



## 저작자표시-비영리-변경금지 2.0 대한민국

이용자는 아래의 조건을 따르는 경우에 한하여 자유롭게

- 이 저작물을 복제, 배포, 전송, 전시, 공연 및 방송할 수 있습니다.

다음과 같은 조건을 따라야 합니다:



저작자표시. 귀하는 원저작자를 표시하여야 합니다.



비영리. 귀하는 이 저작물을 영리 목적으로 이용할 수 없습니다.



변경금지. 귀하는 이 저작물을 개작, 변형 또는 가공할 수 없습니다.

- 귀하는, 이 저작물의 재이용이나 배포의 경우, 이 저작물에 적용된 이용허락조건을 명확하게 나타내어야 합니다.
- 저작권자로부터 별도의 허가를 받으면 이러한 조건들은 적용되지 않습니다.

저작권법에 따른 이용자의 권리는 위의 내용에 의하여 영향을 받지 않습니다.

이것은 [이용허락규약\(Legal Code\)](#)을 이해하기 쉽게 요약한 것입니다.

[Disclaimer](#)

공학박사 학위논문

고출력 고에너지 밀도 이차전지용  
유기물 전하 이동 착물에 관한 연구

**Organic charge-transfer complexes for high power-  
and energy-density rechargeable batteries**

2021 년 2 월

서울대학교 대학원

재료공학부

이 세 찬

고출력 고에너지 밀도 이차전지용  
유기물 전하 이동 착물에 관한 연구

Organic charge-transfer complexes for high power-  
and energy-density rechargeable batteries

지도교수 강 기 석

이 논문을 공학박사 학위논문으로 제출함

2021 년 2 월

서울대학교 대학원

재료공학부

이 세 찬

이세찬의 박사 학위논문을 인준함

2020년 12월

위 원 장	박 수 영	(인)
부위원장	강 기 석	(인)
위 원	이 동 환	(인)
위 원	김 천 중	(인)
위 원	Philippe Poizot	(인)



## **Abstract**

# **Organic charge-transfer complexes for high power- and energy-density rechargeable batteries**

**Sechan Lee**

Department of Materials Science and Engineering

College of Engineering

The Graduate School

Seoul National University

High demand on lithium-ion batteries (LIBs) have been continuously increased according to the development of the diverse electronic devices from portable applications to the large-scale electric vehicles. However, currently used LIBs have limitations on utilizing transition metal-based electrode materials induced by limited amount of the resources, narrow boundaries of material candidates, and the low sustainability. As an alternative to be utilized for the future generation energy storage system, organic rechargeable batteries, which use organic redox-active molecules as electrodes, have been highly focused. Organic redox-active compounds are usually constructed based on carbon-network, constituting with the earth-

abundant typical elements. In addition, they have the strong point that chemical tuning can be demonstrated in an easy way. These advantages have a great potential to the structural diversity and sustainability. However, intrinsic material properties of organics, such as low electrical conductivity and high solubility to solvent, limit the electrochemical performances of organic redox-active compounds. Numerous strategies have been tried to overcome those issues, based on their chemical tunability. Molecular-level tunings of adding functional groups and polymerization and electrode-level tunings of hybridizing active material with conductive scaffolds have been applied. However, all the modifications include the addition of the redox inactive part such as applying connecting units and conductive scaffolds, finally decreasing the energy density. Therefore, it is necessary to find the new approach without utilizing the intramolecular force of the redox-inactive part, which originates the trade-off relationship of the electrochemical performances.

In this respect, switching the way of thinking to utilizing the intermolecular forces of redox-active molecules for enhancing the intrinsic material properties is performed. Organic charge-transfer complex (OCTC) is an association of two or more types of organic molecules (donor and acceptor molecules) in which a fraction of electronic charge is transferred between the molecular entities. Distinctive feature of the OCTCs is the charge-transfer interaction, which is induced by the orbital mixing of the highest occupied molecular orbital (HOMO) of donor and the lowest unoccupied molecular orbital (LUMO) of acceptor, and the structural rearrangement of donor and acceptor molecules occurs to form this interaction spontaneously.

Donor and acceptor molecules are rearranged in the same molecular layers through complementary hydrogen bonds, and in the stacked structure, constituting molecules face other molecules in the neighboring layers through  $\pi$ - $\pi$  interaction to have the layered structure. The structural characteristics of OCTCs, which are induced by constructing charge-transfer interaction between donor and acceptor molecules, enable to enhance the structural integrity and electrical conductivity simultaneously. Constituting the OCTC only with redox-active molecules have a high possibility to solve the existing drawbacks of organics, preserving the electrochemical performances.

Here, I applied the OCTC with combining known redox-active molecules, phenazine (PNZ) and 7,7,8,8-tetracyanoquinodimethane (TCNQ), as the electrode material for the first time. PNZ-TCNQ OCTC successfully improved the intrinsic material properties of increased electrical conductivity and reduced solubility to solvent, achieving the respectable battery performances. Nevertheless, the relatively low voltage of organics and the redox inactivity of PNZ monomer still limited the energy density. To solve the remaining problem on model PNZ-TCNQ OCTC, exploiting the high voltage organic cathode for substituting low voltage donor molecule and realizing the full redox-activity of model OCTC are further progressed in parallel. First, a new donor molecule (dibenzo-1,4-dioxin (DD)) with the extremely high voltage of 4.1 V vs. Li/Li<sup>+</sup> is designed by substituting the redox center atoms to the Group 16 element of oxygen, which has the high electronegativity. New OCTC electrode with the DD and TCNQ was successfully fabricated, and DD-

TCNQ OCTC exhibited the large energy density of  $\sim 560 \text{ Wh kg}^{-1}$  as well as the comparable electrical conductivity ( $2.785 \times 10^{-7} \text{ S cm}^{-1}$ ) to the inorganic electrodes and improved battery performances. Second, optimization of the electrochemical system is performed to reveal the origin of the redox-inactive property of PNZ donor component in OCTC and realize the full-redox reaction. Unlike the inorganic electrodes, it is currently suggested that the redox mechanism of organic electrode materials is affected by the types of charge carrying ions and solvent molecules. Therefore, various types of representative solvents from non-aqueous to aqueous solvents and charge carrying ions from monovalent to divalent ions are utilized for scrutinizing the redox reaction mechanism of model PNZ–TCNQ OCTC. It is observed that the redox reaction pathways of the model OCTC (PNZ–TCNQ) electrode differs according to the types of solvent and charge carrying ions. Interesting point is that the PNZ–TCNQ OCTC electrode in Zn-aqueous electrolyte only could fully utilize the redox activity of both PNZ and TCNQ molecules, while it only shows the singular redox reaction of TCNQ in other Li-based electrolytes. Therefore, the distinct redox mechanisms according to the electrolyte types are systematically analyzed, and it is observed that immediate phase transformation of the active material occurred just after electrolyte exposure without the case in the Zn-aqueous electrolyte. The preformed product from the initial phase transformation is confirmed as the side-product from the chemical interaction between the TCNQ molecule and electrolytes. It is speculated that structural stability plays a critical role to realize the full redox reaction of PNZ–TCNQ OCTC in Zn-aqueous electrolyte,



while other electrolytes induce the unwanted side reaction inducing the structural degradation and redox-instability of OCTC. On the other hand, synergetic effect of conductive aqueous medium and structural stability in Zn-aqueous electrolyte achieves the further improved rate and cycle performances. This novel material group, OCTC, which can enhance the intrinsic material properties without any additives, opens up a new avenue of enlarging the material candidates for the future energy storage system. The unlimited potential of numerous combinations of organic redox-active molecules with the superior battery performances will get close to the commercialization of the sustainable energy materials.

**Keywords:** Rechargeable batteries, Organic redox-active molecules, Organic rechargeable batteries, Charge-transfer complex, Interplay between electrolytes and organic redox-active compounds.

**Student Number:** 2015-20852



# Contents

---

<b>List of Figures .....</b>	<b>xi</b>
<b>Chapter 1. Introduction .....</b>	<b>1</b>
1.1 Motivation and objectives .....	1
1.2 The concept of organic charge-transfer complexes and outlines .....	4
1.3 References .....	9
<b>Chapter 2. Construction of organic charge-transfer complex with organic redox-active molecules .....</b>	<b>12</b>
2.1 Research background.....	12
2.2 Experimental methods .....	20
2.2.1 Preparation of materials .....	20
2.2.2 Material characterization .....	20
2.2.3 Electrochemical measurements .....	21
2.2.4 <i>Ex situ</i> electrode characterization.....	22
2.2.5 Size reduction of particles of PNZ–TCNQ and synthesis of CNT aligned electrodes.....	22
2.3 Results and discussions .....	24
2.3.1 Material characterization and material properties of PNZ–TCNQ .....	24
2.3.2 Electrochemical performances of PNZ–TCNQ .....	34
2.3.3 Strategy for enhancing the cycle stability of PNZ–TCNQ.....	42
2.4 Concluding remarks.....	47
2.5 References .....	49

**Chapter 3. Exploiting the high voltage redox active molecules for the high energy density organic charge-transfer complex electrode. ....54**

3.1 Research background.....	54
3.2 Experimental methods .....	58
3.2.1 Preparation of materials .....	58
3.2.2 Electrochemical measurements .....	58
3.2.3 Material characterization.....	59
3.2.4 <i>Ex situ</i> electrode characterization.....	60
3.3 Results and discussions .....	61
3.3.1 Design concept and energy storage behavior of DD .....	61
3.3.2 Fabrication of DD–TCNQ electrode and its material and electrochemical properties.....	76
3.3.3 Redox mechanism of DD–TCNQ .....	92
3.4 Concluding remarks.....	100
3.5 References .....	102

**Chapter 4. Elucidating the energy storage mechanism of charge-transfer complex according to the interplay with electrolytes.....105**

4.1 Research background.....	105
4.2 Experimental methods .....	109
4.2.1 Preparation of materials .....	109
4.2.2 Electrochemical measurements .....	109
4.2.3 <i>Ex situ</i> electrode characterization.....	110
4.3 Results and discussions .....	111
4.3.1 Diverse redox reaction pathways according to the electrolyte types .....	111

4.3.2 Structural investigation on the intermediate phases of PNZ–TCNQ OCTC electrode during battery cycling .....	122
4.3.3 Thermal and chemical investigation on the pre-formed product during battery cycling .....	126
4.3.4 The model for interplay between PNZ–TCNQ OCTC and electrolytes .....	136
4.3.5 Electrochemical performances of PNZ–TCNQ OCTC in Zn aqueous battery .....	141
4.3.6 Quantitative and qualitative analysis on dissolution behavior of organic redox-active compounds .....	152
4.4 Concluding remarks.....	160
4.5 References .....	163
<b>Chapter 5. Conclusion.....</b>	<b>168</b>
<b>Chapter 6. Abstract in Korean .....</b>	<b>172</b>

## List of Figures

- Figure 2.1** Conceptual diagram and brief structural description of the PNZ–TCNQ OCTC.
- Figure 2.2** Schematic diagram of working principles of the OCTC.
- Figure 2.3** Electrical conductivities of representative inorganic and organic redox active species and the PNZ–TCNQ OCTC.
- Figure 2.4** **Detailed structural description of PNZ–TCNQ OCTC in the microscopic- and macroscopic-levels.** (a) Detailed structural information for PNZ–TCNQ. (dotted line: hydrogen bonds between molecules,  $\pi$ – $\pi$  interactions occur between the slabs). (b) SEM image of pristine PNZ–TCNQ powder.
- Figure 2.5** XRD patterns of PNZ–TCNQ, monomer units, and simulated PNZ–TCNQ.
- Figure 2.6** Color characterization of PNZ–TCNQ and its constituting monomers. (a) Observed color change and (b) UV-vis spectra of powder dispersion (PNZ, TCNQ, and PNZ–TCNQ) in solutions (THF/H<sub>2</sub>O: v/v=5:95).

- Figure 2.7** Chemical investigation of PNZ–TCNQ and its constituting monomers. (a) FTIR and (b) Raman spectra of powders (PNZ, TCNQ, and PNZ–TCNQ)
- Figure 2.8** Material properties of PNZ, TCNQ, and PNZ–TCNQ. Solubility with electrolytes measured using UV–vis spectroscopy after 6-h storage at high temperature (60 °C). The electrical conductivities were determined using four-probe measurements.
- Figure 2.9** **Quantitative analysis of dissolution problem for organic electrode materials.** UV–vis spectra of (a) PNZ, (b) TCNQ, and (c) PNZ–TCNQ OCTC after 6-h storage at 60 °C. Related to Figure 2.8.
- Figure 2.10** Capacity–voltage profiles of monomolecules (PNZ, TCNQ) and charge-transfer complex (PNZ–TCNQ) during the second cycle.
- Figure 2.11** Capacity–voltage profile of PNZ–TCNQ for 1, 2 and 5 cycles. Related to Figure 2.10.
- Figure 2.12** **Capacity–voltage profile for full activation of PNZ–TCNQ.** Voltage–capacity curve of PNZ–TCNQ with the lower voltage limit of 1.0 V vs. Li/Li<sup>+</sup> for 2–5 cycles.
- Figure 2.13** Rate capability of PNZ–TCNQ at 50, 150, 300, and 500 mA g<sup>−1</sup>.

- Figure 2.14** Capacity–voltage profiles with high contents of active materials: 40 wt%, 90 wt%, and 95 wt% in total electrode.
- Figure 2.15** **Comparison of cyclability of charge–transfer complex and its monomer units.** Capacity retention curves of PNZ, TCNQ, and PNZ–TCNQ. Related to Figure 2.18.
- Figure 2.16** ***Ex situ* UV–vis analysis of OCTC electrodes during first cycle.** *Ex situ* UV–vis spectra of OCTC electrodes for PNZ–TCNQ at the different state-of-charge.
- Figure 2.17** **Chemical reversibility of OCTC.** FTIR spectra of further cycled OCTC electrodes for PNZ–TCNQ.
- Figure 2.18** Capacity retention curves of bare TCNQ, bare PNZ–TCNQ, and size-reduced PNZ–TCNQ aligned on CNTs.
- 

- Figure 3.1** Schematic diagram of the molecular design of DD.
- Figure 3.2** Frontier molecular orbital (FMO) energies of DD, DD<sup>+</sup>, EC, and DMC. Note that the energy levels of DD change upon oxidation due to the relaxation effect of the molecules.
- Figure 3.3** Cell configuration of DD rechargeable battery.



- Figure 3.4** Capacity–voltage profile of DD.
- Figure 3.5** (a) Capacity–voltage curve of DD for 1, 2, and 5 cycles. (b) Differential capacity ( $dQ/dV$ ) curve of DD.
- Figure 3.6** Voltage comparison of representative cathode materials.
- Figure 3.7** Rate capability of DD at current density of 150, 300, 500, 1000, and 1500 mA g<sup>-1</sup>.
- Figure 3.8** **Investigation of the redox mechanism of DD.** *Ex situ* Fourier-transform infrared (FTIR) spectra of DD.
- Figure 3.9** **Investigation of the redox mechanism of DD.** *Ex situ* X-ray photoelectron spectroscopy (XPS) spectra of DD.
- Figure 3.10** Natural population analysis (NPA) of DD and DD<sup>+</sup>. The depth of the blue color denotes the extent of change in charge accompanying one-electron oxidation.
- Figure 3.11** Charge distribution calculations of DD and DD<sup>+</sup> using NPA.
- Figure 3.12** **Detailed structural description of PNZ–TCNQ OCTC in the microscopic- and macroscopic-levels.** (a) Chemical formula of DD and TCNQ and detailed structural information for DD–TCNQ: in-plane and side view ( $\pi$ – $\pi$  interactions occur between the slabs). (b) SEM image of pristine DD–TCNQ powder.

- Figure 3.13** XRD patterns of DD–TCNQ and its monomers and simulated pattern of DD–TCNQ.
- Figure 3.14** Color characterization of DD–TCNQ and its constituting monomers. (a) Observed color change and (b) UV-vis spectra of powder dispersion (DD, TCNQ, and DD–TCNQ) in solutions (THF/H<sub>2</sub>O: v/v=5:95).
- Figure 3.15** Chemical investigation of DD–TCNQ and its constituting monomers. (a) FTIR and (b) Raman spectra of powders (DD, TCNQ, and DD–TCNQ)
- Figure 3.16** UV-vis spectra of DD–TCNQ and their constituting monomers.
- Figure 3.17** Material properties of DD, TCNQ, and DD–TCNQ. Solubility with electrolytes measured using UV-vis spectroscopy after 6-h storage at high temperature (60 °C). The electrical conductivities were determined using four-probe measurements.
- Figure 3.18** Capacity–voltage profiles of monomolecules (DD, TCNQ) and charge–transfer complex (DD–TCNQ) during the second cycle.
- Figure 3.19** Capacity–voltage profile of DD–TCNQ during the 1, 2 and 5 cycles.
- Figure 3.20** Rate capability of DD–TCNQ at 50, 150, 300, 500, and 1000 mA g<sup>-1</sup>.

- Figure 3.21** Capacity retention curve of DD–TCNQ.
- Figure 3.22** *Ex situ* UV–vis analysis of OCTC electrodes during first cycle. *Ex situ* UV–Vis spectra of OCTC electrodes for DD–TCNQ at the different state-of-charge.
- Figure 3.23** **Chemical reversibility of OCTCs.** FTIR spectra of further cycled OCTC electrodes for DD–TCNQ.
- Figure 3.24** Capacity–voltage profile of DD–TCNQ. Numbers (1-7) denote the electrode samples at each state-of-charge related to Figure 3.25, 3.26, 3.27, and 3.28.
- Figure 3.25** *Ex situ* FTIR data in the regions of (a) 2250–2150  $\text{cm}^{-1}$  and (b) 1600–1200  $\text{cm}^{-1}$ . The numbered labels are the same as those in Figure 3.24.
- Figure 3.26** *Ex situ* XPS data in the regions of (a) 406–392 eV and (b) 288–282 eV. The numbered labels are the same as those in Figure 3.24.
- Figure 3.27** *Ex situ* XPS data for DD–TCNQ. O 1s spectra of DD–TCNQ during the first cycle. The numbered labels are the same as those in Figure 3.24.
- Figure 3.28** Suggested redox mechanism of DD–TCNQ. The numbered labels are the same as those in Figure 3.24.

- 
- Figure 4.1** Capacity–voltage profiles of PNZ–TCNQ in universal electrolytes during the discharging process.
- Figure 4.2** Capacity–voltage profiles of PNZ–TCNQ OCTC electrode in the reported electrolyte (1M LiTFSI in TEGDME) and the mostly used electrolyte (1M LiTFSI in EC/DMC).
- Figure 4.3** **Electrochemical tests of PNZ–TCNQ OCTC electrode in the diverse types of solvents for Li non-aqueous batteries.** Capacity–voltage profiles of PNZ–TCNQ OCTC electrodes in 1M LiTFSI in (a) TEGDME, DEGDME, and DME, (b) EC/DMC, EC/PC, and PC, and (c) DMSO, DOL/DME, and ACN.
- Figure 4.4** Capacity–voltage profiles of PNZ–TCNQ OCTC electrode in Li-aqueous electrolyte.
- Figure 4.5** **Electrochemical tests of PNZ–TCNQ OCTC electrode in Zn ion batteries.** Capacity–voltage profiles of PNZ–TCNQ OCTC electrode in 1M Zn(TFSI)<sub>2</sub> in (a) PC, (b) TEGDME, (c) DMSO, and (d) H<sub>2</sub>O.

**Figure 4.6**      **Electrochemical behaviors of PNZ–TCNQ according to the electrolyte types and the four representative reaction types of PNZ–TCNQ.** (a) Capacity–voltage profiles and (b) differential capacity curves of PNZ–TCNQ in Li ion with carbonates electrolytes, ether electrolytes, aqueous electrolytes, and Zn ion with aqueous electrolytes. (c) Suggested redox mechanism of PNZ–TCNQ regarding the four-electron storage.

**Figure 4.7**      **Structural investigation on the intermediate phase of PNZ–TCNQ during cycling.** *Ex situ* XRD of PNZ–TCNQ during discharging and charging processes in (a) 1M LiTFSI in EC/DMC (v/v 1:1), (b) 1M LiTFSI in TEGDME, (c) 1M LiTFSI in H<sub>2</sub>O, and (d) 1M Zn(TFSI)<sub>2</sub> in H<sub>2</sub>O.

**Figure 4.8**      **Immediate phase transformation of PNZ–TCNQ OCTC electrode.** (a) Long-range arrangements of PNZ–TCNQ powder, pristine, and electrodes after electrolytes exposure. (b) Comparison of the residual amount of PNZ–TCNQ of pristine and electrodes in 1M LiTFSI in EC/DMC, LiTFSI in TEGDME, and Zn(TFSI)<sub>2</sub> in H<sub>2</sub>O. (c) Structural destruction of PNZ–TCNQ electrode after the exposure to 1M LiTFSI in H<sub>2</sub>O.

**Figure 4.9**      Thermo-gravimetric (TG) curves (left) and correlated TG derivative curves (right) of PNZ–TCNQ powder, pristine, and

electrodes obtained from the cell disassembly without battery cycling.

- Figure 4.10** Residual weight of the electrode after elevating the temperature to 600 °C.
- Figure 4.11** **Thermal investigation on the pre-formed product according to the various types of electrolytes and solvents.** TG curves of PNZ–TCNQ powder immersed in the electrolytes and pure solvents for 1 day, showing (a) same trend with the original PNZ–TCNQ and (b) altered trend from the original PNZ–TCNQ, respectively.
- Figure 4.12** **Thermal investigation on the pre-formed product according to the various types of electrolytes and solvents.** TG curves of TCNQ powder immersed in the electrolytes and pure solvents for 1 day, showing (a) same trend with the original TCNQ and (b) altered trend from the original TCNQ, respectively.
- Figure 4.13** Fourier-transform infrared spectroscopy (FTIR) curves of PNZ–TCNQ powder immersed in the electrolytes for 1 day in the range of (a) 4000–2500 cm<sup>-1</sup> and (b) 2400–2100 cm<sup>-1</sup>.
- Figure 4.14** Schematic diagram of the interplay model between active material and electrolytes.

- Figure 4.15** *Ex situ* TG curves (left) and correlated TG derivative curves (right) of PNZ–TCNQ electrodes in (Top-to-bottom: 1M LiTFSI in EC/DMC, 1M LiTFSI in TEGDME, 1M LiTFSI in H<sub>2</sub>O, and 1M Zn(TFSI)<sub>2</sub> in H<sub>2</sub>O)
- Figure 4.16** *Ex situ* XRD and correlated capacity–voltage profile of PNZ–TCNQ OCTC electrode after further cycling.
- Figure 4.17** Electron transfer per formula unit of PNZ–TCNQ and its constituting monomers in the various current rates.
- Figure 4.18** High active contents test of PNZ–TCNQ electrodes in Zn aqueous batteries.
- Figure 4.19** Specific and areal capacities of PNZ–TCNQ electrodes with the active contents of 60% in the various active material loading density.
- Figure 4.20** Specific and areal capacities of PNZ–TCNQ electrodes with the active contents of 40% in the various active material loading density.
- Figure 4.21** Specific and areal capacities of PNZ–TCNQ electrodes with the active contents of 80% in the various active material loading density.

- Figure 4.22** Areal capacity comparison of PNZ–TCNQ with representatively reported electrodes in Zn aqueous batteries.
- Figure 4.23** Ragone plot of PNZ–TCNQ with representatively reported electrodes in Zn aqueous batteries.
- Figure 4.24** Capacity retention curves of PNZ–TCNQ in Zn aqueous and Li non-aqueous batteries.
- Figure 4.25** **Quantitative analysis on dissolution behavior.** (a) Electrode weight change and (b) the deviation of the electrode weight change between the experimental and theoretical values during battery cycling.
- Figure 4.26** Capacity retention curves of PNZ–TCNQ OCTC electrode and its constituting monomers (PNZ and TCNQ).
- Figure 4.27** **Quantitative analysis on dissolution behavior for the constituting monomers of PNZ and TCNQ.** Electrode weight change during battery cycling for (a) PNZ and (b) TCNQ.
- Figure 4.28** Color change of the water solvents storing the PNZ–TCNQ and its constituting monomers at different state-of-charge.
- Figure 4.29** **Qualitative analysis on dissolution behavior.** *Ex situ* UV–vis spectroscopy of the PNZ–TCNQ and its constituting monomers (PNZ and TCNQ) during battery cycling.





# Chapter 1. Introduction

## 1.1 Motivation and objectives

Development of environmental-friendly and renewable energy resources has been highly demanded due to the energy and environmental issues, arising from the exhaustion of fossil fuels, global warming, and so on. Accordingly, efficient energy storage and conversion are highly required to treat the above-mentioned intermittently supplied renewable energy resources. Li ion batteries (LIBs) has been concerned as the great candidate among the various energy storage systems due to their high energy- and power-density.<sup>[1]</sup>

Currently used LIBs have the transition metal-based electrode materials as a cathode component and the graphite as an anode component. Transition metal-based electrode materials limit the currently used LIBs to be applied to the future generation energy storage system. Transition metals have an issue of the scarcity of the resources from the localization and little reserves of the deposits. Moreover, its heavy molecular weight and limited material candidates impedes the currently used LIBs to be still utilized in the future. Hence, various types of next-generation electrode materials have been developed over the past 20 years to alternate the transition metal-based electrode materials in the LIBs.<sup>[1-3]</sup>

One of the promising candidates of the electrode materials in post LIBs is the organic redox-active molecules.<sup>[4-7]</sup> Organic electrode materials are transition

metal-free, resulting in non-toxicity and the earth-abundance of the constituting elements. The distinctive advantage of the organic redox active molecules is that they are chemically tunable with easy way. They are usually constructed based on carbon network, which can have the large possible chemical diversity to be tuned, and furthermore, they do not require the extreme synthesis condition of high temperature and pressure. In addition to the chemical tunability, organic electrode materials also have the potential advantages of reducing the CO<sub>2</sub> emission during the production and recycling processes.

Exploitation on the organic electrode materials have been actively progressed. However, the electrochemical performances of them could not reach the current level of transition metal-based electrode materials since organic electrode materials have their own limitations from the intrinsic material properties.<sup>[7-8]</sup> Almost of reported organic redox-active compounds have one or more intrinsic impediments of the low electrical conductivity, high solubility to solvent, and the relatively low redox potential compared to the transition metal-based electrode materials. These characteristics of organics influence the limited electrochemical performances of poor rate performances, bad cycle stability, and low energy density, respectively.

Diverse approaches to overcome those drawbacks have been suggested in the molecular- and electrode-level. However, all the suggested strategies have the trade-off relationship among the battery performances. The chemical tunings on the single molecules have been widely applied such as polymerization and adding the

functional groups that induce the decrease of solubility.<sup>[9-12]</sup> Currently, constructing molecular architecture as triangle- or honeycomb-like form, called as a covalent organic framework (COF), are developed to simultaneously solve the dissolution and conductivity issues.<sup>[13-15]</sup> However, all the molecular-level tunings require the addition of redox inactive parts such as connecting unit between each single redox-active moiety and the attached functional groups that are redox-inactive. These increase the total weight of the molecules and further reduce the energy density of the organic electrode materials. On the other hand, electrode-level tunings have also been conducted through hybridization with conductive scaffolds such as graphene and carbon nanotubes.<sup>[16-18]</sup> Hybridized electrodes can induce the increase of electrical conductivity and decrease of the solubility to solvent at the same time, however, attached conductive scaffolds are also redox-inactive, resulting in the decrease of energy density with respect to the electrode-level weight increase. Therefore, it can be noticed that it is required to develop the novel research strategy, which can avoid utilizing the redox-inactive unit to enhance the intrinsic material properties simultaneously with preserving the redox capability.

## 1.2 The concept of organic charge-transfer complexes and outlines

The key clue for the novel approach is only utilizing the redox-active molecules, and it should be noticed that the conventionally suggested ways of chemical tunings are totally depended on the intramolecular interaction such as inductive effect and conjugation. Intramolecular interaction is accompanied by the redox-inactive functional groups or the connecting units, however, intermolecular interaction such as hydrogen bonding and  $\pi$ - $\pi$  interaction can be formed without any additives.

An organic charge-transfer complex (OCTC) is an association of two or more types of organic molecules in which a fraction of electronic charge is transferred between the molecular entities.<sup>[19-20]</sup> An OCTC generally consists of two types of constituents, an electron-donating and electron-accepting molecules. Distinctive feature of the OCTCs is the charge-transfer interaction, which is induced by the orbital mixing of the highest occupied molecular orbital (HOMO) of donor and the lowest unoccupied molecular orbital (LUMO) of acceptor. Charge-transfer interaction is the main driving force to undergo the structural rearrangement of donor and acceptor molecules, resulting in forming a characteristic crystal structure (stacking structure) of OCTCs. Donor and acceptor molecules are rearranged in the same molecular layers through complementary hydrogen bonds, to be easily stacked onto other molecules in the upper and lower molecular layers. In the stacked structure, constituting molecules face other molecules in the neighboring layers

through  $\pi$ - $\pi$  interaction to generally have the layered structure, creating a charge-transfer interaction. The intermolecular forces in OCTCs such as complementary hydrogen bonds and  $\pi$ - $\pi$  interaction, enable to enhance the intrinsic material properties. Constituting molecule couples in OCTCs are typically bound to each other, forming a molecular layer through hydrogen bonds, and the molecules in the layer are surrounded with hydrogen bonds throughout the neighboring molecules, offering the high structural stability. In addition, the common  $\pi$ - $\pi$  interaction between the layers of molecules promotes well-ordered stacking of these molecular layers. The dense electron cloud formed in the slab space by the  $\pi$ - $\pi$  interaction and the segregated electron density creates a charge-transport path between the layers through which electrons can move freely, resulting in the significantly enhanced conductivity compared that of each constituting molecule unit. These enhanced material properties are expected to solve the intrinsic issues of organic electrode materials such as dissolution and relatively low electrical conductivity at the same time, which are directly related to the battery performances of cycle stability and rate performance, respectively. Constituting the OCTC with only two or more types of redox-active molecules can achieve the initial objective without any additives, enhancing the intrinsic material properties with preserving the electrochemical performances.

OCTCs have been applied as semiconductors<sup>[21]</sup> and superconductors<sup>[22]</sup>, however, they have not yet been investigated for used in rechargeable batteries. Herein, I propose the novel material group, OCTCs, as a viable concept that can

mitigate the intrinsic drawbacks of organic electrode materials with preserving the intrinsic redox capability of organic compounds, and I apply the OCTCs as electrode materials in rechargeable batteries for the first time. In addition, designing new donor molecules with high voltage and investigation on the redox mechanism of OCTC are further progressed in parallel, to overcome the redox-inactive behavior of the donor component of the firstly developed model OCTC.

Chapter 2 excavates a model compound of OCTC, which is constructed with the known-redox active molecules.<sup>[23]</sup> Phenazine (PNZ) and 7,7,8,8-tetracyanoquinodimethane (TCNQ) are firstly selected to be electron donor and acceptor molecules, respectively, since they are known to have the planar structure with the reversible two-electron redox reaction. PNZ–TCNQ OCTC showed the enhancement of the intrinsic material properties of electrical conductivity and solubility. PNZ–TCNQ OCTC electrode was applied as a cathode material in LIBs, exhibiting the reversible redox reaction successfully. Furthermore, the high rate performance at the high current rate of 500 mA g<sup>-1</sup> (~3.5 C-rate) and the high active material contents in the electrode were realized, originated from the conductive nature of OCTC compared to the constituting monomers. However, there remains the limitations on battery performance. The energy density of PNZ–TCNQ OCTC is limited due to the low voltage and redox-instability of PNZ monomer. To solve the remaining problem on the model PNZ–TCNQ OCTC, exploiting the high voltage organic cathode for substituting the low voltage donor molecule and realizing full-redox activities of PNZ–TCNQ OCTC are further progressed in parallel.

Chapter 3 suggests the design principle of exploiting the high voltage organic cathode material for proving the full redox-activity of charge-transfer complex concept.<sup>[23-24]</sup> *p*-type organic redox-active species are mainly treated, and the final product with 4 V class, dibenzo-1,4-dioxin (DD), is designed through the redox center atom substitution strategy. Substitution of PNZ, which were redox-inactive in the OCTC, to the newly developed 4 V class cathode material, DD, is successfully demonstrated. DD–TCNQ OCTC exhibits the further increase of electrical conductivity, even comparable to that of currently used inorganic-based electrode materials, and the decrease of solubility to solvent. The electrochemical performance and energy storage mechanism of DD–TCNQ OCTC electrode are further studied, presenting the improved energy density of 560 Wh kg<sup>-1</sup> with the full redox activation of both donor and acceptor molecules.

Chapter 4 reveals the origin of the redox-inactive property of PNZ donor component in OCTC and realizes the full-redox reaction through optimizing the electrochemical system.<sup>[24-26]</sup> PNZ donor molecule in the model OCTC loses its redox capability in the firstly applied model battery system. Unlike the inorganic electrodes, it is currently suggested that the redox mechanism of organic electrode materials is affected by the types of charge carrying ions and solvent molecules. Therefore, the redox behaviors according to the diverse electrolyte types is firstly investigated for scrutinizing the redox reaction mechanism of the model PNZ–TCNQ OCTC. Different redox reaction pathways are observed in the distinct types of solvents and charge carrying ions, and the origin of this phenomenon is revealed



as the occurrence of unexpected pre-formed products just after electrolyte exposure. Through the structural and thermal analysis, it is confirmed that the initially started side-reaction is occurred by the chemical interaction between TCNQ molecule and the electrolytes. Initially altered structure of the PNZ–TCNQ OCTC from the chemical side-reaction induces the different redox reaction pathways with the following evolved distinct intermediate products. The electrolyte-participating chemical change may weaken the intermolecular interaction between the PNZ and TCNQ molecules in OCTC, further resulting in the material degradation. As a result, Zn-aqueous electrolyte, which shows the stable behavior without any side reaction, is the most compatible electrolyte system to the OCTC electrode with maintaining the own crystal structure of OCTC. Therefore, the full redox activation of PNZ–TCNQ OCTC with four-electron redox reaction and the enhanced rate and cycle performances are further performed in Zn aqueous batteries.

### 1.3 References

- [1] J. M. Tarascon, M. Armand, *Nature* **2001**, 414, 359.
- [2] D. Larcher, J. M. Tarascon, *Nature Chemistry* **2015**, 7, 19.
- [3] M. Armand, J. M. Tarascon, *Nature* **2008**, 451, 652.
- [4] Y. Liang, Z. Tao, J. Chen, *Advanced Energy Materials* **2012**, 2, 742.
- [5] S. Lee, G. Kwon, K. Ku, K. Yoon, S.-K. Jung, H.-D. Lim, K. Kang, *Advanced Materials* **2018**, 30, 1704682.
- [6] Z. Song, H. Zhou, *Energy & Environmental Science* **2013**, 6, 2280.
- [7] S. Lee, J. Hong, K. Kang, *Advanced Energy Materials* **2020**, 10, 2001445.
- [8] Y. Lu, J. Chen, *Nature Reviews Chemistry* **2020**, 4, 127.
- [9] Y. Liang, P. Zhang, S. Yang, Z. Tao, J. Chen, *Advanced Energy Materials* **2013**, 3, 600.
- [10] Y. Liang, P. Zhang, J. Chen, *Chemical Science* **2013**, 4, 1330.
- [11] M. Yao, H. Senoh, S.-i. Yamazaki, Z. Siroma, T. Sakai, K. Yasuda, *Journal of Power Sources* **2010**, 195, 8336.
- [12] H.-g. Wang, S. Yuan, D.-l. Ma, X.-l. Huang, F.-l. Meng, X.-b. Zhang, *Advanced Energy Materials* **2014**, 4, 1301651.
- [13] K. Sakaushi, E. Hosono, G. Nickerl, T. Gemming, H. Zhou, S. Kaskel, J. Eckert, *Nature Communications* **2013**, 4, 1485.
- [14] D.-H. Yang, Z.-Q. Yao, D. Wu, Y.-H. Zhang, Z. Zhou, X.-H. Bu, *Journal of Materials Chemistry A* **2016**, 4, 18621.

- [15] S. Wang, Q. Wang, P. Shao, Y. Han, X. Gao, L. Ma, S. Yuan, X. Ma, J. Zhou, X. Feng, B. Wang, *Journal of the American Chemical Society* **2017**, 139, 4258.
- [16] M. Lee, J. Hong, H. Kim, H.-D. Lim, S. B. Cho, K. Kang, C. B. Park, *Advanced Materials* **2014**, 26, 2608.
- [17] H. Wang, P. Hu, J. Yang, G. Gong, L. Guo, X. Chen, *Advanced Materials* **2015**, 27, 2348.
- [18] M.-S. Kwon, A. Choi, Y. Park, J. Y. Cheon, H. Kang, Y. N. Jo, Y.-J. Kim, S. Y. Hong, S. H. Joo, C. Yang, K. T. Lee, *Scientific Reports* **2014**, 4, 7404.
- [19] K. P. Goetz, D. Vermeulen, M. E. Payne, C. Kloc, L. E. McNeil, O. D. Jurchescu, *Journal of Materials Chemistry C* **2014**, 2, 3065.
- [20] J. B. Torrance, *Molecular Crystals and Liquid Crystals* **1985**, 126, 55.
- [21] S. Horiuchi, T. Hasegawa, Y. Tokura, *Journal of the Physical Society of Japan* **2006**, 75, 051016.
- [22] G. Saito, Y. Yoshida, in *Unimolecular and supramolecular electronics I*, Springer **2011**, p. 67.
- [23] S. Lee, J. Hong, S.-K. Jung, K. Ku, G. Kwon, W. M. Seong, H. Kim, G. Yoon, I. Kang, K. Hong, H. W. Jang, K. Kang, *Energy Storage Materials* **2019**, 20, 462.
- [24] S. Lee, K. Lee, K. Ku, J. Hong, S. Y. Park, J. E. Kwon, K. Kang, *Advanced Energy Materials* **2020**, 10, 2001635.

- [25] S. Lee, I. Kang, J. Kim, S. h. Kim, K. Kang, J. Hong, *Journal of Power Sources* **2020**, 472, 228334.
- [26] S. Lee, J. E. Kwon, J. Hong, S. Y. Park, K. Kang, *Journal of Materials Chemistry A* **2019**, 7, 11438.

## **Chapter 2. Construction of organic charge-transfer complex with organic redox-active molecules**

(The essence of this chapter has been published in *Energy Storage Materials*.

Reprinted with permission from [S. Lee *et al.*, *Energy Storage Mater.* **20**, 462 (2019)]

Copyright (2020) Elsevier)

### **2.1 Research background**

The development of sustainable and economical energy storage technologies is indispensable to address the increasing demand for renewable energy sources and promotion of the widespread adoption of electric vehicles. LIBs are one of the most widely adopted technologies among available energy storage options because of their high energy and power density with reliable stability.<sup>[1]</sup> Significant increases in the mass production of LIBs are thus expected in the near future to meet the surging needs for electric vehicles and large-scale energy storage systems. We speculate that if electric vehicles were to grow to make up 10% of the global car market, this change alone would necessitate at least a fourfold increase in the total LIB production worldwide.<sup>[2]</sup> Nevertheless, the large production of LIBs presents a serious issue in terms of the availability of resources, particularly of the transition metals (*i.e.*, Co or Ni) on which the current LIB chemistry heavily relies. The limited amount of transition metal resources and their concentration in certain countries may potentially result in high and/or unstable LIB production costs.<sup>[1, 3]</sup> In addition, the use of large amounts of transition metals is neither sustainable nor environmentally

benign, as their production and/or recycling generate substantial carbon dioxide emissions.<sup>[1, 4]</sup>

Organic redox compounds have been proposed as promising alternatives to transition-metal-oxide electrode materials in LIBs because of their low cost and earth abundance as well as the minimal carbon dioxide footprint associated with their synthesis and recycling processes.<sup>[5-7]</sup> Moreover, whereas the theoretical limit of the charge capacity for conventional electrodes based on transition metal oxides has almost been reached, leaving little room for further improvement, the chemical diversity of organic redox compounds and their light weight offer great promise for further development of high-capacity organic electrodes. For example, some organic compounds such as benzoquinone, rhodizionate, and muconate have been demonstrated to be capable of delivering a specific capacity of 500–600 mAh g<sup>-1</sup> near 3 V (vs. Li/Li<sup>+</sup>), which is hardly achievable using conventional transition metal oxide-based chemistries.<sup>[7-9]</sup> Nevertheless, key bottlenecks to further progress include their intrinsically low electrical conductivity and high solubility in organic solvents.<sup>[6, 10-11]</sup> The early developed redox-active organic species were highly dissolvable in the electrolyte, inducing severe cycle degradation and thus offsetting the merits of the initial high charge capacity.<sup>[12-13]</sup> Moreover, the insulating nature of most organic compounds necessitates the use of a large amount of conductive agents in the electrode preparation, which substantially reduces the practical energy density.

Approaches to resolve these issues have generally included polymerization of the redox-active organic monomers or the fabrication of composites using conductive scaffolds. Polymerization can partly mitigate the dissolution issues by anchoring the redox-active parts to an insoluble polymer backbone, resulting in improvement of the capacity retention.<sup>[14-16]</sup> However, this improvement is often accompanied by a poorer electrical conductivity and an increase in weight after the polymerization because of the addition of the redox-inactive backbone units, leading to deterioration of both the power capability and gravimetric energy density. The synthesis of composites or hybrids of organic electrode materials using conductive scaffolds based on carbonaceous materials has also often been applied.<sup>[17-18]</sup> The conductive scaffolds enhance the electrical conduction in the electrode and provide anchoring sites for the redox organic compounds, thus improving the power and capacity retention. However, the substantial amount of additional matrices or scaffolds significantly increases the electrode weight, thus reducing the specific energy density. Moreover, the anchoring of the organic compounds is only partially effective for long-term cycling.

Herein, we propose the formation of organic charge-transfer complexes (OCTCs) as a viable self-anchoring approach that can mitigate these issues of reduced electrical conductivity and dissolution, thereby preserving the intrinsic redox capability of organic compounds. (Figures 2.1 and 2.2) An OCTC is an association of two or more types of organic molecules in which a fraction of electronic charge is transferred between the molecular entities.<sup>[19-20]</sup> An OCTC

generally consists of two types of constituents, an electron-donating and electron-accepting molecule, and any molecule couples with different electron-accepting capabilities are potential OCTC candidates. Distinctive feature of the OCTCs is the charge-transfer interaction, which is induced by the orbital mixing of the highest occupied molecular orbital (HOMO) of donor and the lowest unoccupied molecular orbital (LUMO) of acceptor. Characteristic layered structure of OCTCs is formed through the structural rearrangement of donor and acceptor molecules to have the charge-transfer interaction. Donor and acceptor molecules are rearranged in the same molecular layers through complementary hydrogen bonds, to be easily stacked onto other molecules in the upper and lower molecular layers. In the stacked structure, constituting molecules face other molecules in the neighboring layers through  $\pi$ - $\pi$  interaction, to be located closely for  $\pi$  orbitals mixing, creating a charge-transfer interaction. The intermolecular forces in OCTCs such as complementary hydrogen bonds and  $\pi$ - $\pi$  interaction, enable to enhance the intrinsic material properties. Constituting molecule couples in OCTCs are typically bound to each other, forming a molecular layer through strong hydrogen bonds and offering high structural stability. In addition, the common  $\pi$ - $\pi$  interaction between the layers of molecules promotes well-ordered stacking of these molecular layers. (Figure 2.1) The dense electron cloud formed in the slab space by the  $\pi$ - $\pi$  interaction and the separated electron density creates a charge-transport path between the layers through which electrons can move freely, resulting in significantly enhanced electrical conductivity compared with that of each constituting molecule unit.<sup>[19-25]</sup>(Figure 2.2) Figure 2.3



comparatively illustrates the electrical conductivity of the newly designed OCTC reported hereafter (phenazine-7,7,8,8-tetracyanoquinodimethane (PNZ-TCNQ)), with those of the precursor organic materials (phenazine (PNZ) and 7,7,8,8-tetracyanoquinodimethane (TCNQ)), demonstrating the orders-of-magnitude enhancement. Notably, the electrical conductivity of the OCTC is even comparable to those of commercialized cathode materials such as  $\text{LiMn}_2\text{O}_4$ , NCM111 ( $\text{LiNi}_{1/3}\text{Co}_{1/3}\text{Mn}_{1/3}\text{O}_2$ ), and  $\text{LiFePO}_4$ .<sup>[19, 30-34]</sup> Because of the unique material properties distinct from other organic compounds, OCTCs have been applied as semiconductors<sup>[35]</sup> and superconductors<sup>[36]</sup>; however, they have not yet been investigated for use in rechargeable batteries. While some metal-organic compounds such as Cu-TCNQ have been explored to enhance the intrinsic property of organic electrodes (*e.g.* TCNQ) in batteries, synergetic effects of both organic constituents in the OCTC remain elusive.<sup>[37-38]</sup> In the following, we provide the newly developed OCTC that can serve as promising positive electrodes for lithium rechargeable batteries. A new OCTC is constructed from two well-known redox active species with different electron affinities, and its feasibility as a positive electrode material in a lithium cell is examined.

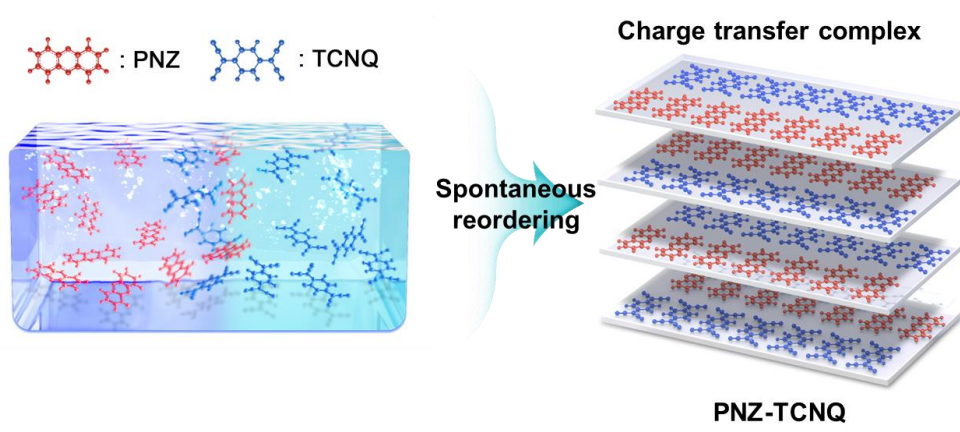


**Figure 2.1** Conceptual diagram and brief structural description of the PNZ–TCNQ OCTC.

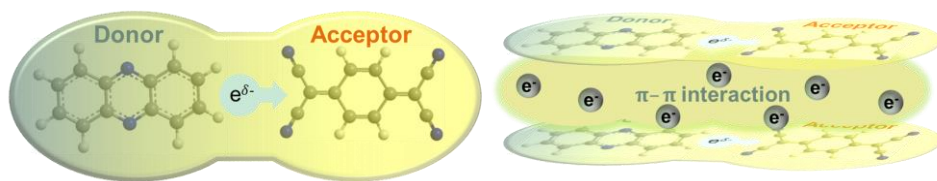


**Figure 2.2** Schematic diagram of working principles of the OCTC.

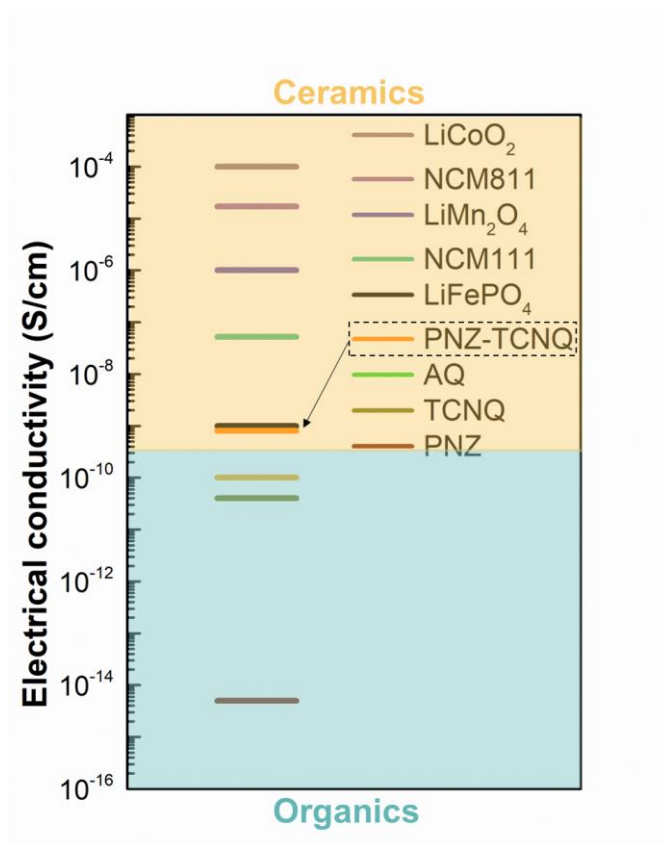


**Figure 2.3** Electrical conductivities of representative inorganic and organic redox active species and the PNZ–TCNQ OCTC.

## **2.2 Experimental methods**

### **2.2.1 Preparation of materials**

PNZ was purchased from Alfa Aesar (USA), and TCNQ was purchased from Sigma-Aldrich (UK). All the commercially available chemicals were utilized without further purification. The charge-transfer complex, PNZ–TCNQ, was synthesized following a procedure previously described in the literature.<sup>[39]</sup> The PNZ and TCNQ powders were mixed in an equimolar ratio in acetone solvent for 3 h at room temperature. The resulting solution was filtered, and the residue was dried at 30 °C overnight.

### **2.2.2 Material characterization**

XRD profiles of the powder samples of PNZ–TCNQ and its monomers were characterized using a D2 PHASER (Bruker, Bremen, Germany) equipped with Cu-K $\alpha$  radiation ( $\lambda$ = 1.54178 Å) at a scanning speed of 0.2° min<sup>-1</sup> in the 2 $\theta$  range of 5°–60°. The electrolytes with the stored electrode samples and the powder dispersed solutions (DD, TCNQ, and DD–TCNQ in THF/H<sub>2</sub>O: v/v=5:95) with the dispersed powders were characterized using a UV–vis spectrometer (Agilent Technologies, Cary 5000) with an optical glass cuvette (Quartz; Hellma®). FTIR spectra were measured using pellets made of the powders (PNZ, TCNQ, and PNZ–TCNQ) and KBr powder on an FT/IR-4200 (Jasco, Japan) at a resolution of 4 cm<sup>-1</sup>. Raman spectra were measured using powders of PNZ–TCNQ and its monomers on

an LabRAM HR Evolution (Horiba, Japan). The fabricated electrodes of the PNZ–TCNQ series (PNZ–TCNQ and its monomer units) were stored in the electrolyte (1 M LiTFSI in TEGDME) for 6 h at 60 °C. A lab-made four-probe station with an Agilent 4156C semiconductor parameter analyzer was used to measure the electrical conductivities of the charge-transfer complex and their constituting monomers. To evaluate the electrical conductivities, pelletized powders were prepared with thicknesses of ~3 mm.

### **2.2.3 Electrochemical measurements**

Capacity–voltage profiles of the charge-transfer complex and their constituting molecules versus a Li metal foil (Hohsen, Japan) in coin-type cells (CR2032) were obtained. The Li metal anode was prepared in an Ar-filled glove box. The cathodes were fabricated by mixing 40% w/w active materials, 40% w/w carbon black (Super P), and 20% w/w polytetrafluoroethylene (PTFE, Aldrich) binder, and all of the sampled-electrodes are 4–6 mg. Especially for the high-content test, cathodes with two additional compositions were formulated by mixing 90% w/w active materials, 5% w/w carbon black, and 5% w/w PTFE binder and 95% w/w active materials, 2.5% w/w carbon black, and 2.5% w/w PTFE binder. A porous glass microfiber membrane (GF/F; Whatman, UK) was used as a separator in the Li cells. The electrolyte was 1 M LiTFSI in TEGDME for PNZ–TCNQ, and the cells were assembled in an inert atmosphere within an Ar-filled glove box. The electrochemical measurements were performed at a constant current density of 50

mA g<sup>-1</sup> in the voltage range of 2.4–3.8 V vs. Li/Li<sup>+</sup>, using a battery test system (Won-A Tech, Korea).

#### **2.2.4 *Ex situ* electrode characterization**

The electrodes of PNZ–TCNQ and TCNQ at different states of cycling were prepared by disassembling coin cells (pristine, 2 cycles, 10 cycles, and 50 cycles) followed by rinsing the electrodes with TEGDME. XRD profiles were obtained using the D2 PHASER with Cu-K $\alpha$  radiation ( $\lambda = 1.54178$  Å) at a scanning speed of 0.2° min<sup>-1</sup> in the 2 $\theta$  range of 5°–60°. The surface morphologies of the electrodes were examined using SEM (MERLIN Compact, ZEISS, Germany). XPS measurements were performed using an Axis Supra<sup>TM</sup> from Kratos (U.K.). All the measured spectra were set to the reference of C 1s (284.4 eV), which is correlated to the Super P. FTIR spectra were measured using pellets made of the electrodes at different states and KBr powder on an FT/IR-4200 (Jasco, Japan) at a resolution of 4 cm<sup>-1</sup>. UV-vis spectra measurements were performed using an JASCO-3000 (Jasco, Japan) at a resolution of 10 nm.

#### **2.2.5 Size reduction of particles of PNZ–TCNQ and synthesis of CNT aligned electrodes**

Size reduction of the PNZ–TCNQ particles was performed using an anti-solvent reduction method. The PNZ–TCNQ powder was dissolved in distilled water to obtain a saturated solution. Then, the same amount of anti-solvent (acetone) was

added to the saturated solution followed by 10 min of sonication. The resulting solution was filtered, and the residue was dried overnight at 30 °C in a vacuum oven. CNT aligned electrodes were synthesized, followed by mixing the CNTs (5 mg) and PNZ–TCNQ (5 mg) in the acetone solvent (20 mL). The solution was homogenized using an ultrasonic Vibra Cell VCX 750 homogenizer (Sonics & Materials Inc., USA) for 10 min (2-s on, 1-s off). The resulting solution was also filtered, and the residue was dried overnight at 30 °C in a vacuum oven.



## 2.3 Results and discussions

### 2.3.1 Material characterization and material properties of PNZ–TCNQ

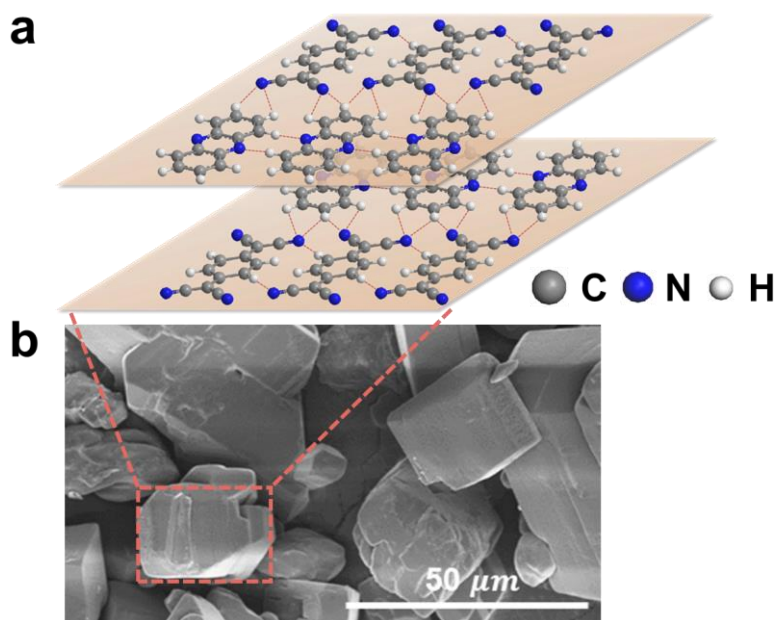
PNZ<sup>[40]</sup> and TCNQ<sup>[41]</sup> are some of the most widely studied redox active organic compounds and were selected as the first model constituents for the formation of the new OCTC electrode.<sup>[22, 39]</sup> (Figure 2.4a) PNZ and TCNQ have been previously reported as potential electrode materials for LIBs, which can deliver redox activity at 1.5/1.2 V and 3.2/2.6 V (vs. Li/Li<sup>+</sup>), respectively. Nevertheless, their low electrical conductivities and their dissolution in the electrolyte lead to low power capability and poor cycle stability.<sup>[40-41]</sup> Although the redox potential of PNZ is relatively low and inadequate for its use as the positive electrode, the planar structures of PNZ were expected to aid in inducing a well-defined layered crystalline structure with TCNQ in the formation of the OCTC.<sup>[19]</sup> As such, the OCTC based on PNZ–TCNQ was prepared from a simple mixing process at room temperature. The PNZ and TCNQ powders were mixed/stirred in acetone solvent in an equimolar ratio at room temperature for 3 hours followed by vacuum filtration and drying at 30 °C overnight. Characterization of the resultant powder indicated that the PNZ–TCNQ OCTC was successfully obtained via this single-step reaction. Well-defined cubic particles are clearly observable in the scanning electron microscopy (SEM) images in Figure 2.4b, suggesting the formation of a new crystalline phase after the mixing and drying processes. The X-ray diffraction (XRD) patterns in Figure 2.5 further elucidate that the structure of the OCTC differs from that of the starting materials of

PNZ and TCNQ and is consistent with the simulated XRD pattern based on an ordered layered structure of a PNZ–TCNQ OCTC.<sup>[39]</sup> According to the structural model, all of the molecules are connected in a single layer by bondings between nitrogen and hydrogen atoms in PNZ and TCNQ.<sup>[39]</sup> (Figure 2.4a) It is also noted that the  $\pi$ – $\pi$  attractive force aids in maintaining the well-ordered stacking of the layers as the  $\pi$ – $\pi$  conjugation field can be built up between the layers.<sup>[19, 24-25]</sup> The presence of the strong intermolecular forces between the molecular entities is believed to aid in the facile room-temperature synthesis of PNZ–TCNQ OCTC with high yield and contribute to the stability of the crystal structure. In order to verify the existence of charge-transfer interaction from the structural rearrangement, color observation of the PNZ–TCNQ OCTC and its constituting monomers was firstly performed, as presented in Figure 2.6a.<sup>[26]</sup> Significant color change can be noticed from the samples with the powder dispersion in solutions (THF/H<sub>2</sub>O: v/v=5:95), giving a clue for the existence of charge-transfer interaction. However, there was no clear bathochromic shift of the absorbed peaks of the PNZ–TCNQ OCTC in the ultraviolet–visible (UV–vis) spectra, only exhibiting the slight peak occurrence in the 700–850 nm region (Figure 2.6b).<sup>[27]</sup> Therefore, further chemical analysis for confirming the charge-transfer interaction was conducted through FTIR and Raman spectroscopy, as illustrated in Figure 2.7. Degree of charge-transfer can be estimated from the chemical structure change of the constituting donor or acceptor molecules, which is originated from the partial electron transfer. The amount of the peak shift in FTIR<sup>[28]</sup> and Raman spectra<sup>[29]</sup> has a linear relationship with the degree of charge-

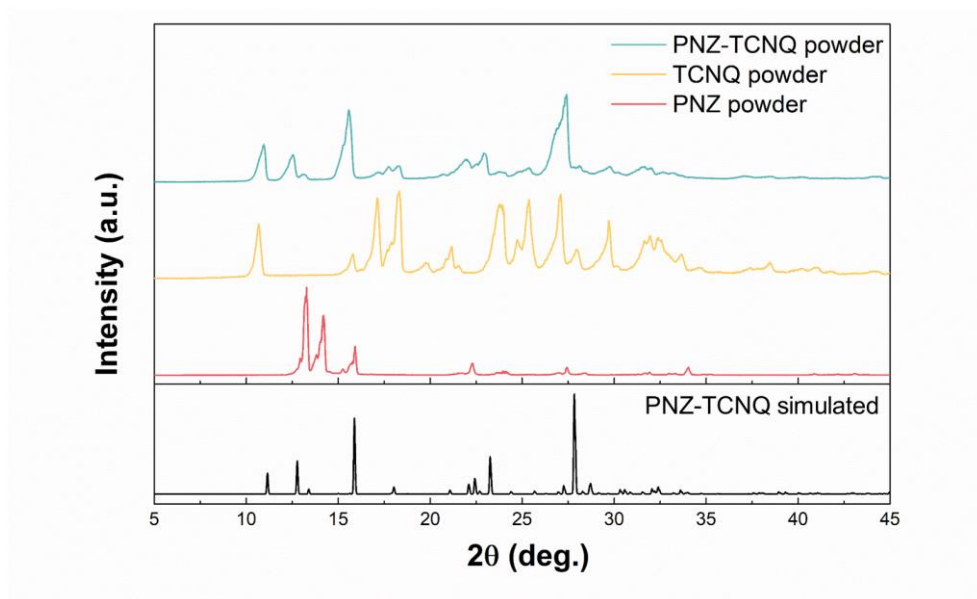
transfer, and the characteristic bonds in the TCNQ molecule part are treated as the standard for the estimation. First, peak shift, corresponding to the nitrile stretching mode of the TCNQ molecule, was observed through FTIR spectroscopy (Figure 2.7a). The slope of the linearity between the wavenumber of the characteristic peak and the degree of charge-transfer is suggested as  $-44\text{ cm}^{-1}$ . Therefore, the obtained degree of charge-transfer of PNZ–TCNQ OCTC is  $\sim 0.05$ , which is very small value. Second, peak shift, corresponding to the C=C bond stretching mode of the TCNQ molecule, was also observed through Raman spectroscopy (Figure 2.7b), and the obtained degree of charge-transfer is  $\sim 0.02$ . Although the estimating the degree of charge-transfer through chemical investigation has an imperfect reliability since it utilizes the empirical method, however, it can be stated that the PNZ–TCNQ OCTC has the only slight amount of electron transfer between the donor and acceptor molecules from the obtained data (Figure 2.6 and 2.7). It is speculated that the high degree of charge-transfer may affect the redox capability of the OCTCs since that the initial states of the donor and acceptor molecules are already in the oxidized or reduced state before battery cycling. However, the slight amount of electron transfer, that is, the small amount of charge-transfer interaction has a possibility to preserve the redox capability of constituting molecules in OCTCs as well as taking advantages of the structural characteristics of OCTCs.

Figure 2.8 compares the intrinsic material properties of the OCTC with those of PNZ and TCNQ. The electrical conductivity of the OCTC ( $8 \times 10^{-10}\text{ S cm}^{-1}$ ) was  $10^5$  and 20 times higher than those of PNZ and TCNQ, respectively,<sup>[42-43]</sup> and

represents remarkably high electrical conductivities among redox active organic materials reported. (Figure 2.3) This notable enhancement of the electrical conductivity after the formation of the OCTC agrees with the general observation for charge-transfer complexes that the structural aspect involving the  $\pi$ - $\pi$  interaction in the slab space typically results in the formation of a fast charge-transport path.<sup>[24-25]</sup> In addition, UV-vis spectroscopy analysis revealed that the dissolution of the OCTC was notably reduced compared with those of its precursor forms. Whereas the PNZ and TCNQ exhibited 9.1 and 5.6 mM solubility in tetraethylene glycol dimethyl ether (TEGDME) solvent after 6-hour storage at 60 °C (Figures 2.8 and 2.9), the OCTC was much more tolerant to the dissolution (2.3 mM solubility). The suppressed dissolution is mainly attributed to the strong intermolecular interaction in the OCTC and resulting large molecular matrix compared with those of the precursor molecules.<sup>[44-45]</sup>



**Figure 2.4 Detailed structural description of PNZ-TCNQ OCTC in the microscopic- and macroscopic-levels.** (a) Detailed structural information for PNZ-TCNQ. (dotted line: hydrogen bonds between molecules,  $\pi$ - $\pi$  interactions occur between the slabs). (b) SEM image of pristine PNZ-TCNQ powder.



**Figure 2.5** XRD patterns of PNZ–TCNQ, monomer units, and simulated PNZ–TCNQ.

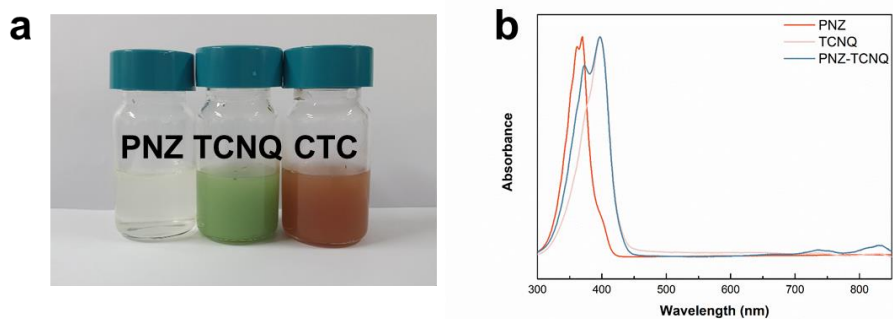


**Figure 2.6** Color characterization of PNZ–TCNQ and its constituting monomers. (a) Observed color change and (b) UV-vis spectra of powder dispersion (PNZ, TCNQ, and PNZ–TCNQ) in solutions (THF/H<sub>2</sub>O: v/v=5:95).

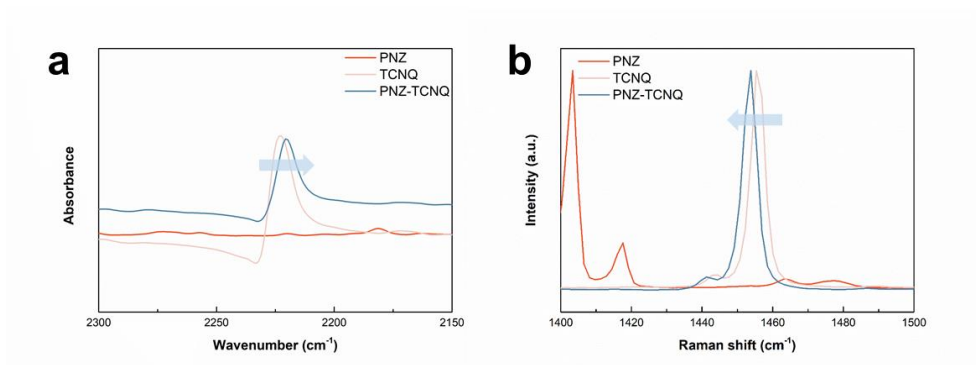


**Figure 2.7** Chemical investigation of PNZ–TCNQ and its constituting monomers.  
(a) FTIR and (b) Raman spectra of powders (PNZ, TCNQ, and PNZ–TCNQ)



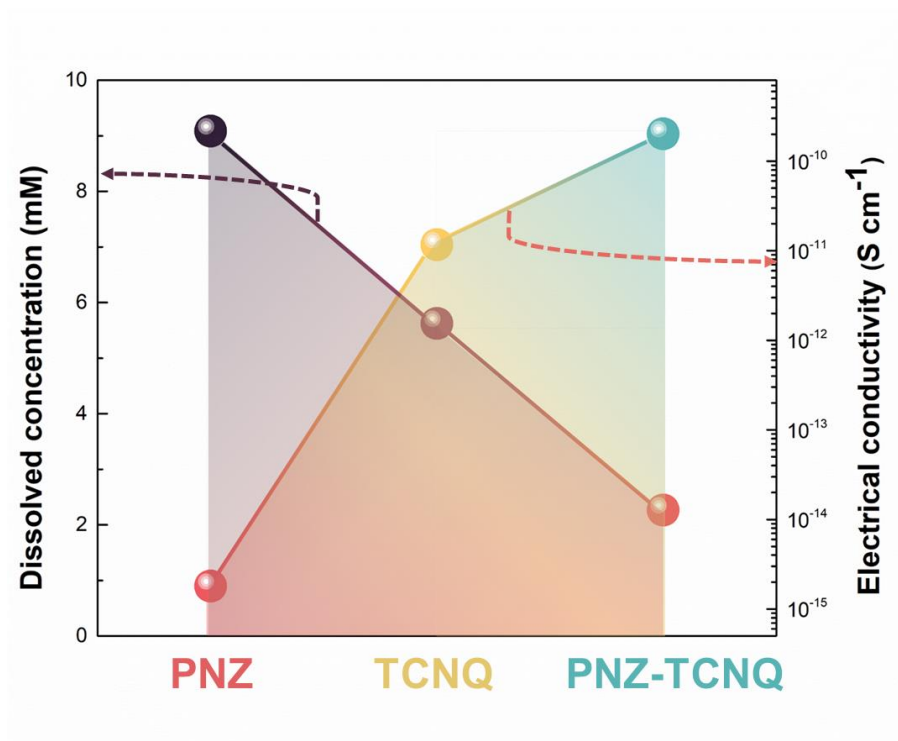


**Figure 2.8** Material properties of PNZ, TCNQ, and PNZ–TCNQ. Solubility with electrolytes measured using UV–vis spectroscopy after 6-h storage at high temperature (60 °C). The electrical conductivities were determined using four-probe measurements.

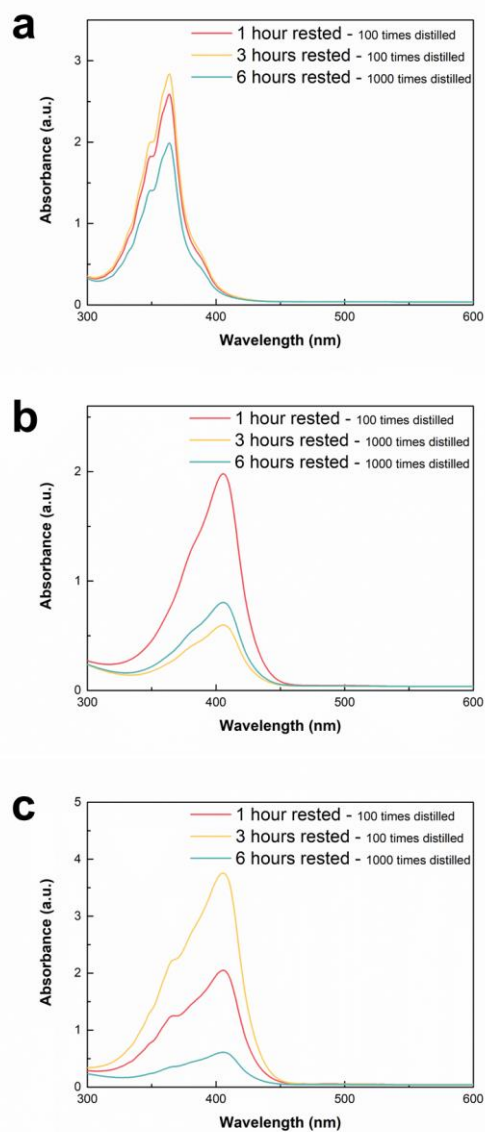


**Figure 2.9 Quantitative analysis of dissolution problem for organic electrode materials.** UV-vis spectra of (a) PNZ, (b) TCNQ, and (c) PNZ-TCNQ OCTC after 6-h storage at 60 °C. Related to Figure 2.8.

### 2.3.2 Electrochemical performances of PNZ–TCNQ

Preliminary electrochemical tests of the OCTC electrode were performed, and the second charge and discharge profiles of the PNZ, TCNQ, and PNZ–TCNQ OCTC electrodes in a lithium half-cell are shown in Figure 2.10 and Figure 2.11. Considering the theoretical capacities of PNZ and TCNQ (uptake of two lithium per formula unit), the PNZ and TCNQ electrodes retained approximately 50% and 75% of their theoretical capacities, respectively, at a current rate of  $50 \text{ mA g}^{-1}$ . This result partly agrees with previous reports of PNZ and TCNQ exhibiting relatively low capacities, which were attributed to their insulating nature.<sup>[40-41]</sup> However, at the same current rate, the OCTC electrode exhibited ~90% of the theoretical capacity. Although the cut-off voltage of the OCTC electrode was limited above 2 V and, thus, the PNZ part in the OCTC remained electrochemically inactive, the activity of the TCNQ part in the complex was notably enhanced.<sup>[46-47]</sup> (See Figure 2.12 for cycle data with the extended lower voltage cut-off.) Elucidating the origin of redox-inactive behavior of PNZ part and realizing full redox-activity through battery optimization are performed in Chapter 4. Figure 2.13 further supports the noteworthy improvement in the rate capability of the OCTC. The electrochemical profiles of the OCTC electrode at various current rates illustrate that the retention of the specific capacity was relatively stable even with the current density increase from 20 to  $500 \text{ mA g}^{-1}$ . The OCTC electrode exhibited ~73% capacity utilization at a current rate of  $500 \text{ mA g}^{-1}$  compared with that at  $50 \text{ mA g}^{-1}$ , corresponding to a capacity of 98 mAh

$\text{g}^{-1}$ . This rate performance is remarkable considering the large particle sizes ( $\sim 30\ \mu\text{m}$ ) of the OCTC in the electrode.

It should be noted that organic electrodes conventionally utilize a low active material content in the electrode (20%–60%) to compensate for the poor electrical conductivity.<sup>[5-7]</sup> In this respect, we also examined the electrode performance of the OCTC with various conductive carbon contents. Figure 2.14 presents the charge and discharge profiles of the OCTC electrodes with three representative carbon contents. As the carbon content decreased, the capacity of the OCTC electrode gradually decreased; however, the electrodes with 90 *wt.*% and 95 *wt.*% of active material could still deliver approximately 65% and 50% of the theoretical capacity, respectively. Most organic electrodes with such high active material contents and large particle sizes rarely exhibit electrochemical activity under these operating conditions.<sup>[8, 48-49]</sup> The cycle performances of the electrodes were further investigated, as shown in Figure 2.15. The OCTC electrode generally displayed improved capacity retention compared with those of the PNZ and TCNQ electrodes. The capacity retention of the OCTC electrode after 50 cycles was 43%, which is substantially higher than that of the TCNQ electrode (21%).

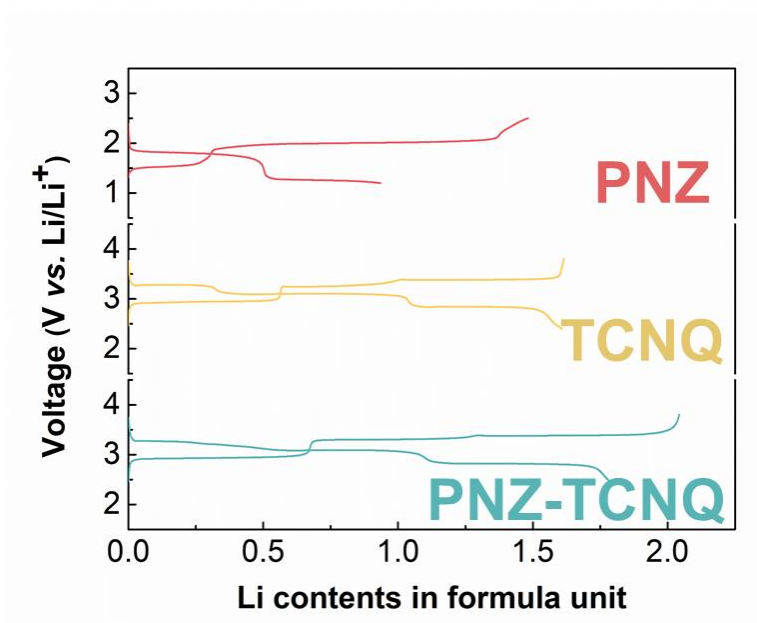


**Figure 2.10** Capacity–voltage profiles of monomolecules (PNZ, TCNQ) and charge-transfer complex (PNZ–TCNQ) during the second cycle.

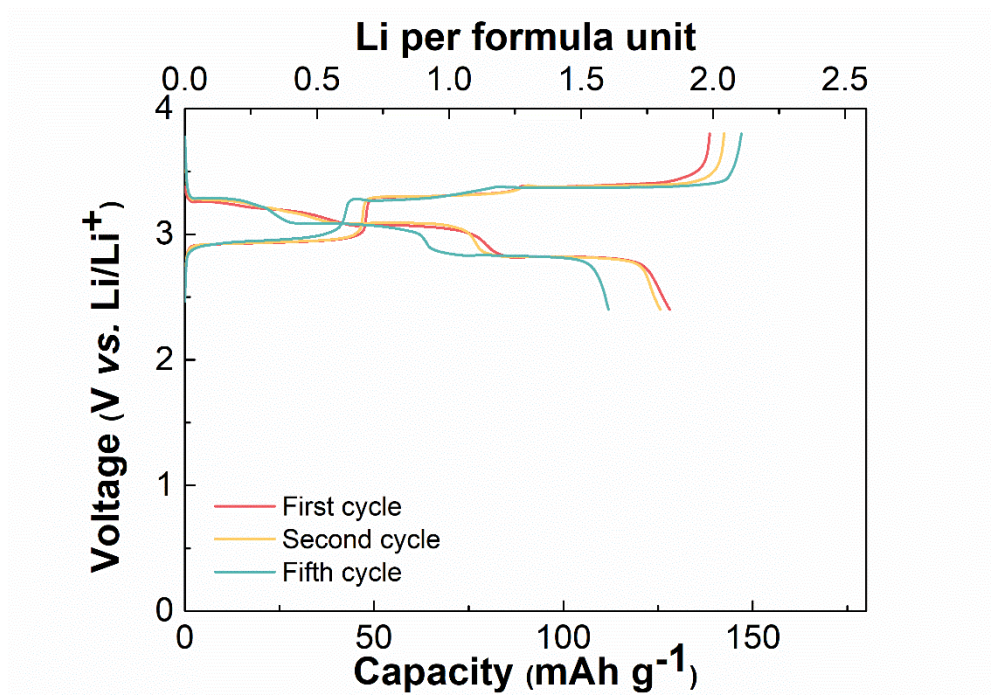


**Figure 2.11** Capacity–voltage profile of PNZ–TCNQ for 1, 2 and 5 cycles. Related to Figure 2.10.

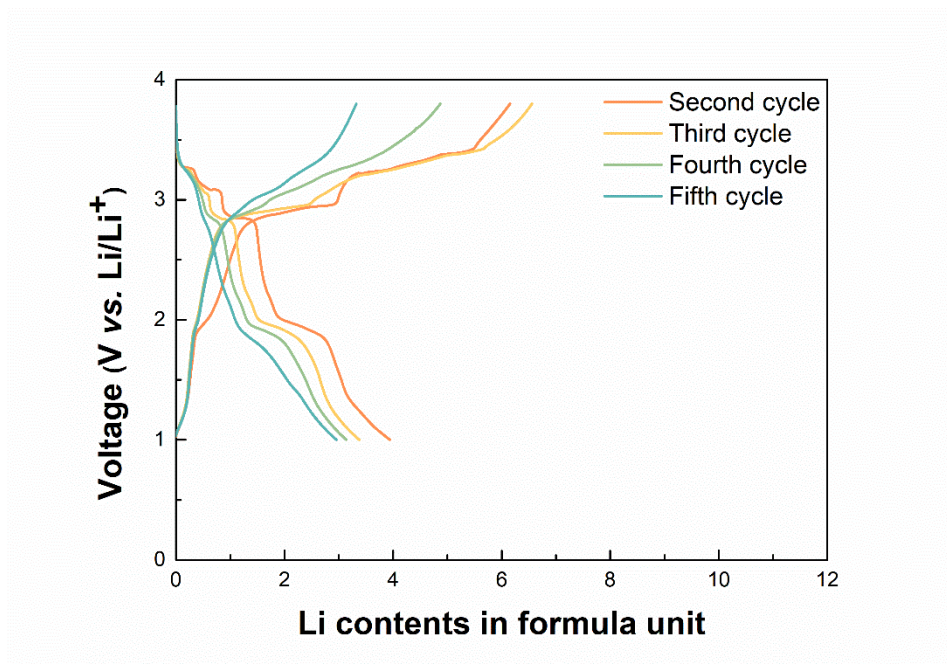


**Figure 2.12 Capacity–voltage profile for full activation of PNZ–TCNQ.**

Voltage–capacity curve of PNZ–TCNQ with the lower voltage limit of 1.0 V vs.  $\text{Li/Li}^+$  for 2–5 cycles.

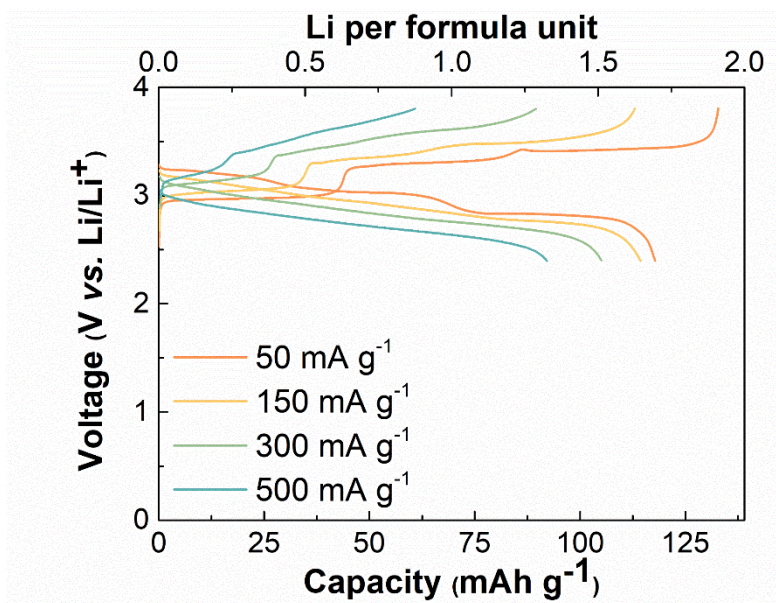


**Figure 2.13** Rate capability of PNZ-TCNQ at 50, 150, 300, and 500 mA g<sup>-1</sup>.



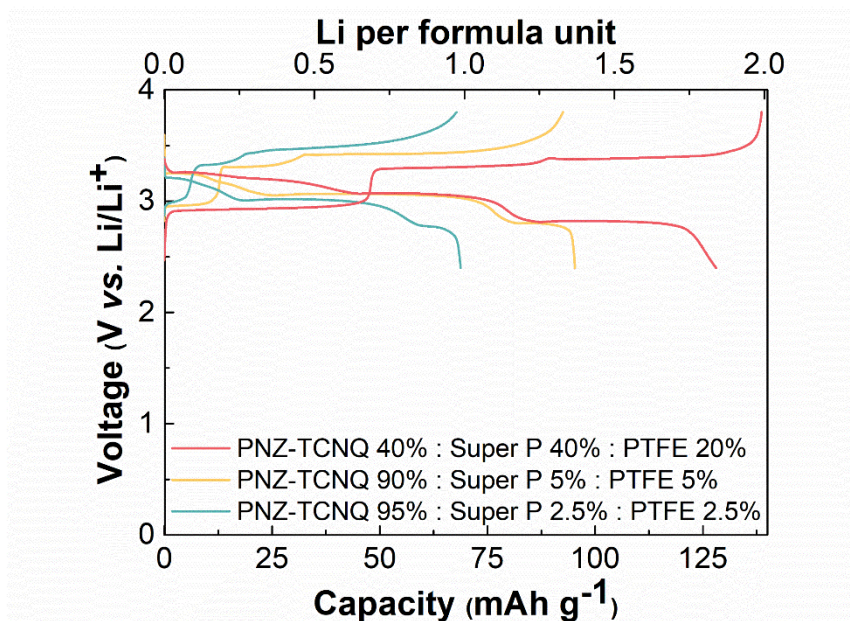


**Figure 2.14** Capacity–voltage profiles with high contents of active materials: 40 wt%, 90 wt%, and 95 wt% in total electrode.

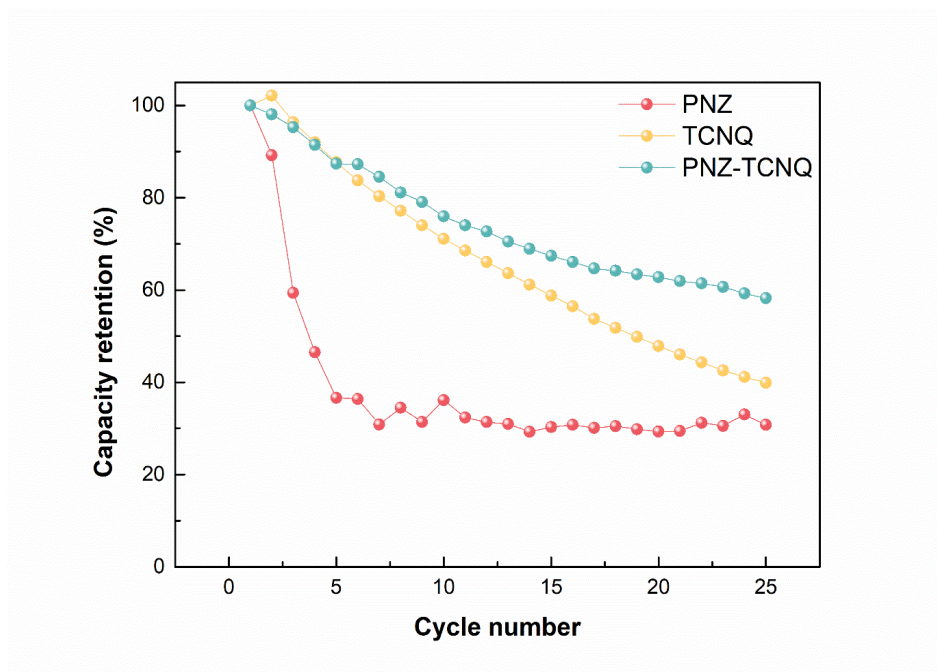


**Figure 2.15 Comparison of cyclability of charge-transfer complex and its monomer units.** Capacity retention curves of PNZ, TCNQ, and PNZ–TCNQ.

Related to Figure 2.18.

### 2.3.3 Strategy for enhancing the cycle stability of PNZ–TCNQ

PNZ–TCNQ OCTC showed the relatively higher capacity retention, however, there still exists capacity fading considered to be originated from continuous dissolution, low persistence of oxidized organics or another factor. First, it is speculated that it was not sufficient to sustain the stable cycling in the given electrolyte system from the *ex situ* UV–vis spectral analysis (See Figure 2.16 for more details). It is observed that the peak intensities of samples in the different state-of-charge are roughly similar, implying that the dissolution properties of the OCTCs at partially charged states are not significantly different from the pristine states. Nevertheless, it also indicated that small amount of dissolution is continuously observed regardless of the state-of-the charges, which may contribute cumulatively to the degradation of the capacity. Furthermore, post mortem analysis of the electrodes using FTIR in Figure 2.17 exhibited that the pristine PNZ–TCNQ was chemically stable after cycling, indicating no chemical degradation during charge/discharge processes. Nevertheless, the overall cycle performance requires further improvement, which might be attributed to the unusually large particle size (Figure 2.4b) and small amount of dissolution still observed in the OCTC (Figure 2.8). Particle size reduction and additional anchoring to a carbon nanotube (CNT) scaffold could further improve the capacity retention, and the OCTC electrode exhibited enhanced cycle stability, displaying 73% of the capacity after 50 cycles, and thus outperforming the TCNQ and PNZ electrodes.<sup>[50-51]</sup> (Figure 2.18) While more efforts need to be placed in improving the cycle stability of these TCNQ

derivatives in general, it clearly verifies that the charge-transfer complex formation enhances the cycle retention compared with those of its constituting respective organic molecules.

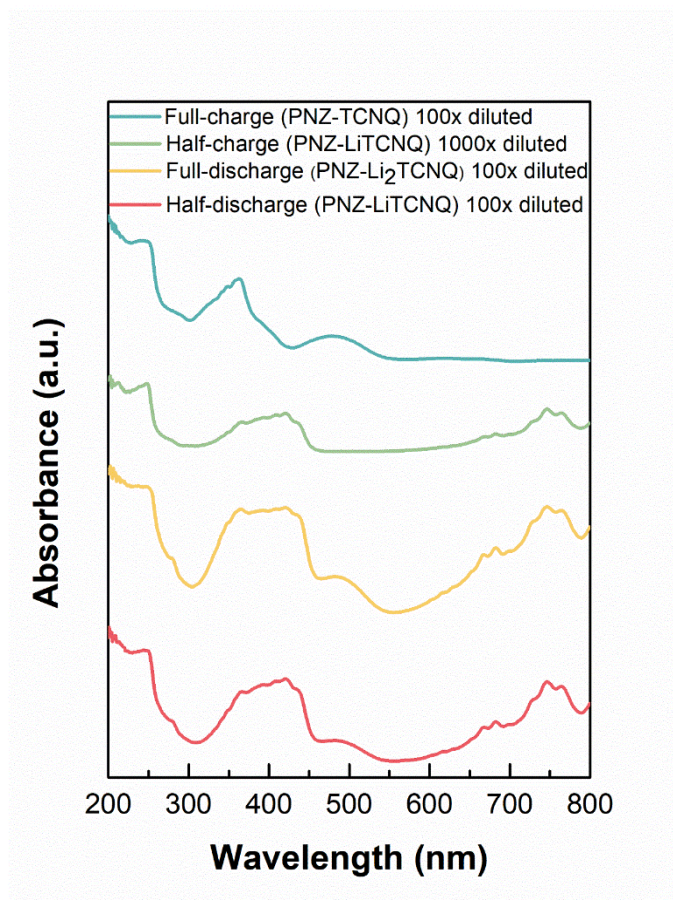


**Figure 2.16** *Ex situ* UV-vis analysis of OCTC electrodes during first cycle. *Ex situ* UV-vis spectra of OCTC electrodes for PNZ-TCNQ at the different state-of-charge.

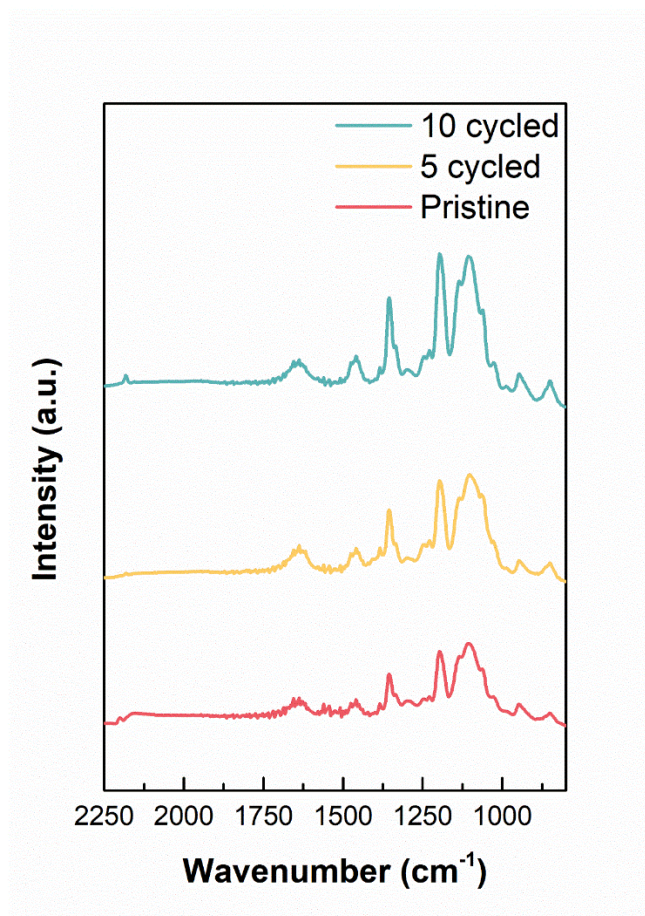


**Figure 2.17 Chemical reversibility of OCTC.** FTIR spectra of further cycled OCTC electrodes for PNZ-TCNQ.



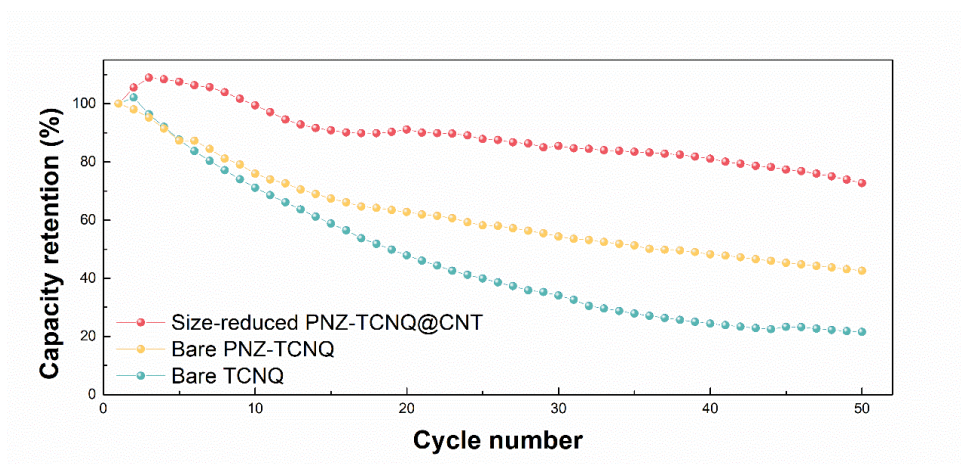


**Figure 2.18** Capacity retention curves of bare TCNQ, bare PNZ–TCNQ, and size-reduced PNZ–TCNQ aligned on CNTs.

## 2.4 Concluding remarks

In summary, we demonstrated the use of a charge-transfer complex as a novel type of organic electrode material for the first time. The formation of OCTCs from various organic redox compounds potentially results in several advantages for electrode materials in rechargeable battery chemistries. Because of the general structural characteristics of the charge-transfer complex, the electrical conductivity and structural integrity can be greatly improved. In particular, the firstly developed model PNZ–TCNQ OCTC has the low degree of charge-transfer, however, the electrical conductivity of the suggested OCTC (PNZ–TCNQ) exhibit remarkable high value among organic electrode materials reported to date and is comparable to that of transition-metal-oxide-based electrode materials. Even at a high current rate and using practical electrode formulation ratios, the new OCTC electrode retained respectable power and cycle performance. Various combinations of organic redox-active molecules can be considered for OCTCs to exploit different electron-accepting capabilities. Therefore, the integration of the distinct advantages of each organic redox-active moiety is expected to be possible by applying the charge-transfer complex strategy, resulting in improved electrical and structural properties. The electrochemical performance of the OCTC reported in this work, PNZ–TCNQ OCTC, is not yet comparable to that of currently used inorganic-based electrode materials. It is believed that to optimize the electrochemical performances, one need to further find the highly compatible electrolytes or utilize the conductive scaffold such as CNT and graphene. As various combinations of organic moieties are possible



to construct the organic charge transfer complexes, more appropriate material candidates in OCTCs which can better solve the dissolution and conductivity problems at the same time can be explored in the further work. The feasible formation of OCTCs from any molecule couples with different electron-accepting capabilities along with a future fundamental study on this new chemistry suggests the great promise for new organic electrode discovery via the exploration of numerous combinations of organic redox-active species. Moreover, the simple synthetic process of OCTCs *via* co-precipitation of two or more types of organic molecules in solvents at moderate temperature can offer additional merits.

## 2.5 References

- [1] J.-M. Tarascon, M. Armand, in *Materials for sustainable energy: a collection of peer-reviewed research and review articles from Nature Publishing Group*, World Scientific **2011**, p. 171.
- [2] B. Lee, K. Kang, *Nature* **2017**, 549, 339.
- [3] D. Larcher, J.-M. Tarascon, *Nature chemistry* **2015**, 7, 19.
- [4] M. Armand, J.-M. Tarascon, *nature* **2008**, 451, 652.
- [5] Y. Liang, Z. Tao, J. Chen, *Advanced Energy Materials* **2012**, 2, 742.
- [6] S. Lee, G. Kwon, K. Ku, K. Yoon, S. K. Jung, H. D. Lim, K. Kang, *Advanced materials* **2018**, 30, 1704682.
- [7] Z. Song, H. Zhou, *Energy & Environmental Science* **2013**, 6, 2280.
- [8] T. B. Schon, B. T. McAllister, P.-F. Li, D. S. Seferos, *Chemical Society Reviews* **2016**, 45, 6345.
- [9] M. Lee, J. Hong, J. Lopez, Y. Sun, D. Feng, K. Lim, W. C. Chueh, M. F. Toney, Y. Cui, Z. Bao, *Nature Energy* **2017**, 2, 861.
- [10] M. Lee, J. Hong, D. H. Seo, D. H. Nam, K. T. Nam, K. Kang, C. B. Park, *Angewandte Chemie International Edition* **2013**, 52, 8322.
- [11] X. Wu, S. Jin, Z. Zhang, L. Jiang, L. Mu, Y.-S. Hu, H. Li, X. Chen, M. Armand, L. Chen, *Science advances* **2015**, 1, e1500330.
- [12] D. Williams, J. Byrne, J. Driscoll, *Journal of The Electrochemical Society* **1969**, 116, 2.

- [13] H. Senoh, M. Yao, H. Sakaebe, K. Yasuda, Z. Siroma, *Electrochimica acta* **2011**, 56, 10145.
- [14] T. Le Gall, K. H. Reiman, M. C. Grossel, J. R. Owen, *Journal of power sources* **2003**, 119, 316.
- [15] Z. Song, H. Zhan, Y. Zhou, *Chemical communications* **2009**, 448.
- [16] Z. Song, H. Zhan, Y. Zhou, *Angewandte Chemie International Edition* **2010**, 49, 8444.
- [17] W. Choi, S. Ohtani, K. Oyaizu, H. Nishide, K. E. Geckeler, *Advanced Materials* **2011**, 23, 4440.
- [18] T. Sukegawa, K. Sato, K. Oyaizu, H. Nishide, *RSC Advances* **2015**, 5, 15448.
- [19] K. P. Goetz, D. Vermeulen, M. E. Payne, C. Kloc, L. E. McNeil, O. D. Jurchescu, *Journal of Materials Chemistry C* **2014**, 2, 3065.
- [20] J. B. Torrance, *Molecular Crystals and Liquid Crystals* **1985**, 126, 55.
- [21] J. R. Kirtley, J. Mannhart, *Nature materials* **2008**, 7, 520.
- [22] C. K. Sharma, R. Rogers, *Crystal engineering* **1998**, 1, 139.
- [23] Z. Soos, H. Keller, W. Moroni, D. Nöthe, *Annals of the New York Academy of Sciences* **1978**, 313, 442.
- [24] J. M. Schultz, *Properties of Solid Polymeric Materials: Treatise on Materials Science and Technology, Vol. 10*, Elsevier, **2017**.
- [25] Y. Qin, J. Zhang, X. Zheng, H. Geng, G. Zhao, W. Xu, W. Hu, Z. Shuai, D. Zhu, *Advanced Materials* **2014**, 26, 4093.

- [26] S. Oh, S. K. Park, B. H. Jhun, J. C. Roldao, J. H. Kim, M.-W. Choi, C. H. Ryoo, S. Jung, N. Demitri, R. Fischer, I. E. Serdiuk, R. Resel, J. Gerschner, S. Y. Park, *The Journal of Physical Chemistry C* **2020**, 124, 20377.
- [27] S. K. Park, I. Cho, J. Gierschner, J. H. Kim, J. H. Kim, J. E. Kwon, O. K. Kwon, D. R. Whang, J.-H. Park, B.-K. An, S. Y. Park, *Angewandte Chemie International Edition* **2016**, 55, 203.
- [28] J. S. Chappell, A. N. Bloch, W. A. Bryden, M. Maxfield, T. O. Poehler, D. O. Cowan, *Journal of the American Chemical Society* **1981**, 103, 2442.
- [29] S. Matsuzaki, R. Kuwata, K. Toyoda, *Solid State Communications* **1980**, 33, 403.
- [30] A. Aumüller, E. Hädicke, S. Hünig, A. Schätzle, J. U. von Schütz, *Angewandte Chemie International Edition in English* **1984**, 23, 449.
- [31] A. L. Sutton, B. F. Abrahams, D. M. D'Alessandro, T. A. Hudson, R. Robson, P. M. Usov, *CrystEngComm* **2016**, 18, 8906.
- [32] T. T. Fang, H. Y. Chung, *Journal of the American ceramic society* **2008**, 91, 342.
- [33] R. Guo, P. Shi, X. Cheng, Y. Ma, Z. Tan, *Journal of Power Sources* **2009**, 189, 2.
- [34] M. S. Whittingham, *Chemical reviews* **2004**, 104, 4271.
- [35] S. Horiuchi, T. Hasegawa, Y. Tokura, *Journal of the Physical Society of Japan* **2006**, 75, 051016.

- [36] G. Saito, Y. Yoshida, in *Unimolecular and supramolecular electronics I*, Springer **2011**, p. 67.
- [37] J. Ma, E. Zhou, C. Fan, B. Wu, C. Li, Z.-H. Lu, J. Li, *Chemical communications* **2018**, 54, 5578.
- [38] C. Fang, Y. Huang, L. Yuan, Y. Liu, W. Chen, Y. Huang, K. Chen, J. Han, Q. Liu, Y. Huang, *Angewandte Chemie* **2017**, 129, 6897.
- [39] I. Goldberg, U. Shmueli, *Acta Crystallographica Section B: Structural Crystallography and Crystal Chemistry* **1973**, 29, 440.
- [40] B. Tian, Z. Ding, G.-H. Ning, W. Tang, C. Peng, B. Liu, J. Su, C. Su, K. P. Loh, *Chemical Communications* **2017**, 53, 2914.
- [41] Y. Hanyu, I. Honma, *Scientific reports* **2012**, 2, 453.
- [42] S. Aftergut, G. Brown, *Nature* **1961**, 189, 827.
- [43] H. Afify, F. Abdel-Kerim, H. Aly, A. Shabaka, *Zeitschrift für Naturforschung A* **1978**, 33, 344.
- [44] C. Peng, G.-H. Ning, J. Su, G. Zhong, W. Tang, B. Tian, C. Su, D. Yu, L. Zu, J. Yang, *Nature Energy* **2017**, 2, 1.
- [45] D.-H. Yang, Z.-Q. Yao, D. Wu, Y.-H. Zhang, Z. Zhou, X.-H. Bu, *Journal of Materials Chemistry A* **2016**, 4, 18621.
- [46] A. Pei, G. Zheng, F. Shi, Y. Li, Y. Cui, *Nano letters* **2017**, 17, 1132.
- [47] J. Lu, Z. Chen, F. Pan, Y. Cui, K. Amine, *Electrochemical Energy Reviews* **2018**, 1, 35.

- [48] A. Shimizu, Y. Tsujii, H. Kuramoto, T. Nokami, Y. Inatomi, N. Hojo, J. i. Yoshida, *Energy Technology* **2014**, 2, 155.
- [49] T. Yokoji, H. Matsubara, M. Satoh, *Journal of Materials Chemistry A* **2014**, 2, 19347.
- [50] M. Lee, J. Hong, H. Kim, H. D. Lim, S. B. Cho, K. Kang, C. B. Park, *Advanced Materials* **2014**, 26, 2558.
- [51] Y. Wang, Y. Ding, L. Pan, Y. Shi, Z. Yue, Y. Shi, G. Yu, *Nano Letters* **2016**, 16, 3329.

## **Chapter 3. Exploiting the high voltage redox active molecules for the high energy density organic charge-transfer complex electrode.**

(The essence of this chapter has been published in Energy Storage Materials.

Reprinted with permission from [S. Lee *et al.*, *Energy Storage Mater.* **20**, 462

(2019)] Copyright (2020) Elsevier)

### **3.1 Research background**

In designing high-performance and sustainable batteries, the key technical barriers are to develop new electrode materials that are superior to current electrode materials.<sup>[1-2]</sup> Transition metal-based electrodes have been widely used because of their high energy density and reliable stability.<sup>[3-5]</sup> Nonetheless, mass production of batteries poses a serious problem in terms of the availability of the resources, particularly of the transition metals (*i.e.*, Co or Ni), on which the current battery technology heavily relies.<sup>[2, 6]</sup> Unlike conventional inorganic electrodes, organic compounds that can be obtained from earth abundant elements and thus cost-effective are highly desirable for pursuing sustainable electrodes.<sup>[7-9]</sup> In addition, the minimal carbon dioxide footprint associated with the recycling processes and the chemical tunability are their unique advantages.<sup>[8]</sup>

However, there are critical limitations of intrinsic material properties of organic electrode materials such as low electrical conductivity and high solubility to

solvent. To solve the chronic drawbacks of the organic redox-active compounds, it is highly required to develop the novel strategy to enhance the material properties with preserving the redox capability of the organic electrode materials. In the priorly reported work,<sup>[10]</sup> organic charge-transfer complex (OCTC), phenazine-7,7,8,8-tetracyanoquinodimethane (PNZ-TCNQ), was successfully utilized as a new material group for the electrode material in organic rechargeable batteries. PNZ-TCNQ OCTC electrode exhibited the improved material properties and electrochemical performances only through the molecular rearrangement in its own crystal structure. Although improved rate performance with acceptable cycle stability was successfully demonstrated by forming the OCTC from the PNZ and TCNQ, the electrochemical activity of the OCTC was displayed only from the TCNQ redox center. An attempt to discharge to lower voltage  $\sim 1$  V (*vs.* Li/Li<sup>+</sup>) to utilize the PNZ part in the complex induced side reactions in the electrochemical cell.<sup>[11-12]</sup> Accordingly, the energy density of the firstly developed OCTC electrode is still in low level compared to the currently-used inorganic electrode materials. This is also due to that the cell voltages rarely exceed 3.0 V *vs.* Li/Li<sup>+</sup> because of the inherently low redox potentials of *n*-type organic electrodes to serve as the electron acceptor, thus requiring additional inactive parts in battery pack design to meet the voltage specification.<sup>[9, 13-14]</sup> Therefore, efforts for alternating the PNZ part have been made to increase the redox potentials of OCTC by substituting heteroaromatic rings and adding electronegative functional groups, resulting in the high energy density.<sup>[15-16]</sup> However, only small elevation (0.1–0.4 V) of the voltage was attained with loss



of the theoretical capacity; the cell voltages are still not comparable to the current level. Moreover, most *n*-type organic compounds do not contain lithium in their natural state, and thus lithium-containing anodes (*e.g.*, lithium metal) must be employed to realize lithium-ion batteries (LIBs), raising other difficulties such as the explosiveness and the scarcity of the material.<sup>[8-9]</sup> Organic compounds with *p*-type redox properties, which serve as the electron donor, presents relatively higher redox potentials than the *n*-type counterparts and utilize molecular anions as charge carriers, offering freedom for the choice of the anode in the dual-ion battery system.<sup>[17-18]</sup> Despite improved performance, organic electrodes with the *p*-type redox reaction are not yet comparable in the redox potential to conventional inorganic electrodes exhibiting cell voltages of around 4.0 V *vs.* Li/Li<sup>+</sup>.<sup>[8]</sup>

Herein, we report a new 4.0 V class of *p*-type organic cathode based on dibenzo-1,4-dioxin (DD) as an alternative to the electron donor (PNZ) of the OCTC electrode. DD exhibits reversible single-electron redox reaction at the redox potential of 1.1 V *vs.* Ag/Ag<sup>+</sup>, which is one of the highest records among electrode materials. The demonstrated cell exhibits a reversible capacity of 90 mAh g<sup>-1</sup> with superior rate capability and the average cell voltage of 4.1 V *vs.* Li/Li<sup>+</sup>, which is the highest among redox-active organic moieties reported thus far. Its underlying redox mechanism is thoroughly investigated using spectroscopic tools combined with computational methods. Furthermore, following a similar mixing process as that used in the previous PNZ–TCNQ OCTC synthesis, we succeeded in fabrication a new OCTC based on DD (an electron donor) and TCNQ (an electron acceptor) at room

temperature. Material properties of DD–TCNQ OCTC significantly improved compared to the PNZ–TCNQ OCTC, exhibiting the highly increased electrical conductivity even comparable to the highest level of the state-of-the-art inorganic electrode materials. Full redox activation of both donor and acceptor molecule was also demonstrated with the three-electron redox reaction, further showing the enhanced energy density of  $560 \text{ Wh kg}^{-1}$  by the increased average cell voltage. We believe that our material design paves the way for the practical use of organic batteries by reducing its performance gap with the state-of-the-art inorganic batteries.

## **3.2 Experimental methods**

### **3.2.1 Preparation of materials**

DD was purchased from Alfa Aesar (USA), and TCNQ was purchased from Sigma-Aldrich (UK). All the commercially available chemicals were utilized without further purification. All air-sensitive manipulations were carried out under N<sub>2</sub>/Ar atmosphere by standard Schlenk-line techniques. The charge-transfer complex, DD–TCNQ, was synthesized following a procedure previously described in the literature.<sup>[19]</sup> The DD and TCNQ powders were mixed in an equimolar ratio in acetonitrile solvent for 30 min at room temperature, and the resulting solution was dried at 30 °C for 3 h.

### **3.2.2 Electrochemical measurements**

Solution samples were prepared and evaluated in an Ar-filled glove box under an inert atmosphere (< 0.5 ppm O<sub>2</sub>, H<sub>2</sub>O). Cyclic voltammograms of 5,10-dihydro-5,10-dimethylphenazine (DMPZ), thianthrene (TA), and DD (concentration = 10 mM) were obtained using 0.1 M LiClO<sub>4</sub> in EC/DMC (v/v 1:1). A three-electrode system (Pt counter electrode; Ag/AgNO<sub>3</sub> reference electrode; glassy carbon working electrode) was employed, and a scan rate of 100 mV s<sup>-1</sup> was used.

Capacity–voltage profiles of DD, DD–TCNQ, and its constituting molecules versus Li metal foil (Hohsen, Japan) were obtained in coin-type cells (CR2032). The Li metal anode was prepared in an Ar-filled glove box. The cathodes (6–8 mg) were

fabricated by mixing 40% (w/w) active materials, 40% (w/w) carbon black, and 20% (w/w) polytetrafluoroethylene (PTFE, Aldrich) binder. A porous glass microfiber membrane (GF/F; Whatman, UK) was used as a separator in the Li cells. The electrolyte was 5 M LiClO<sub>4</sub> in EC/DMC (1:1, v/v); the cells were assembled under inert atmosphere within an Ar-filled glove box. Electrochemical measurements were performed at a constant current density of 50 mA g<sup>-1</sup> in the voltage range of 2–4.3 V or 2.4–4.3 V versus Li/Li<sup>+</sup> using a battery test system (Won-A Tech, Korea).

### 3.2.3 Material characterization

XRD profiles of the powder samples of DD–TCNQ and its monomers were characterized using a D2 PHASER (Bruker, Bremen, Germany) equipped with Cu-K $\alpha$  radiation ( $\lambda$ = 1.54178 Å) at a scanning speed of 0.2° min<sup>-1</sup> in the 2 $\theta$  range of 5°–60°. The electrolytes with the stored electrode samples and the powder dispersed solutions (DD, TCNQ, and DD–TCNQ in THF/H<sub>2</sub>O: v/v=5:95) were characterized using a UV–vis spectrometer (Agilent Technologies, Cary 5000) with an optical glass cuvette (Quartz; Hellma®). FTIR spectra were measured using pellets made of the powders (DD, TCNQ, and DD–TCNQ) and KBr powder on an FT/IR-4200 (Jasco, Japan) at a resolution of 4 cm<sup>-1</sup>. Raman spectra were measured using powders of DD–TCNQ and its monomers on an LabRAM HR Evolution (Horiba, Japan). The fabricated electrodes of the DD–TCNQ series (DD–TCNQ and its monomer units) were stored in the electrolyte (5 M LiClO<sub>4</sub> in EC/DMC (v/v=1:1)) for 6 h at 60 °C. A lab-made four-probe station with an Agilent 4156C semiconductor parameter

analyzer was used to measure the electrical conductivities of the charge-transfer complexes and their constituting monomers. To evaluate the electrical conductivities, pelletized powders were prepared with thicknesses of ~3 mm.

### **3.2.4 *Ex situ* electrode characterization**

The electrodes of DD and DD–TCNQ at different states of cycling were prepared by disassembling coin cells followed by rinsing the electrodes with EC/DMC (v/v=1:1). XRD profiles were obtained using the D2 PHASER with Cu-K $\alpha$  radiation ( $\lambda = 1.54178 \text{ \AA}$ ) at a scanning speed of  $0.2^\circ \text{ min}^{-1}$  in the  $2\theta$  range of  $5^\circ$ – $60^\circ$ . The surface morphologies of the electrodes were examined using SEM (MERLIN Compact, ZEISS, Germany). XPS measurements were performed using an Axis Supra<sup>TM</sup> from Kratos (U.K.). All the measured spectra were set to the reference of C 1s (284.4 eV), which is correlated to the Super P. FTIR spectra were measured using pellets made of the electrodes at different states and KBr powder on an FT/IR-4200 (Jasco, Japan) at a resolution of  $4 \text{ cm}^{-1}$ . UV-vis spectra measurements were performed using an JASCO-3000 (Jasco, Japan) at a resolution of 10 nm.

### 3.3 Results and discussions

#### 3.3.1 Design concept and energy storage behavior of DD

The design of DD is inspired by the redox chemistry of 5,10-dihydro-5,10-dimethylphenazine (DMPZ), which undergoes a *p*-type redox reaction of ready-to-charge material with a high energy density.<sup>[20]</sup> DMPZ has a significant merit of high redox potential (3.4 V *vs.* Li/Li<sup>+</sup> in average potential) originating from the *p*-type redox reaction.<sup>[8, 21]</sup> However, it still could not reach the comparable level of currently used transition metal oxide-based electrode materials. It is highly required to increase the redox potential of organic electrode materials to make them feasible in terms of the energy density. DMPZ has a nitrogen-based redox center with electron donating methyl groups. In order to expand the redox potential window of this type of organic electrode materials, new molecular design strategy is suggested by replacing the redox-active atoms (Figure 3.1). The *sp*<sup>3</sup>-hybrid nitrogen atoms in DMPZ requires alkyl substituents that decrease the redox potential of the organic electrode materials. As an alternative, substitution of the ring-embedded redox-active heteroatoms to group 16 elements, such as sulfur and oxygen, would satisfy the octet rule without any additional functional groups. For example, sulfur-containing heterocyclic motif, such as thianthrene (TA), was employed as the redox-active component in polymers having high redox potential.<sup>[22]</sup>

We newly propose oxygen-containing heterocyclic compound, DD, as a high voltage *p*-type electrode material. Oxygen has higher electronegativity and

lower atomic weight than sulfur, thus exhibiting potential to have higher redox potential and theoretical capacity. From chemical point of view, DD is ideally structured to satisfy all the requirements to exhibit high redox potential in the tricyclic fused heterocyclic system without any additional functional groups. In addition, it is expected that the electrochemical reaction of DD would be reversible without deleterious side reactions from electron transfer because the electronic energy levels of DD and DD<sup>+</sup> lie within the electrochemical window of EC/DMC (v/v=1:1) solvent system (Figure 3.2). As shown in Figure 3.1, DD shows redox potential of 1.1 V *vs.* Ag/Ag<sup>+</sup> in cyclic voltammetry (CV) test, which is much higher than that of DMPZ or TA.<sup>[20, 22]</sup> It is noted that the suggested molecular design concept could increase the redox potential of organic electrode materials without any loss of theoretical capacity.

DD is a *p*-type redox active molecule, which undergoes anion insertion/deinsertion redox reaction during cycling. Molecular anions in the electrolyte approach the oxidized redox centers during charge process for charge balance and diffuse back to bulk electrolyte during discharge process. Therefore, it can be explained that the anions and cations in the electrolyte moves towards the opposite sides as charge carriers. Based on the knowledge of *p*-type redox active molecules, we fabricated a dual-ion rechargeable battery system with DD as a cathode, as schematically depicted in Figure 3.3. Cathode associates with the anion in the electrolyte during charging, indicating that DD is ready-to-charge even without any cation reservoir in the anode side for lithium or sodium ion batteries.

The electrochemical performance of DD was investigated in the dual-ion batteries based on lithium ions and molecular anions (perchlorate,  $\text{ClO}_4^-$ ) at 50 mA  $\text{g}^{-1}$  (Figures 3.4 and 3.5). DD exhibited reversible redox behavior with well-defined stable plateau with the average cell voltage of 4.10 V *vs.* Li/Li<sup>+</sup>, and it delivered discharge capacity of about 90 mAh  $\text{g}^{-1}$ . DD undergoes a single-electron redox process within the voltage range of 2.0–4.3 V versus Li metal anode. The redox potential of the single redox reaction of DD lies in the highest level among the representative electrode materials, such as LiCoO<sub>2</sub> or Li[Ni<sub>1/3</sub>Co<sub>1/3</sub>Mn<sub>1/3</sub>]O<sub>2</sub> (Figure 3.6).<sup>[8, 16, 20, 23-30]</sup> This discovery of 4 V-class organic cathode is the first time based on our knowledge, and it implies that the suggested molecular design strategy and dioxin motif could overcome the intrinsic drawback of relatively low redox potential of organic redox-active moieties. The rate capability was investigated with various current rates. DD showed 40 and 50 mAh  $\text{g}^{-1}$  even at the extremely high current rates of 1500 and 1000 mA  $\text{g}^{-1}$ , charging and discharging within only 4 and 6 minutes, respectively (Figure 3.7).

We further examined the structural changes and the electron transfer in DD redox-active moiety during the battery cycling using *ex situ* Fourier-transform infrared (FTIR) spectroscopy, X-ray photoelectron spectroscopy (XPS), and density functional theory (DFT) calculations. We measured the FTIR and XPS spectra of DD electrodes at the as-prepared, fully-charged, and fully-discharged states by recollecting the electrode samples from coin cells disassembled at each state. As shown in Figure 3.8, reversible changes of local bonding structures of DD were



observed especially for the C–O–C bonds involved in the C–O stretching modes,<sup>[31]</sup> which indicates that the electron uptake/loss is localized mainly at the C–O–C bonds.

The reversible shifts of the peak in the O 1s XPS spectra shown in Figure 3.9 also support the interpretation of the FTIR data. A positive peak shift of O 1s spectra in the fully charged state points to the notion that the oxidation state of the oxygen atom is increased with the loss of electron during charging. In other words, the oxygen atom indeed functions as a redox center in the DD motif. In addition to experimental studies, natural population analysis (NPA) by DFT computational studies allowed us to track the changes of the charge distribution of DD during the charging/discharging process. As shown in Figures 3.10 and 3.11, the most drastic changes occur at the oxygen atoms. This result is fully consistent with the results of FTIR and XPS analysis.

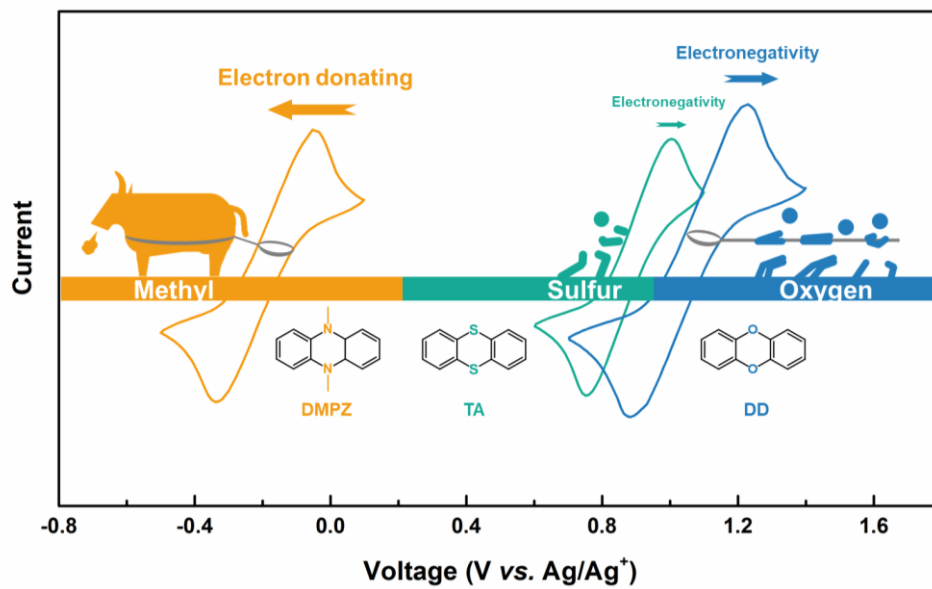


**Figure 3.1** Schematic diagram of the molecular design of DD.

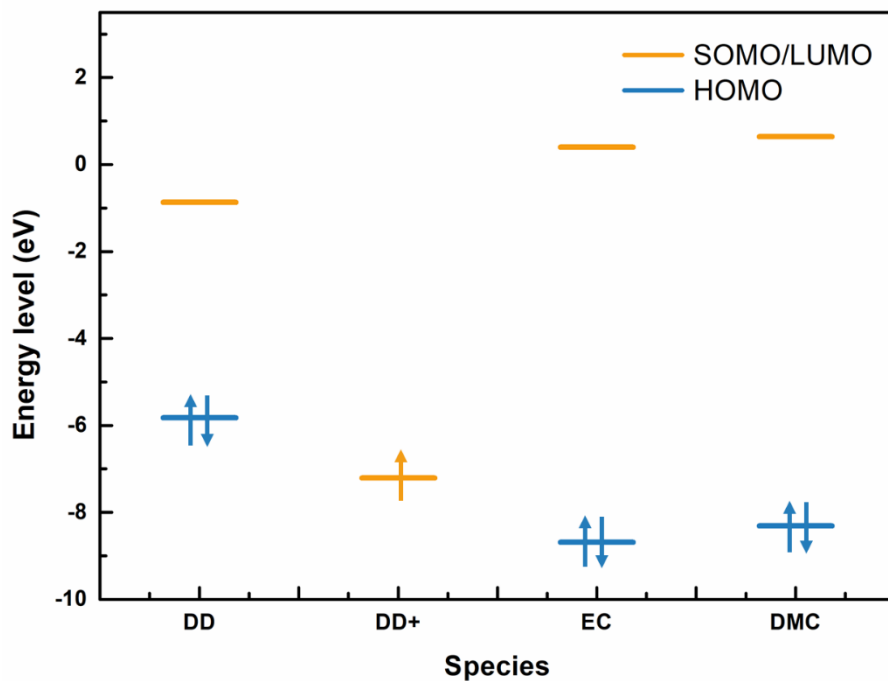


**Figure 3.2** Frontier molecular orbital (FMO) energies of DD, DD<sup>+</sup>, EC, and DMC. Note that the energy levels of DD change upon oxidation due to the relaxation effect of the molecules.

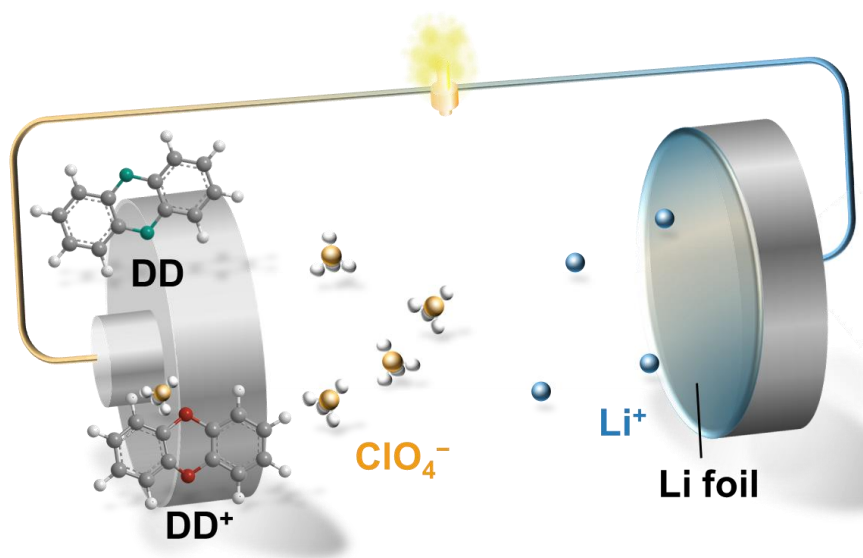


**Figure 3.3** Cell configuration of DD rechargeable battery.

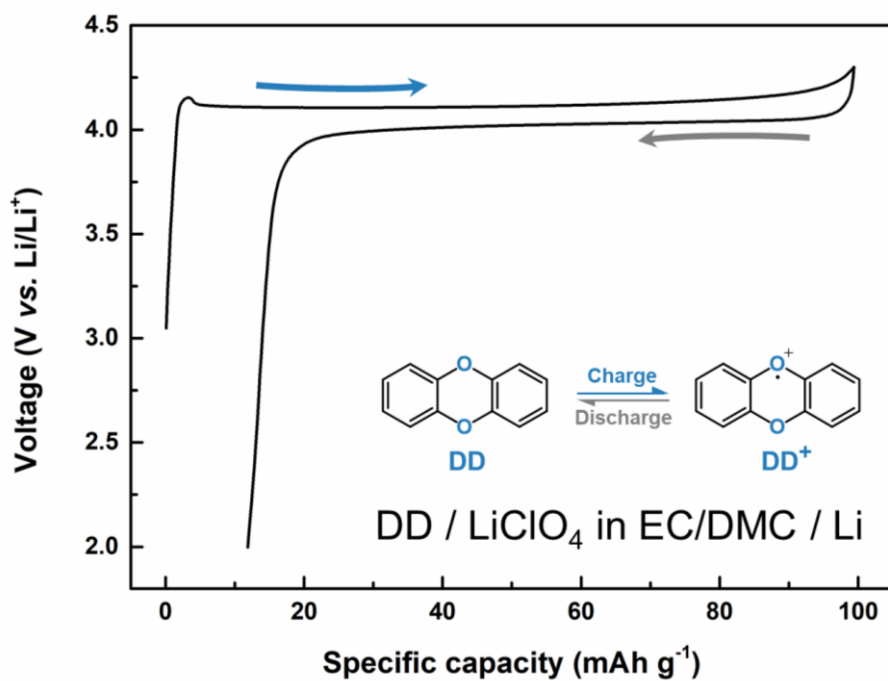


**Figure 3.4** Capacity–voltage profile of DD.

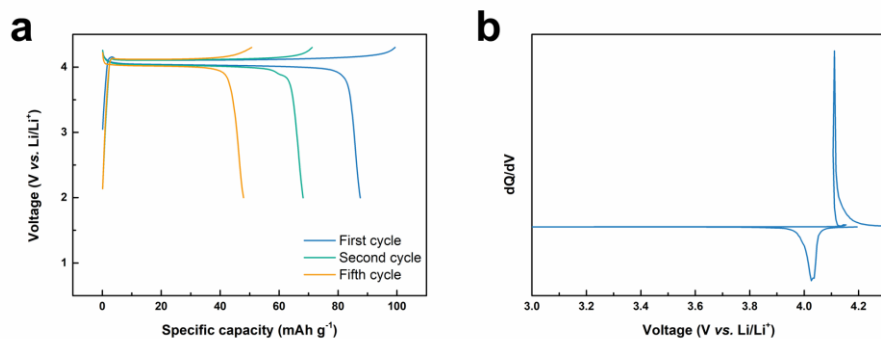


**Figure 3.5** (a) Capacity–voltage curve of DD for 1, 2, and 5 cycles. (b) Differential capacity ( $dQ/dV$ ) curve of DD.

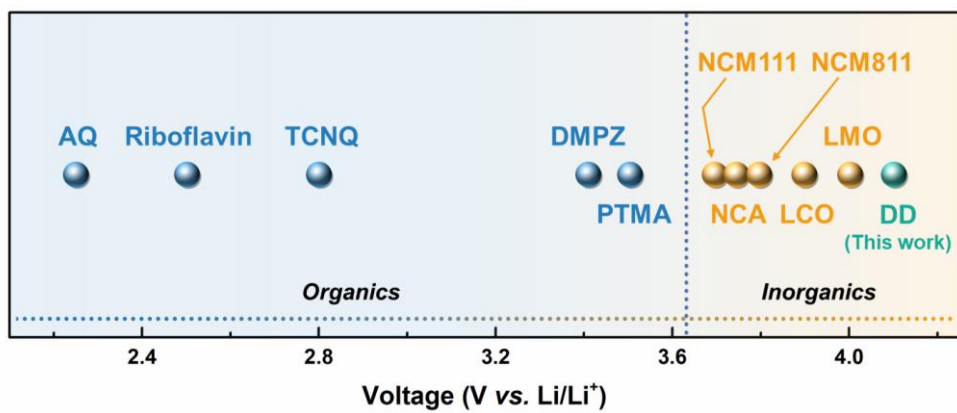


**Figure 3.6** Voltage comparison of representative cathode materials.

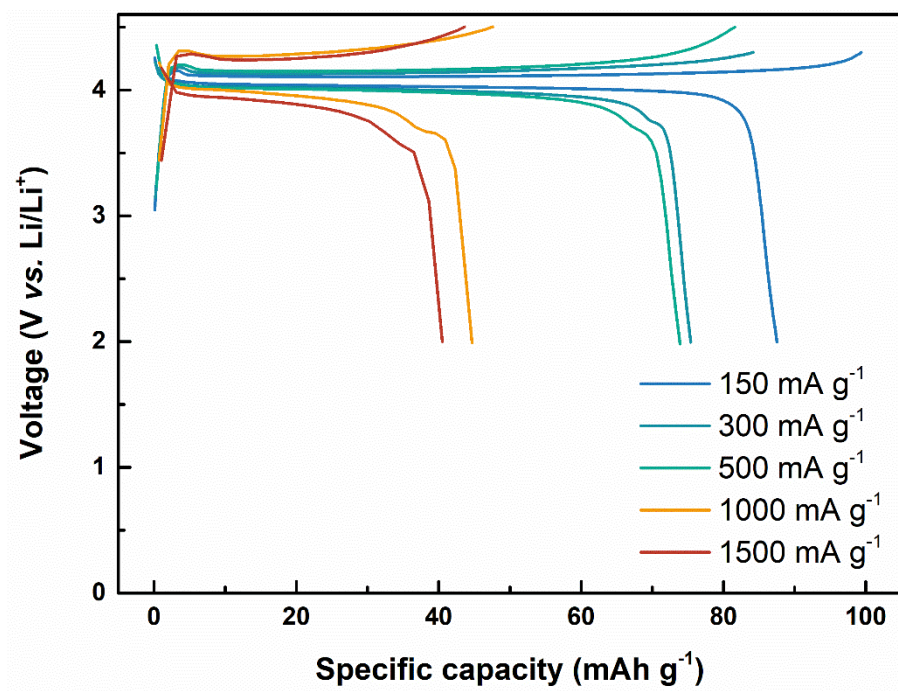


**Figure 3.7** Rate capability of DD at current density of 150, 300, 500, 1000, and 1500 mA g<sup>-1</sup>.



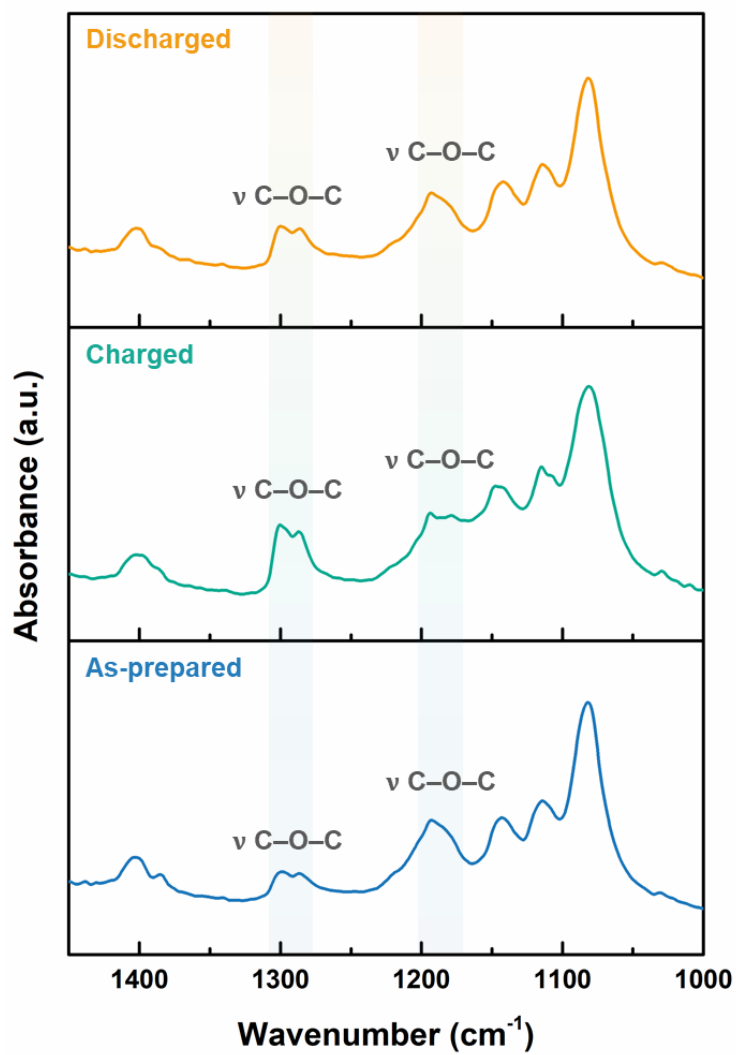


**Figure 3.8 Investigation of the redox mechanism of DD.** *Ex situ* Fourier-transform infrared (FTIR) spectra of DD.

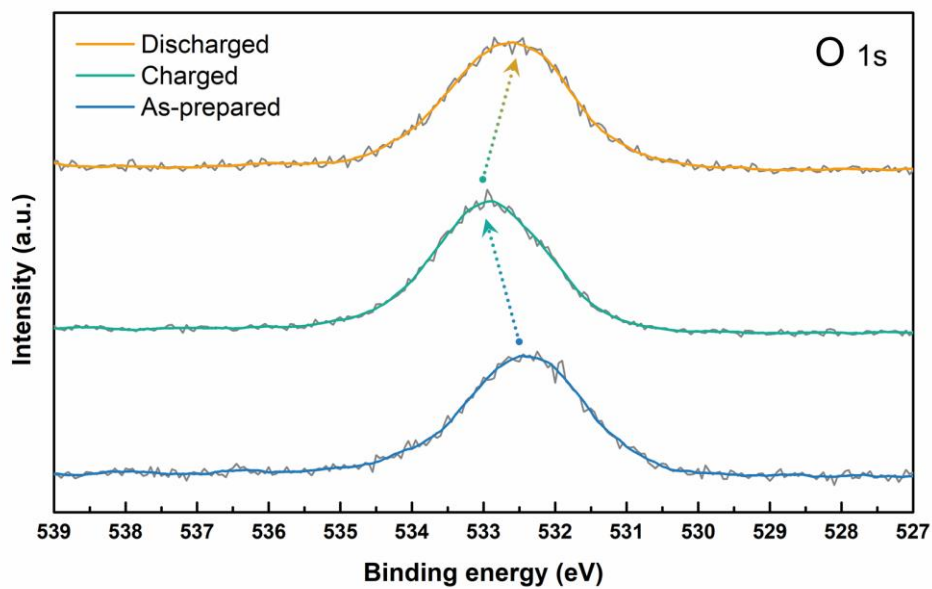


**Figure 3.9 Investigation of the redox mechanism of DD.** *Ex situ* X-ray photoelectron spectroscopy (XPS) spectra of DD.

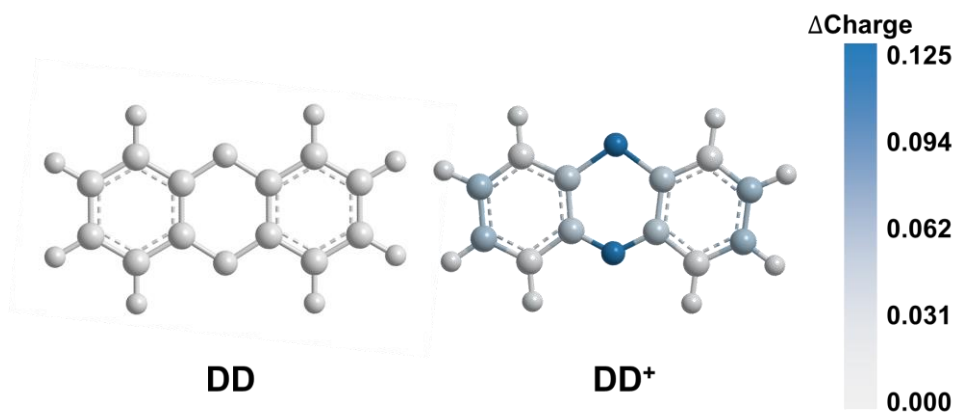


**Figure 3.10** Natural population analysis (NPA) of DD and DD<sup>+</sup>. The depth of the blue color denotes the extent of change in charge accompanying one-electron oxidation.

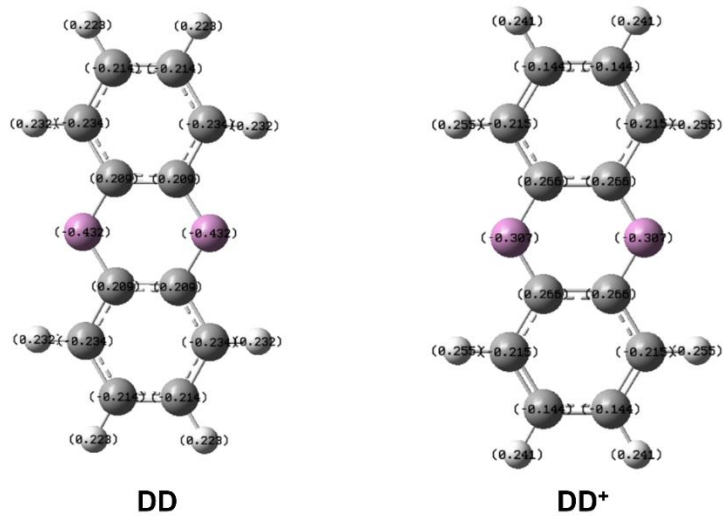


**Figure 3.11** Charge distribution calculations of DD and DD<sup>+</sup> using NPA.

### **3.3.2 Fabrication of DD–TCNQ electrode and its material and electrochemical properties.**

Following with a successful development of the high voltage organic cathode material, DD, we fabricated a new OCTC with the DD and TCNQ at room temperature as the similar mixing process that used in the PNZ–TCNQ OCTC synthesis. (Figure 3.12a) The structural analysis supports that the OCTC was successfully prepared from DD and TCNQ. The SEM image in Figure 3.12b confirms that well-ordered platelet particles were formed after the synthesis, and the XRD pattern of the obtained powder displays a diffraction pattern matched with the simulated pattern and is distinct from those of its precursors, as shown in Figure 3.13.<sup>[19]</sup> The structural merits of the OCTC were consistently observed for the DD–TCNQ OCTC as well. The existence of charge-transfer interaction of DD–TCNQ OCTC is further verified through color observation and UV–vis spectroscopy (Figure 3.14). Significant color change of the powder dispersed solution samples was observed as shown in Figure 3.14a, however, there was no bathochromic shift of the absorbed peaks of the DD–TCNQ OCTC in UV–vis spectra (Figure 3.14b). Further chemical investigation with FTIR and Raman spectroscopy revealed that DD–TCNQ OCTC also shows the low degree of charge-transfer less than 0.1 (Figure 3.15). In the FTIR spectra, peak shift, corresponding to the nitrile stretching mode of the TCNQ molecule, was observed as depicted in Figure 3.15a, and the degree of charge-transfer of DD–TCNQ OCTC is  $\sim 0.07$ , calculated from the reported relationship between the degree of charge-transfer and wavelength, which is very small value.

Next, estimated degree of charge-transfer of DD–TCNQ OCTC from Raman spectroscopy is also similar as the obtained value from FTIR spectroscopy,  $\sim 0.05$  (Figure 3.15b). These results of material characterization states that the DD–TCNQ OCTC has the only slight amount of electron transfer between the donor and acceptor molecules as the previously developed DD–TCNQ OCTC. Therefore, DD–TCNQ OCTC also have the possibility to have the nearly full redox capability of constituting monomers in OCTC, with preserving the structural advantages of OCTCs.

Furthermore, it is observed that the chemical states of each constituting monomers are well-maintained as presented from the series of UV–vis spectra (Figure 3.16). The UV–vis spectra of charge transfer complexes are consistent with those of constituents, indicating the formation of the complex from the precursor moieties without any side reactions. Figure 3.17 illustrates that the electrical conductivity increased remarkably with the formation of the DD–TCNQ OCTC to  $2.785 \times 10^{-7} \text{ S cm}^{-1}$ , which is more than  $10^4$  times greater than that of DD and TCNQ and is even higher than that of the PNZ–TCNQ complex. Notably, this value is comparable to those of conventional transition metal oxide-based electrode materials such as  $\text{LiMn}_2\text{O}_4$  and  $\text{LiNi}_{1/3}\text{Co}_{1/3}\text{Mn}_{1/3}\text{O}_2$ .<sup>[32–33]</sup> The solubility test in ethylene carbonate/dimethyl carbonate (EC/DMC) solvent for 6 h at 60 °C revealed that the dissolution of DD and TCNQ could also be simultaneously suppressed. (Figure 3.17) The DD–TCNQ OCTC exhibited a low solubility (2 mM) that was more than 5 and

8 times lower than that of DD (11 mM) and TCNQ (16.6 mM), respectively, under the same conditions.

The electrochemical properties of the DD–TCNQ OCTC electrode in a lithium cell were investigated to examine the change in the energy density and rate capability corresponding to the improved material properties. Figure 3.18 shows that the DD–TCNQ OCTC clearly exhibited the electrochemical activity of both DD and TCNQ at  $\sim 4.2$  V and  $\sim (3.2/2.6)$  V (vs. Li/Li<sup>+</sup>), respectively. Moreover, the complex utilizes a three-electron redox reaction from both the DD and TCNQ units in the structure, which is equivalent to the theoretical specific capacity of 207 mAh g<sup>-1</sup> and theoretical energy density of 683 Wh kg<sup>-1</sup> (when paired with Li metal and considering only the mass of the working electrode). (Figure 3.19) We observed that the high energy density of the new OCTC could also be retained at high current rates, as depicted in Figure 3.20. Even at a current rate of 1000 mA g<sup>-1</sup>, both the charge and discharge capacity could be stably maintained, delivering a specific capacity of 130 mAh g<sup>-1</sup>, which corresponds to 76% of the capacity at 50 mA g<sup>-1</sup>. Nevertheless, DD–TCNQ OCTC exhibited a relatively low cycle retention, which warrants further study to optimize it. (Figure 3.21). As DD electrode alone could not be cycled at all in the same electrolyte condition due to its severe dissolution problem, it is speculated that, while the dissolution of DD was mitigated in the form of DD–TCNQ, it was not sufficient to sustain the extended cycle in the given electrolyte system (See Figure 3.22 for more details). Regarding the intrinsic chemical stability of the electrode during cycles, post mortem analysis of the electrodes using FTIR were

additionally carried out as shown in Figure 3.23. It revealed that the pristine DD–TCNQ chemical structure was stably maintained after cycling, implying that the major origin of the capacity fade is not likely to be the thermodynamic instability of the electrode at different charging states.



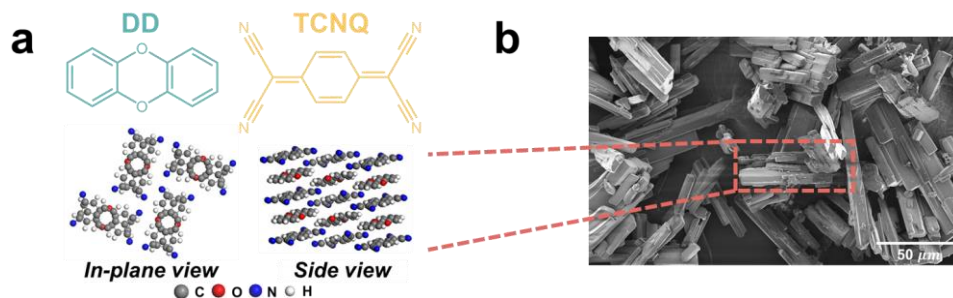


**Figure 3.12 Detailed structural description of PNZ–TCNQ OCTC in the microscopic- and macroscopic-levels.** (a) Chemical formula of DD and TCNQ and detailed structural information for DD–TCNQ: in-plane and side view ( $\pi$ – $\pi$  interactions occur between the slabs). (b) SEM image of pristine DD–TCNQ powder.

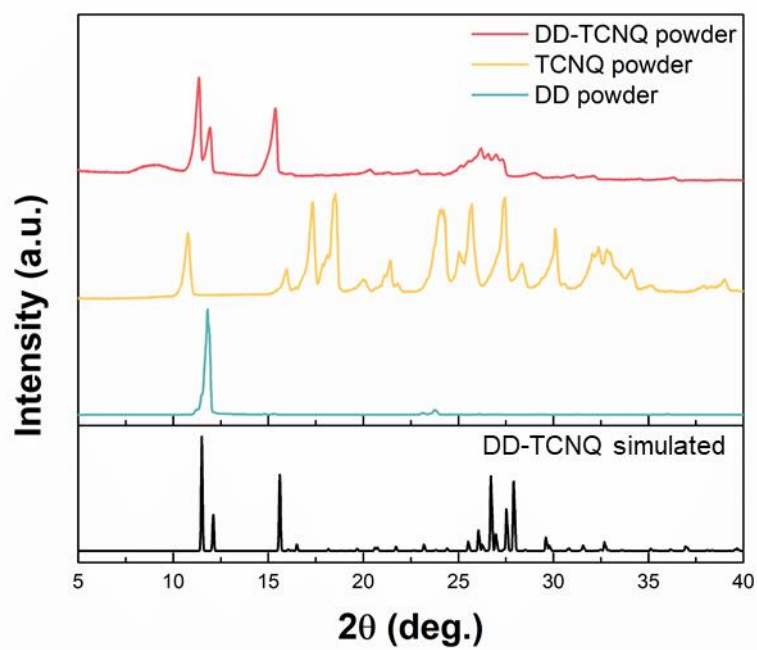


**Figure 3.13** XRD patterns of DD–TCNQ and its monomers and simulated pattern of DD–TCNQ.

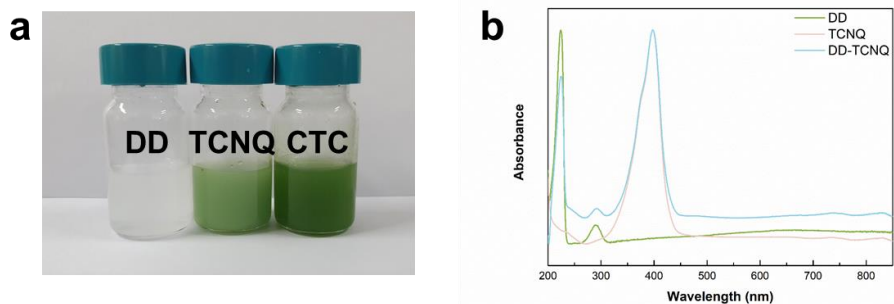


**Figure 3.14 Color characterization of DD–TCNQ and its constituting monomers.** (a) Observed color change and (b) UV-vis spectra of powder dispersion (DD, TCNQ, and DD–TCNQ) in solutions (THF/H<sub>2</sub>O: v/v=5:95).

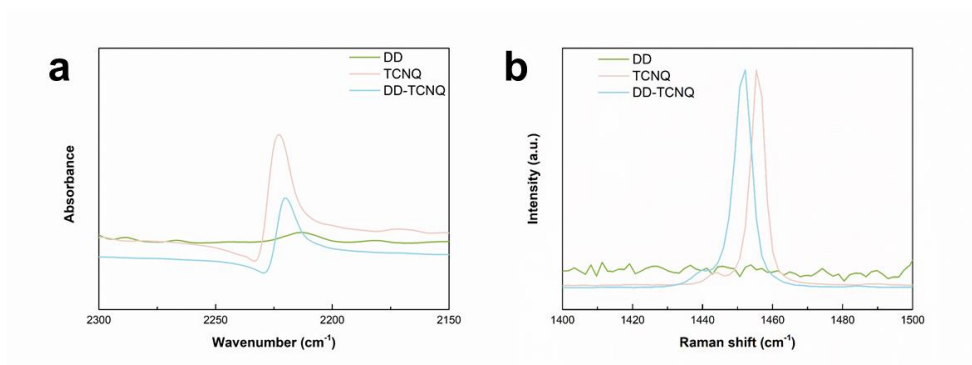


**Figure 3.15 Chemical investigation of DD-TCNQ and its constituting monomers.** (a) FTIR and (b) Raman spectra of powders (DD, TCNQ, and DD-TCNQ)

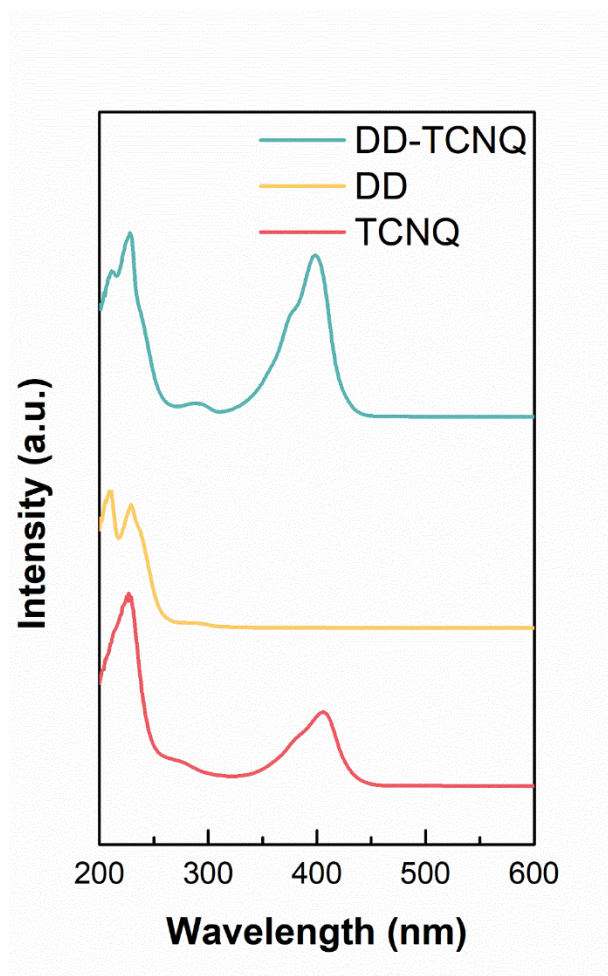


**Figure 3.16** UV-vis spectra of DD-TCNQ and their constituting monomers.

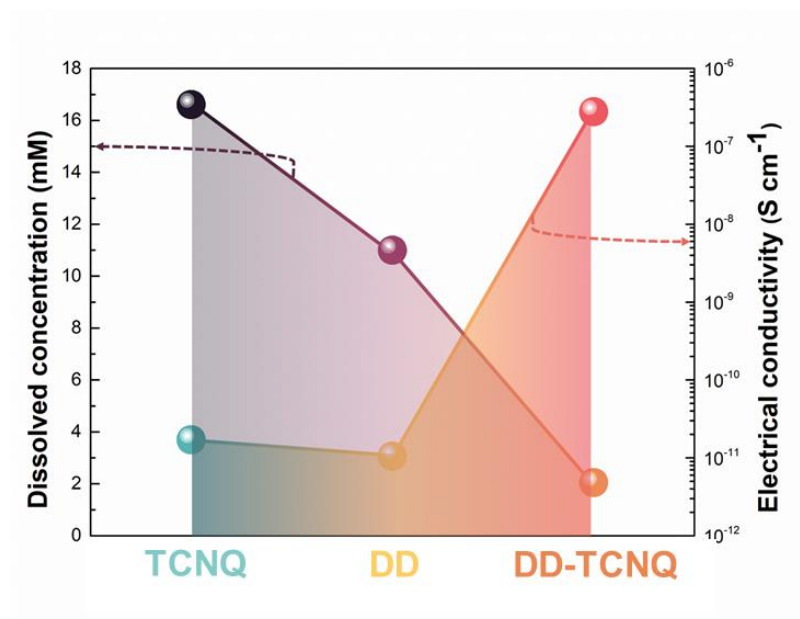


**Figure 3.17** Material properties of DD, TCNQ, and DD–TCNQ. Solubility with electrolytes measured using UV–vis spectroscopy after 6-h storage at high temperature (60 °C). The electrical conductivities were determined using four-probe measurements.

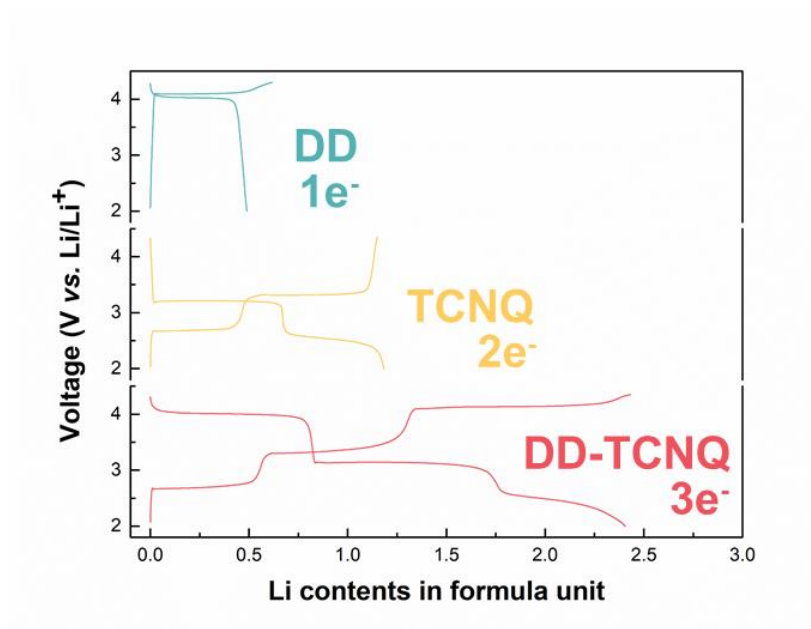


**Figure 3.18** Capacity–voltage profiles of monomolecules (DD, TCNQ) and charge–transfer complex (DD–TCNQ) during the second cycle.

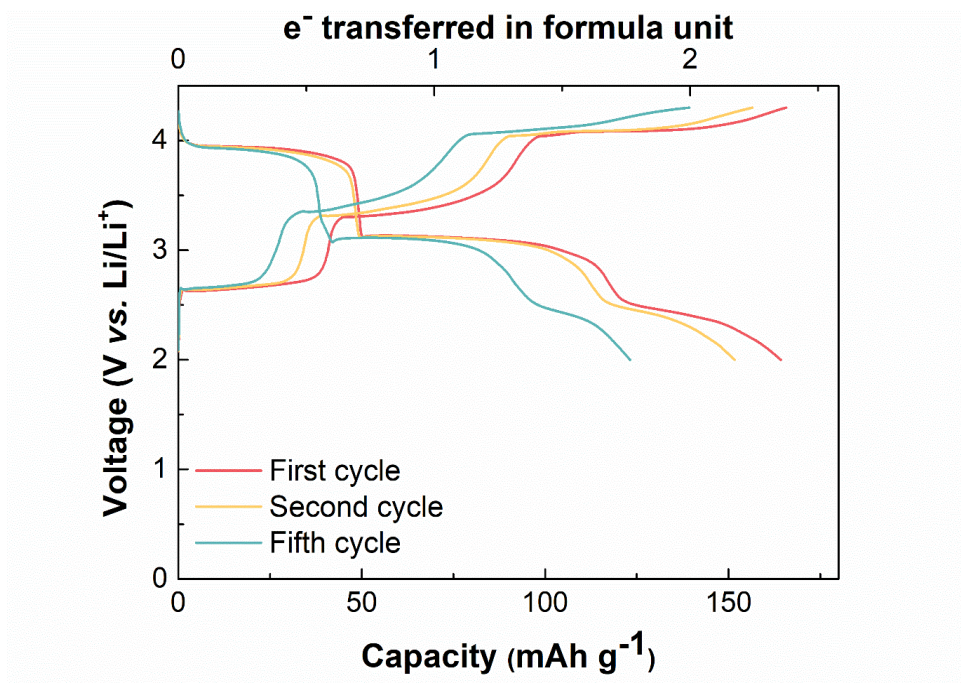


**Figure 3.19** Capacity–voltage profile of DD–TCNQ during the 1, 2 and 5 cycles.



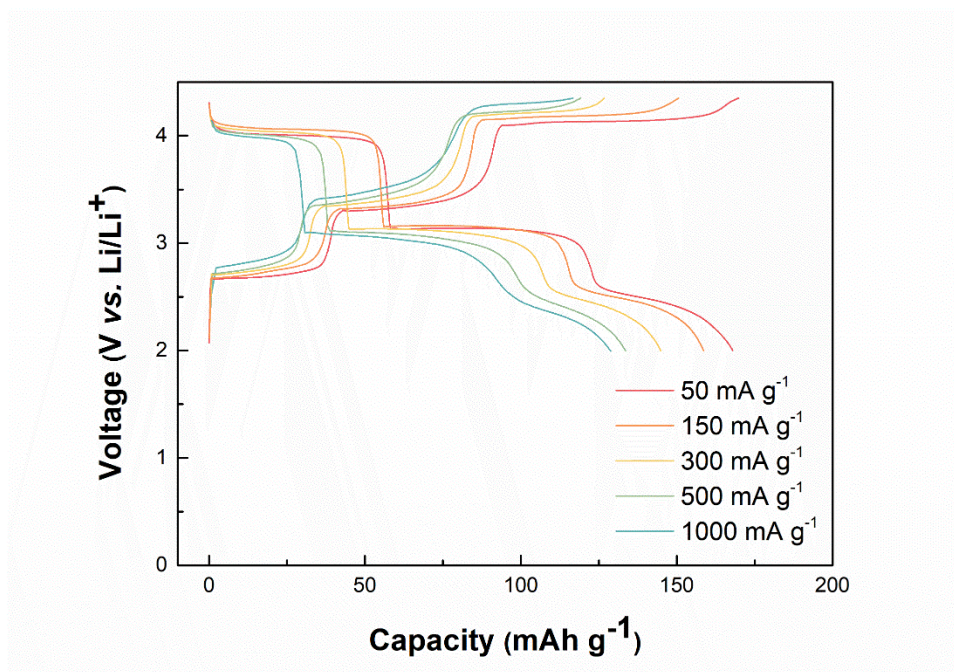


**Figure 3.20** Rate capability of DD-TCNQ at 50, 150, 300, 500, and 1000 mA g<sup>-1</sup>.

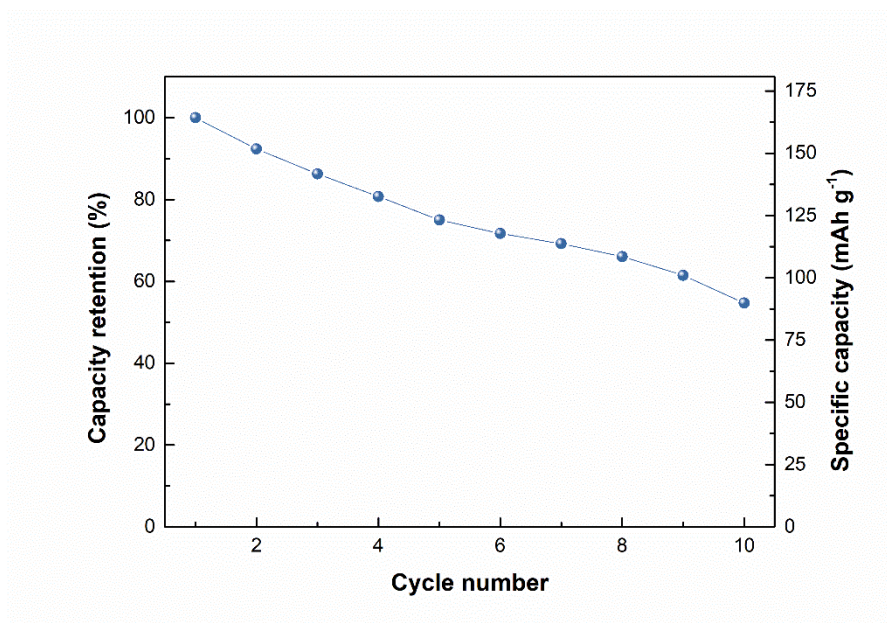


**Figure 3.21** Capacity retention curve of DD-TCNQ.

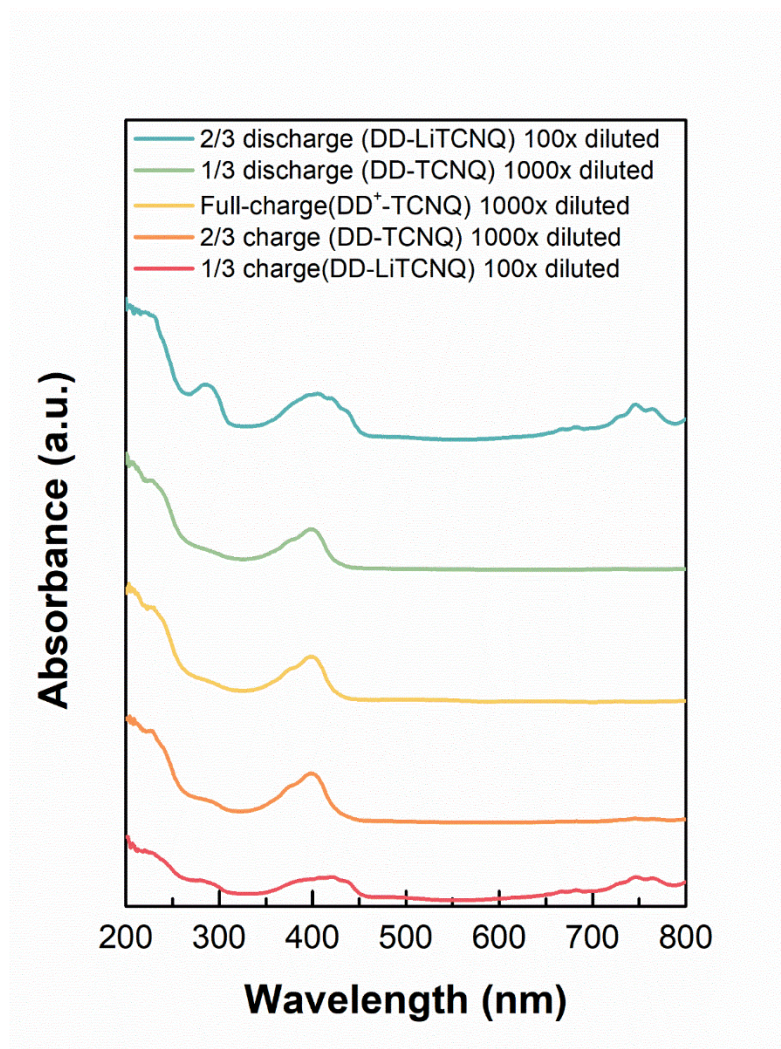


**Figure 3.22** *Ex situ* UV–vis analysis of OCTC electrodes during first cycle. *Ex situ* UV–Vis spectra of OCTC electrodes for DD–TCNQ at the different state-of-charge.

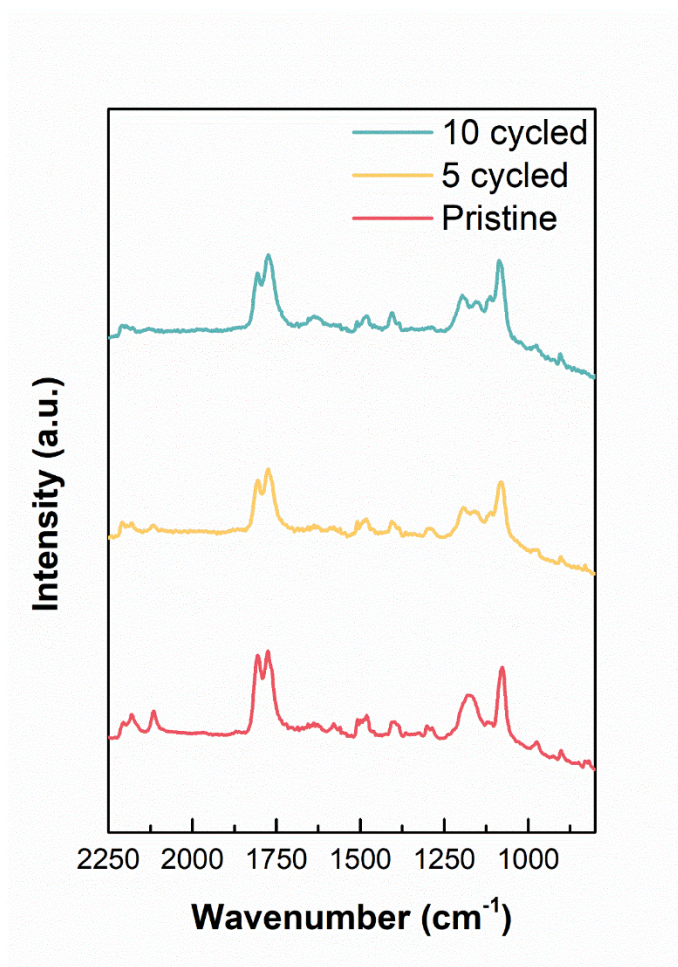


**Figure 3.23 Chemical reversibility of OCTCs.** FTIR spectra of further cycled OCTC electrodes for DD-TCNQ.

### 3.3.3 Redox mechanism of DD–TCNQ

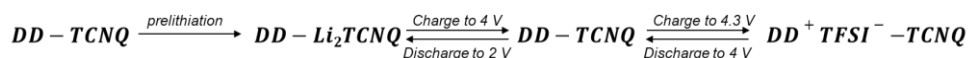
To verify the redox mechanism of this new organic electrode, the lithium cells were disassembled during charge and discharge at different states-of-charge and analyzed. The charge/discharge protocol was set to firstly discharge the electrode to 2.2 V vs. Li/Li<sup>+</sup>, and then charged and re-discharged within 4.3–2.2 V, as shown in Figure 3.24. The electrochemical cycle and the corresponding analysis presented in Figures 3.25, 3.26, and 3.27 begins with the fully discharged state of DD–TCNQ, DD–Li<sub>2</sub>TCNQ, followed by the charge and re-discharge. Figures 3.25, 3.26, and 3.27 shows the *ex situ* FTIR spectroscopy spectra and X-ray photoelectron spectroscopy (XPS) spectra at each end of the voltage plateaus during the second cycle. The FTIR spectra in Figure 3.25a illustrates the negative shift of C≡N stretching and its splitting into two peaks at 2200 cm<sup>-1</sup> and 2180 cm<sup>-1</sup> during discharge below the 4-V region, which are restored during the charge (from state 4 to state 7 in Figure 3.24). Nitrile bond breaks down to double bond after that nitrogen atom gets an electron (and a lithium ion) during discharge, and the neighboring C–C bond becomes a double bond. During charge to 4 V, the peaks positively shifted back to its original wavenumber (~2225 cm<sup>-1</sup>), indicating the recovery of the nitrile bond of the TCNQ unit. However, the reverse behavior was observed during discharge, which is attributed to the lithium insertion accompanying the reduction in the C≡N triple bond and suggests that the main redox reaction below 4 V occurs at the TCNQ part in the complex. This observation also agrees with the previously



reported redox mechanism of TCNQ, which indicates that TCNQ follows a reversible aromatization mechanism.<sup>[24]</sup> In contrast, a notable change in the C–O–C vibration at  $1280\text{ cm}^{-1}$  was observed above 4 V, as indicated by the dotted circle in Figure 3.25b. The generally positive shift of the C–O–C vibration suggests that the oxidation occurs near the C–O–C bond in the DD part, identifying this moiety as the redox center in the complex above 4 V.

A more detailed picture of the redox mechanism can be obtained from the XPS results in Figure 3.26. The N 1s spectra in Figure 3.26a shows that the ratio of the two peaks centered at 399.9 and 398.5 eV, corresponding to  $\text{C}\equiv\text{N}$  and  $\text{C}=\text{C}=\text{N}$  groups in the as-prepared electrode, respectively, reversibly changes, where the  $\text{C}=\text{C}=\text{N}$  peak gradually disappears with charging and reappears with discharging. Notably, the change in the  $\text{C}=\text{C}=\text{N}$  peak is not observed above 4 V, indicating the absence of the redox reaction of TCNQ. The C 1s spectra in Figure 3.26b, however, offers information on the redox activity above 4 V. It is clear that the  $\text{C}^+\text{--O--C}$  peak at 286.2 eV emerges significantly with charging and disappears upon discharge above the 4-V region. In addition, the C–O–C peak (286.0 eV) slightly shifts to the  $\text{C}^+\text{--O--C}$  peak at 286.2 eV, which is consistent with the FTIR result and confirms that the redox activity is centered at C–O–C in the DD part of the complex. Nevertheless, we only observed a negligible change in the O 1s peak, which is not fully understood and requires more detailed analysis of the redox mechanism of DD. (Figure 3.27) The current spectroscopy results suggest that DD undergoes a single-

electron redox reaction above the 4-V region, whereas TCNQ undergoes a two-electron redox reaction below the 4-V region during battery cycling. At each stage of charge and discharge, it is proposed that the original state of the DD–TCNQ OCTC transforms to DD–LiTCNQ, DD–Li<sub>2</sub>TCNQ, and DD<sup>+</sup>–TCNQ, as denoted in Figure 3.28. It can be summarized that the DD in the OCTC has an anion uptake/loss with *p*-type redox, and on the other hand, TCNQ in the OCTC participates an *n*-type redox reaction with a lithium uptake/loss. The detailed redox mechanism of DD–TCNQ is illustrated in equation 1.



**Equation 1.** Suggested redox mechanism of DD–TCNQ.

These series of observations confirm that DD and TCNQ, the constituents of the DD–TCNQ OCTC, fully participate in the redox reaction, resulting in the enhanced energy density of the OCTC. Furthermore, the formation of the OCTC is proposed as a viable approach to combine the electrochemical activities of the two different organic redox compounds into one structure with the additional benefits of enhanced electrical conductivity and structural stability.

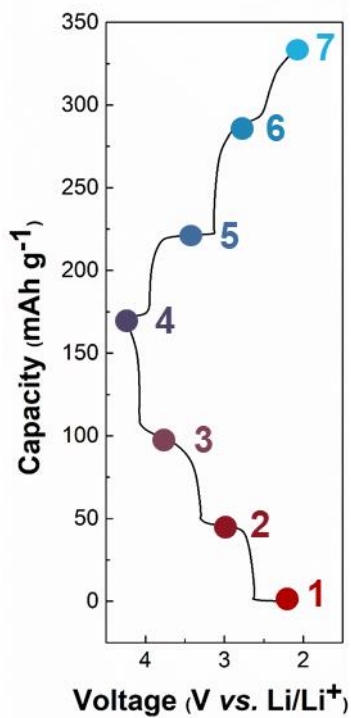


**Figure 3.24** Capacity–voltage profile of DD–TCNQ. Numbers (1-7) denote the electrode samples at each state-of-charge related to Figure 3.25, 3.26, 3.27, and 3.28.



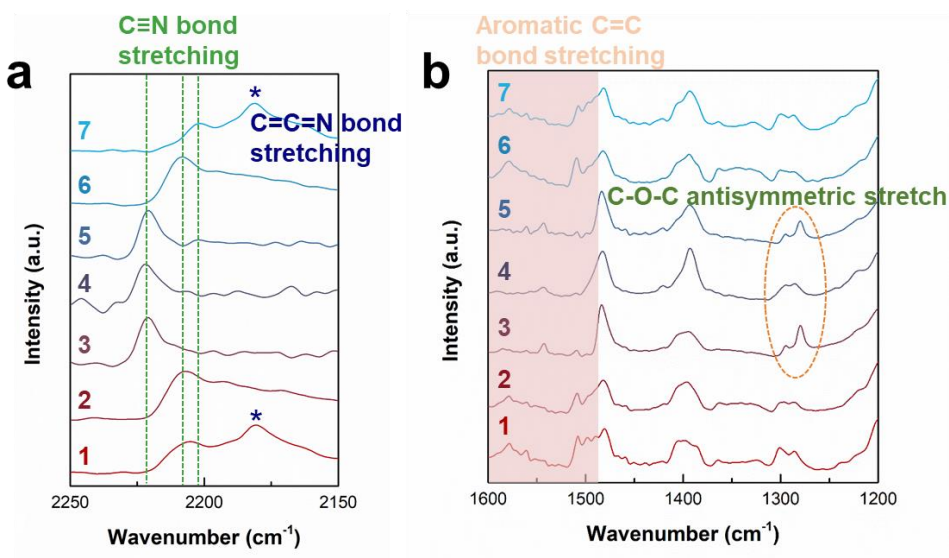


**Figure 3.25** *Ex situ* FTIR data in the regions of (a) 2250–2150  $\text{cm}^{-1}$  and (b) 1600–1200  $\text{cm}^{-1}$ . The numbered labels are the same as those in Figure 3.24.

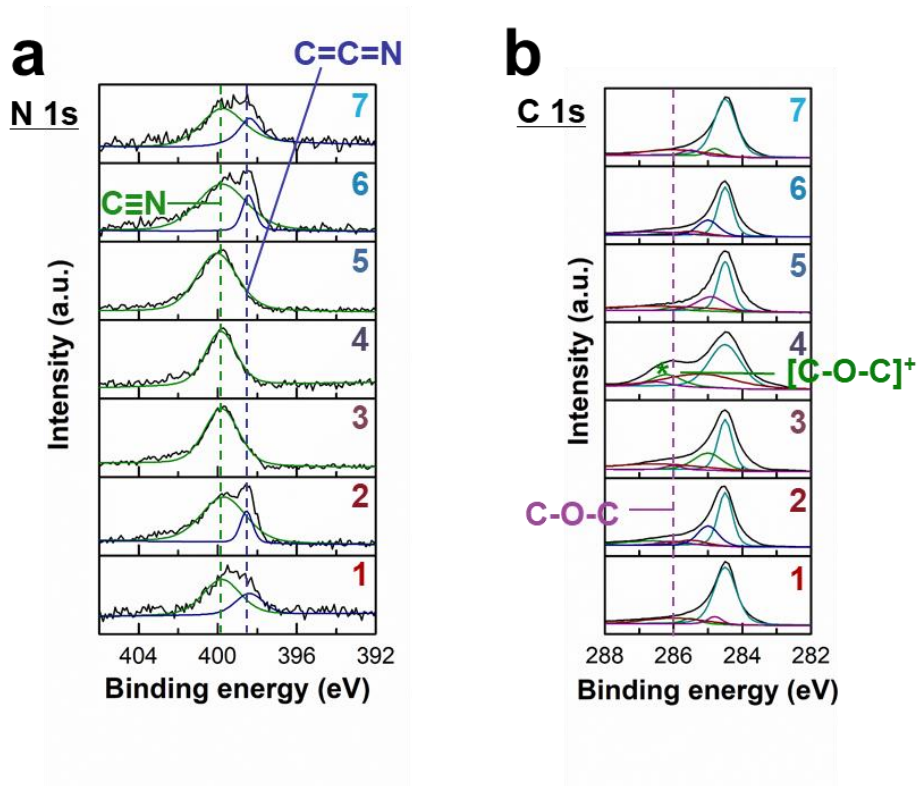


**Figure 3.26** *Ex situ* XPS data in the regions of (a) 406–392 eV and (b) 288–282 eV. The numbered labels are the same as those in Figure 3.24.

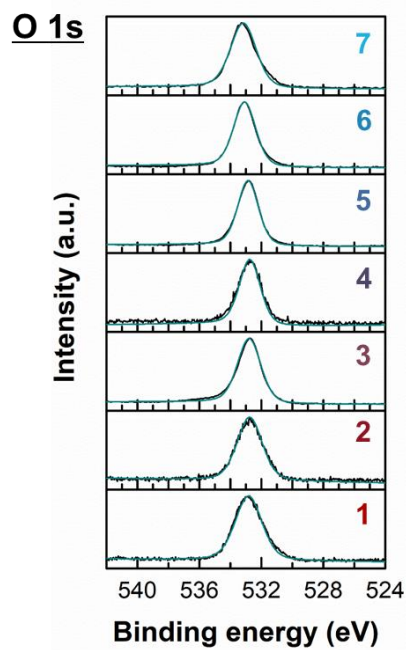


**Figure 3.27** *Ex situ* XPS data for DD-TCNQ. O 1s spectra of DD-TCNQ during the first cycle. The numbered labels are the same as those in Figure 3.24.

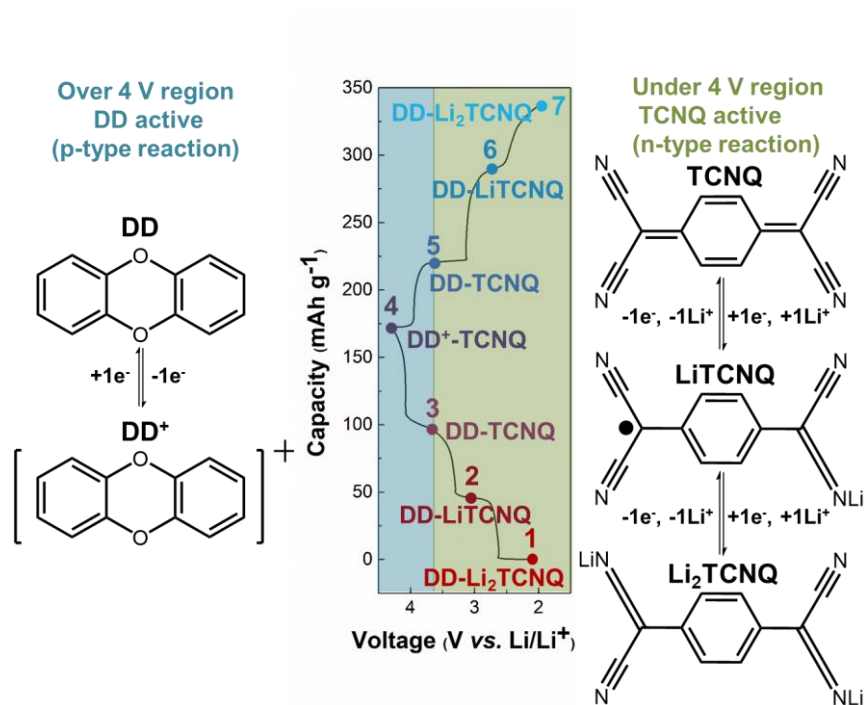


**Figure 3.28** Suggested redox mechanism of DD–TCNQ. The numbered labels are the same as those in Figure 3.24.

### 3.4 Concluding remarks

In summary, we designed a 4.0 V-class organic electrode material, DD, by rationally modifying redox center atoms to the Group 16 element having high electronegativity, and further demonstrated the development of a new OCTC with the high energy density. DD undergoes the stable *p*-type redox reaction mainly on the oxygen redox-center atom and its redox potential is the comparable level to the currently-used transition metal oxide-based electrode materials. It shows the highest redox potential (4.10 V vs. Li/Li<sup>+</sup>) among reported organics with the discharge capacity of 90 mAh g<sup>-1</sup>. In addition, DD showed the great rate performance at an even high current rate of 1000 mA g<sup>-1</sup>. Fabrication of the new OCTC with the developed DD and TCNQ was successfully performed, and its electrical conductivity and structural integrity could be greatly enhanced. In particular, the electrical conductivity of the suggested DD–TCNQ OCTC exhibit remarkable high value among organic electrode materials reported to date and is comparable to that of the highest level of transition metal oxide-based electrode materials. DD–TCNQ OCTC also showed the slight amount of electron transfer in the charge-transfer interaction as previously suggested PNZ–TCNQ OCTC, expecting to preserve their own redox capabilities of donor and acceptor molecules, even after constructing the OCTC. As a result, the achievement of a large energy density by combining two redox moieties in the OCTC can lead to a large practical energy density, ~560 Wh kg<sup>-1</sup> corresponding to 82% of the theoretical value, for the DD–TCNQ electrode. (when paired with Li metal and considering only the mass of the working electrode)

Designing new organic redox-active moieties with the improved performances can enlarge the material pool of the novel material group, OCTC, to ultimately optimize the battery performances. This approach would enhance the specified material properties, which is adequate to the certain application, and it finally suggests the great promise for the commercialization of OCTCs.

### 3.5 References

- [1] B. Dunn, H. Kamath, J.-M. Tarascon, *Science* **2011**, 334, 928.
- [2] D. Larcher, J. M. Tarascon, *Nature Chemistry* **2015**, 7, 19.
- [3] J. M. Tarascon, E. Wang, F. K. Shokoohi, W. R. McKinnon, S. Colson, *Journal of The Electrochemical Society* **1991**, 138, 2859.
- [4] A. K. Padhi, K. S. Nanjundaswamy, J. B. Goodenough, *Journal of The Electrochemical Society* **1997**, 144, 1188.
- [5] K. Mizushima, P. C. Jones, P. J. Wiseman, J. B. Goodenough, *Materials Research Bulletin* **1980**, 15, 783.
- [6] J. M. Tarascon, M. Armand, *Nature* **2001**, 414, 359.
- [7] Y. Liang, Z. Tao, J. Chen, *Advanced Energy Materials* **2012**, 2, 742.
- [8] S. Lee, G. Kwon, K. Ku, K. Yoon, S.-K. Jung, H.-D. Lim, K. Kang, *Advanced Materials* **2018**, 30, 1704682.
- [9] Z. Song, H. Zhou, *Energy & Environmental Science* **2013**, 6, 2280.
- [10] S. Lee, J. Hong, S.-K. Jung, K. Ku, G. Kwon, W. M. Seong, H. Kim, G. Yoon, I. Kang, K. Hong, H. W. Jang, K. Kang, *Energy Storage Materials* **2019**, 20, 462.
- [11] J. Lu, Z. Chen, F. Pan, Y. Cui, K. Amine, *Electrochemical Energy Reviews* **2018**, 1, 35.
- [12] Y.-Y. Hu, Z. Liu, K.-W. Nam, O. J. Borkiewicz, J. Cheng, X. Hua, M. T. Dunstan, X. Yu, K. M. Wiaderek, L.-S. Du, K. W. Chapman, P. J. Chupas, X.-Q. Yang, C. P. Grey, *Nature Materials* **2013**, 12, 1130.

- [13] S. Wang, L. Wang, Z. Zhu, Z. Hu, Q. Zhao, J. Chen, *Angewandte Chemie International Edition* **2014**, 53, 5892.
- [14] Y. Liang, P. Zhang, J. Chen, *Chemical Science* **2013**, 4, 1330.
- [15] H. Kim, J. E. Kwon, B. Lee, J. Hong, M. Lee, S. Y. Park, K. Kang, *Chemistry of Materials* **2015**, 27, 7258.
- [16] Y. Liang, P. Zhang, S. Yang, Z. Tao, J. Chen, *Advanced Energy Materials* **2013**, 3, 600.
- [17] S. Rothermel, P. Meister, G. Schmuelling, O. Fromm, H.-W. Meyer, S. Nowak, M. Winter, T. Placke, *Energy & Environmental Science* **2014**, 7, 3412.
- [18] T. Janoschka, M. D. Hager, U. S. Schubert, *Advanced Materials* **2012**, 24, 6397.
- [19] I. Goldberk, U. Shmueli, *Acta Crystallographica* **1973**, B29.
- [20] M. Lee, J. Hong, B. Lee, K. Ku, S. Lee, C. B. Park, K. Kang, *Green Chemistry* **2017**, 19, 2980.
- [21] T. B. Schon, B. T. McAllister, P.-F. Li, D. S. Seferos, *Chemical Society Reviews* **2016**, 45, 6345.
- [22] A. Wild, M. Strumpf, B. Häupler, M. D. Hager, U. S. Schubert, *Advanced Energy Materials* **2017**, 7, 1601415.
- [23] K. Oyaizu, H. Nishide, *Advanced Materials* **2009**, 21, 2339.
- [24] Y. Hanyu, I. Honma, *Scientific Reports* **2012**, 2, 453.



- [25] M. Lee, J. Hong, D.-H. Seo, D. H. Nam, K. T. Nam, K. Kang, C. B. Park, *Angewandte Chemie International Edition* **2013**, 52, 8322.
- [26] B. Scrosati, J. Garche, *Journal of Power Sources* **2010**, 195, 2419.
- [27] D. Tang, L. Ben, Y. Sun, B. Chen, Z. Yang, L. Gu, X. Huang, *Journal of Materials Chemistry A* **2014**, 2, 14519.
- [28] P. Periasamy, N. Kalaiselvi, H. S. Kim, *International Journal of Electrochemical Science* **2007**, 2, 689.
- [29] J.-L. Shi, D.-D. Xiao, M. Ge, X. Yu, Y. Chu, X. Huang, X.-D. Zhang, Y.-X. Yin, X.-Q. Yang, Y.-G. Guo, L. Gu, L.-J. Wan, *Advanced Materials* **2018**, 30, 1705575.
- [30] B. Huang, X. Li, Z. Wang, H. Guo, X. Xiong, *Ceramics International* **2014**, 40, 13223.
- [31] T. K. Eriksen, B. K. V. Hansen, J. Spanget-Larsen, *Polish Journal of Chemistry* **2008**, 82.
- [32] T.-T. Fang, H.-Y. Chung, *Journal of the American Ceramic Society* **2008**, 91, 342.
- [33] R. Guo, P. Shi, X. Cheng, Y. Ma, Z. Tan, *Journal of Power Sources* **2009**, 189, 2.

## **Chapter 4. Elucidating the energy storage mechanism of charge-transfer complex according to the interplay with electrolytes**

### **4.1 Research background**

The development of the post lithium-ion batteries (post LIBs) has been highly demanded in these days due to the limited resources of transition metals, the limited energy density and material candidates.<sup>[1-3]</sup> As an alternative to the currently used rechargeable batteries, organic rechargeable batteries, which use organics as the electrode material, are one of the highly promising candidates for the next-generation energy storage system since they are transition metal-free system.<sup>[4-7]</sup> Organic redox-active compounds can be made of earth-abundant resources such as carbon, oxygen, and nitrogen, thus they are potentially lighter than the transition metal-based electrode materials, expecting to exhibit the higher energy density. Furthermore, the distinctively powerful advantage of the organic electrode materials is chemical tunability. Organic synthesis does not require the extreme condition of high temperature and pressure. They are also usually constructed based on carbon network, which can have the largest structural diversity. These characteristics enable the organic redox-active molecules to possess a huge pool of the electrode material candidates.

Exploiting the various types of organic electrode materials have been actively progressed, however, the electrochemical performances could not reach the current level of the inorganic-based electrode materials.<sup>[6-7]</sup> They are impeded by own limitations from their intrinsic material properties of low electrical conductivity and high solubility to solvent. Numerous approaches to overcome the above-mentioned issues have been suggested, and the reported strategies can be categorized in the molecular-level and electrode-level tuning. First, the researchers tried to chemically tune the redox-active molecules with adding functional groups that can enhance the electrochemical performances,<sup>[8-11]</sup> however, the attached functional groups are redox-inactive, inducing the decrease of energy density. Recently, the concept of covalent organic framework (COF) has been suggested to tune the molecular architecture that has a porous structure and the connection of two or more organic molecules influence the decrease of solubility.<sup>[12-14]</sup> Nevertheless, all the suggested solutions in the molecular level tuning require the addition of redox-inactive parts, resulting in the decrease of energy density. On the other hand, the hybridization with the conductive scaffolds such as graphene and carbon nanotubes were considered to solve the intrinsic limitations simultaneously.<sup>[15-17]</sup> However, electrode level tuning also contains the addition of redox-inactive part, resulting in increase of the total mass of the electrode. Thus, to surmount the trade-off relationship of the reported strategies, it is required to develop the novel approach without utilizing the redox-inactive additives.

In the prior study, we reported the novel material group, organic charge-transfer complexes (OCTCs), as the solution for enhancing the intrinsic material properties with the combination of two different redox-active molecules.<sup>[18]</sup> We successfully increased the electrical conductivity and decreased the solubility to solvents through only the molecular rearrangement. As a result, the developed OCTC, combination of phenazine (PNZ) and 7,7,8,8-tetracyanoquinodimethane (TCNQ), exhibited the high rate capability compared to those of constituting monomers, as well as the improved cycle stability from the reduced stability. However, the donor component of PNZ molecule could not realize its redox activity in the firstly applied model battery system (Li-TEGDME electrolyte), resulting in the limited energy density.

Unlike the inorganic electrodes, the redox mechanism of organic electrode materials is currently suggested that it is affected from the sorts of electrolytes regarding the charge carrying ions and solvent molecules.<sup>[19-24]</sup> It is speculated to have the physical and chemical interaction between the active material and the electrolytes. Organic redox-active compounds binding with the charge carrying ions have the different charge states according to the types of charge carrying ions, which has a possibility to exhibit the different solubility or reactivity compared to the neutral state.<sup>[27-29]</sup> On the other hand, solvent type dominantly influences the solubility of the organic molecules and it also has a chemical stability issue that can affect the redox reaction.<sup>[9, 30]</sup>

Herein, we elucidated the energy storage behavior of organic electrode material, here for PNZ–TCNQ OCTC, regarding the interplay with electrolytes through varying the electrolyte types. Notably, it is revealed that the electrolyte-participating chemical change of the active material just after the electrolyte exposure plays a key role to the structural degradation and the limited redox-activity. As a result, PNZ–TCNQ OCTC in the most compatible Zn-aqueous electrolyte, which does not have any chemical side reaction with the active material, could utilize the full redox activity of both donor and acceptor with enhanced rate performance and cycle stability. In the following, we also provided the quantitative and qualitative analysis of the dissolution phenomenon and suggested the final solution to ultimately maximize the long-term stability.

## **4.2 Experimental methods**

### **4.2.1 Preparation of materials**

PNZ was purchased from Alfa Aesar (USA) and TCNQ, LiTFSI, and  $\text{Zn(TFSI)}_2$  was purchased from Sigma-Aldrich (UK). All the commercially available chemicals were utilized without further purification. PNZ–TCNQ OCTC was synthesized following a procedure previously described in the literature.<sup>[31]</sup> The PNZ and TCNQ powders were mixed in an equimolar ratio in acetone solvent for 3 h at room temperature. The resulting solution was filtered, and the residue was dried at 30 °C overnight.

### **4.2.2 Electrochemical measurements**

Capacity–voltage profiles of the PNZ–TCNQ OCTC and its constituting molecules versus a Li metal foil (Hohsen, Japan) and a Zn metal (Alfa Aesar, USA) in coin-type cells (CR2032) were obtained. The Li and Zn metal anode were prepared in an Ar-filled glove box. The cathodes were fabricated by mixing 40% w/w active materials, 40% w/w carbon black (Super P), and 20% w/w polytetrafluoroethylene (PTFE, Aldrich) binder. Especially for the high-content test, cathodes with additional compositions were formulated by mixing 60% w/w active materials, 35% w/w carbon black, and 5% w/w polyvinylidene fluoride (PVdF) binder and 65% w/w active materials 30% w/w carbon black, and 5% w/w PVdF binder and 70% w/w active materials, 20% w/w carbon black, and 10% w/w PVdF

binder and 80% w/w active materials, 15% w/w carbon black, and 5% w/w PVdF binder and 90% w/w active materials, 5% carbon black, and 5% w/w PVdF binder and 95% w/w active materials, 2.5% w/w carbon black, and 2.5% w/w PVdF binder. A porous glass microfiber membrane (GF/F; Whatman, UK) and a microporous membrane (Celgard 3560) were used as a separator in the non-aqueous cells and aqueous cells, respectively. The electrolytes were 1M LiTFSI in EC/DMC, TEGDME, H<sub>2</sub>O, EC/PC, PC, DEGDME, DME, DMSO, DOL/DME, ACN, and 1M Zn(TFSI)<sub>2</sub> in H<sub>2</sub>O, TEGDME, PC, and DMSO, and the cells were assembled in an inert atmosphere within an Ar-filled glove box. The electrochemical measurements were performed using a battery test system (Won-A Tech, Korea).

#### **4.2.3 *Ex situ* electrode characterization**

The electrodes of PNZ–TCNQ and its constituting molecules at different states of cycling were prepared by disassembling coin cells followed by the rinsing the electrodes with the used solvents in the electrolytes. XRD profiles were obtained using the D2 PHASER with Cu-K $\alpha$  radiation ( $\lambda = 1.54178 \text{ \AA}$ ) at a scanning speed of  $0.2^\circ \text{ min}^{-1}$  in the  $2\theta$  range of  $5^\circ$ – $60^\circ$ . TG curves were obtained using the Discovery TGA (TA instruments, USA) at an elevating speed of  $10^\circ \text{ C min}^{-1}$  in the temperature range from the room temperature to the  $600^\circ \text{ C}$ . FTIR spectra were measured using pellets made of the electrodes at different states and KBr powder on an FT/IR-4200 (Jasco, Japan) at a resolution of  $4 \text{ cm}^{-1}$ . UV–vis spectra measurements were performed using an JASCO-3000 (Jasco, Japan) at a resolution of 10 nm.

## 4.3 Results and discussions

### 4.3.1 Diverse redox reaction pathways according to the electrolyte types

First, the electrochemical test of PNZ–TCNQ OCTC was performed with the numerous types of electrolytes as illustrated in Figure 4.1, and it was observed that all the trend of the capacity–voltage profiles is different according to the electrolyte types. Priorly reported PNZ–TCNQ OCTC was applied as a cathode in the Li non-aqueous battery with the 1M LiTFSI (lithium bis(trifluoromethanesulfonyl) imide) in TEGDME (tetraethylene glycol dimethylether). Electrochemical test was firstly performed in the mostly used electrolytes of 1M LiTFSI in EC (ethylene carbonate)/DMC (dimethyl carbonate) (v/v=1:1), and the totally different shape of the capacity–voltage profiles was obtained. PNZ–TCNQ OCTC with 1M LiTFSI in EC/DMC showed the two distinct voltage plateaus in both the discharging and charging processes, while the three steps of voltage plateaus were observed in 1M LiTFSI in TEGDME. (Figure 4.2) Other representative types of solvents were further applied as an electrolyte to electrochemically test the redox reaction pathways of PNZ–TCNQ OCTC, as shown in Figure 4.3. Some of the solvents such as DMSO (dimethyl sulfoxide), DOL (1,3-dioxolane)/DME (dimethyl ether), and Acetonitrile (ACN) could not realize the reversible redox reaction, however, the solvents with ether and carbonates functional groups showed the reversible redox behaviors except for the DME-used electrolyte. DEGDME-used electrolyte showed the same redox steps during cycling as the



TEGDME-used electrolyte, while PNZ–TCNQ OCTC electrode in DME-used electrolyte exhibited the irreversible charge profile, may induced by the shuttling effect from the high solubility of the charged species.<sup>[32-33]</sup> EC/PC (propylene carbonate) (v/v=1:1) and PC-used electrolytes showed the two distinct voltage plateaus in both the discharging and charging processes as EC/DMC-used electrolyte. It can be speculated that the solvents with the same functional groups undergo the same redox chemistry. Furthermore, water is also one of the solvent candidates used in the electrolyte of rechargeable batteries, and it has a hydroxyl group different from the ether and carbonates functional groups. Li-aqueous electrolyte showed the reversible redox reaction with the single voltage plateau. (Figure 4.4) On the other hand, in order to investigate the effect of the valency of the charge carrying ion, a divalent zinc ion ( $\text{Zn}^{2+}$ ) was also electrochemically tested as a charge carrying ion in the various types of solvents, as presented in Figure 4.5. All the non-aqueous solvents (PC, TEGDME, and DMSO) with the zinc ion exhibited the irreversible redox reaction, however, reversible charge/discharge reaction was observed in Zn aqueous electrolyte. It showed the totally different reaction steps compared to those in monovalent lithium ion electrolytes, exhibiting the four-step discharge and three-step charge processes.

As a result, four representative types of capacity-voltage profiles, which show the reversible redox reaction, can be categorized among the utilized electrolytes, as shown in Figure 4.6. The dotted line expressed in the capacity-voltage profiles of Li-aqueous and Zn-aqueous electrolytes was obtained under the

same voltage cutoff (2.2-3.8 V vs. Li/Li<sup>+</sup>) without considering the hydrolysis, thus the electrochemical test of the PNZ–TCNQ OCTC electrodes in aqueous batteries were performed under the narrower voltage region that can be stable against the water splitting. Li-carbonates electrolyte exhibited the two-step redox pairs at 3.18/3.30 and 2.60/2.76 V vs. Li/Li<sup>+</sup>, for the reduction and oxidation, respectively. The discharge and charge voltage plateaus of Li-ethers electrolyte are located at the 3.27/3.05/2.83 V and 3.42/3.30/2.96 V vs. Li/Li<sup>+</sup>, respectively, while those of Li-aqueous electrolyte are positioned on the 3.22 V and 3.33 V vs. Li/Li<sup>+</sup> (-0.18 V and -0.07 V vs. LiFePO<sub>4</sub>/FePO<sub>4</sub>), respectively. Besides, the PNZ–TCNQ OCTC electrode in Zn-aqueous electrolyte showed the unpaired numbers of the redox steps during the discharging and charging processes. It exhibited the four-step discharge voltages of 2.86/2.92/3.13/3.29 V and three-step charge voltages of 3.10/3.21/3.53 V vs. Li/Li<sup>+</sup> (0.56/0.62/0.83/0.99 V and 0.80/0.91/1.23 V vs. Zn/Zn<sup>2+</sup>), respectively. It is noticed that the PNZ–TCNQ OCTC participates in different redox reactions from all the obtained capacity-voltage profiles. Suggested redox mechanism in Figure 4.6c follows the prior study<sup>[18]</sup> that only TCNQ in the PNZ–TCNQ OCTC is redox-active, and the operating voltage region of TCNQ is known to be located above that of PNZ. It was available to activate the only acceptor molecule, TCNQ, of PNZ–TCNQ OCTC in the priorly reported battery system (Li-ether electrolyte),<sup>[18]</sup> and the other Li-based electrolytes (Li-carbonates and Li-aqueous electrolytes) also exhibited the two-electron redox reaction derived from the TCNQ redox. However, surprisingly, PNZ–TCNQ OCTC are fully redox-activated in Zn-aqueous electrolyte

with undergoing the four-electron redox reaction successfully. This result implies the activation of the PNZ redox, which could not be realized in the Li-based electrolytes. The investigation on the electrochemical profiles indicates that the redox reaction pathways of organic redox-active compounds can be differed according to the types of solvents and charge carrying ions, and the several possible scenarios of this phenomenon can be suggested. First, the possibility of the spontaneous chemical reaction between PNZ–TCNQ OCTC and electrolytes can differ the redox reaction pathways. There are three cases in respect of chemical change; (1) the chemical interaction between PNZ–TCNQ OCTC and electrolytes before battery cycling, (2) no chemical change just after battery assembly, but the different intermediate products during discharging and charging processes due to the different reactivity in the intermediate states, and (3) participation of the electrolytes in the redox reaction of PNZ–TCNQ OCTC as a catalyst. On the other hand, physical change due to the molecular rearrangement can also be the origin of the different redox mechanism, and there are two possible cases in this prospect; (1) newly nucleated crystal structure after dissolution under the electrolyte exposure before battery cycling and (2) diverse structural evolution of the intermediate products during discharging and charging processes because of the different chemical environment (*e.g.* dielectric constant and solvation energy). The last hypothesis is the complex formation of PNZ–TCNQ OCTC and electrolytes. This case is hard to be classified as both chemical and physical change since complexation induce to alter both the chemical and physical parameters. As a result, in order to narrow down

the suggested hypothesis, it is required to conduct the phase analysis evolved in the intermediate states regarding the rested state (starting point with electrolyte exposure and without battery cycling) during discharging and charging processes.

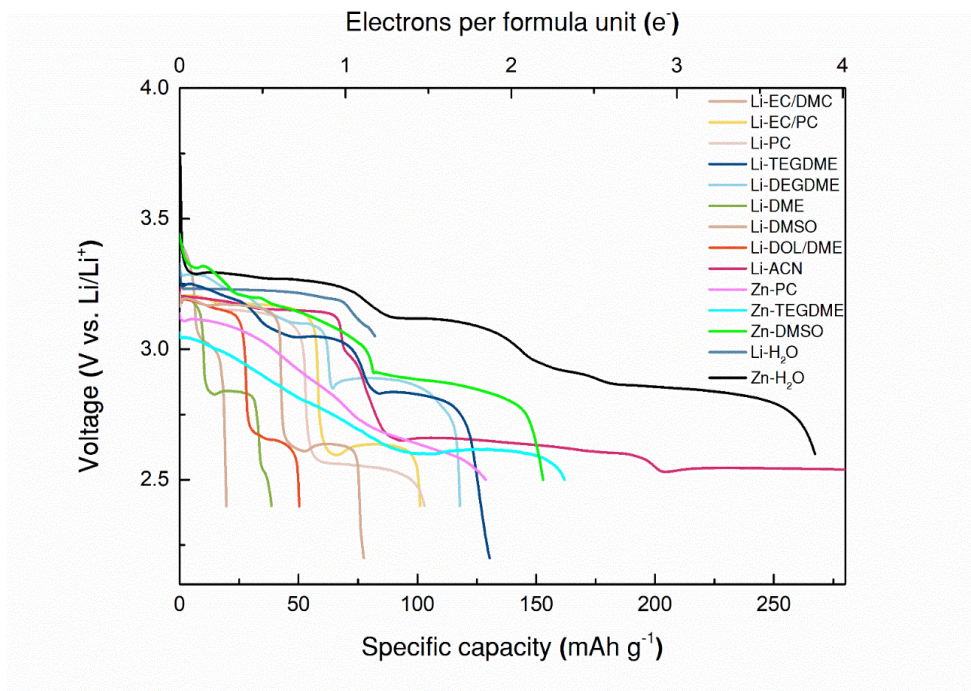


**Figure 4.1** Capacity–voltage profiles of PNZ–TCNQ in universal electrolytes during the discharging process.

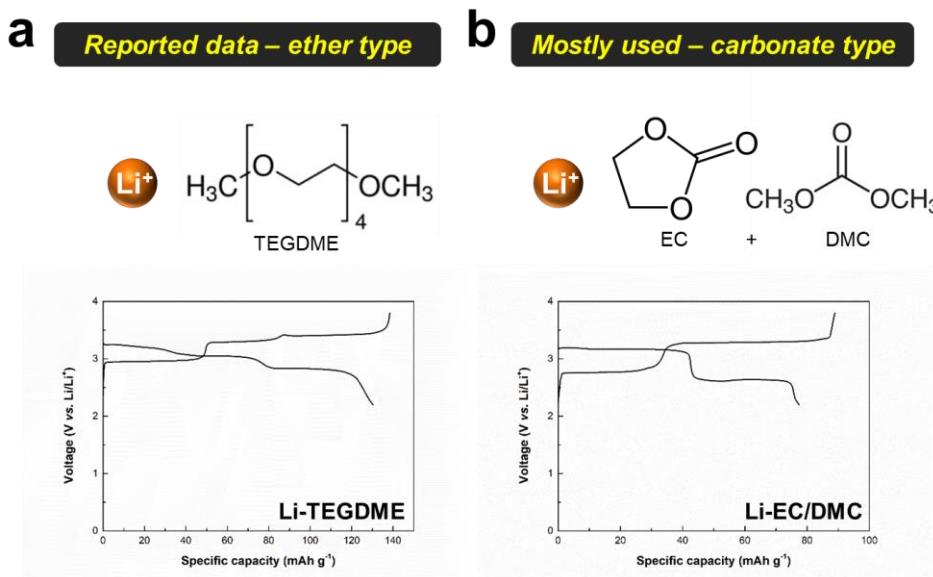


**Figure 4.2** Capacity–voltage profiles of PNZ–TCNQ OCTC electrode in the reported electrolyte (1M LiTFSI in TEGDME) and the mostly used electrolyte (1M LiTFSI in EC/DMC).

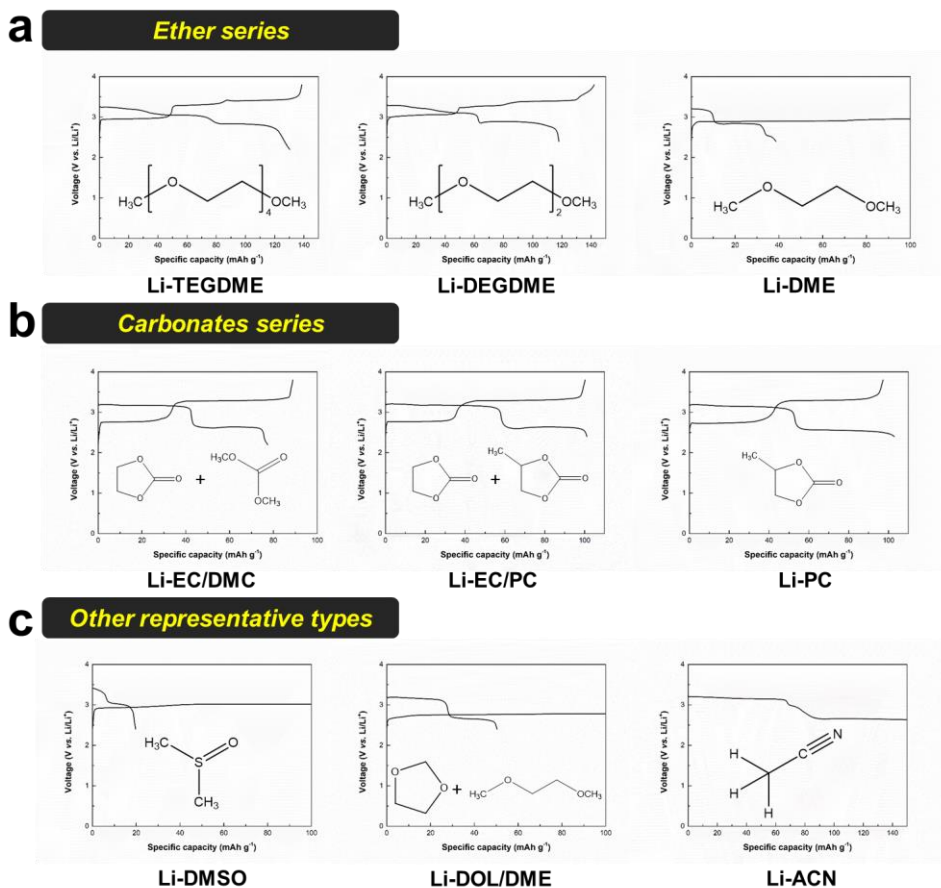


**Figure 4.3** Electrochemical tests of PNZ–TCNQ OCTC electrode in the diverse types of solvents for Li non-aqueous batteries. Capacity–voltage profiles of PNZ–TCNQ OCTC electrodes in 1M LiTFSI in (a) TEGDME, DEGDM, and DME, (b) EC/DMC, EC/PC, and PC, and (c) DMSO, DOL/DME, and ACN.

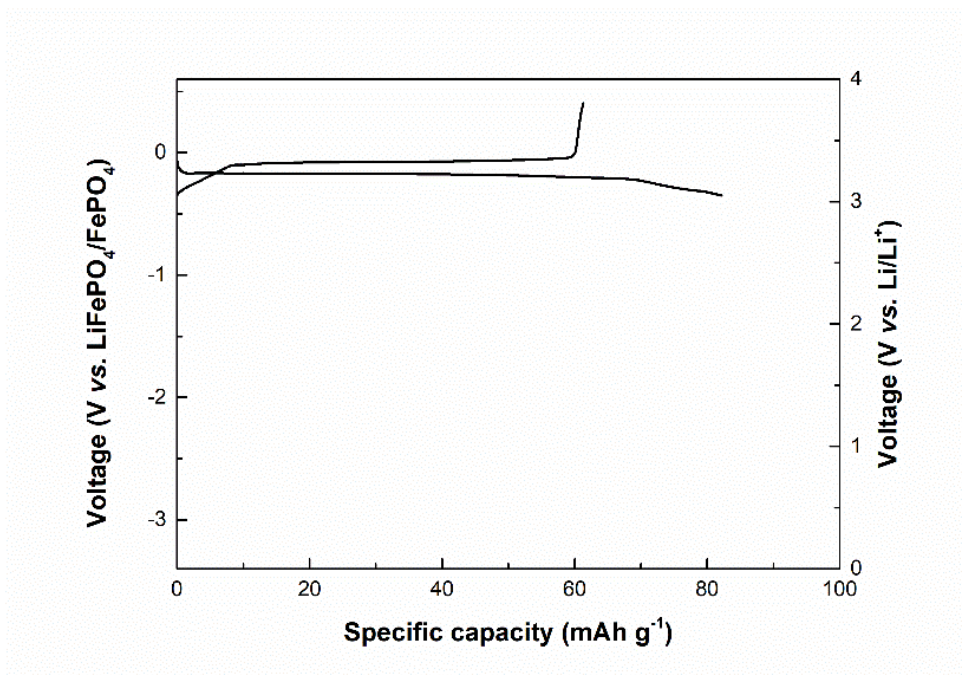


**Figure 4.4** Capacity–voltage profiles of PNZ–TCNQ OCTC electrode in Li-aqueous electrolyte.



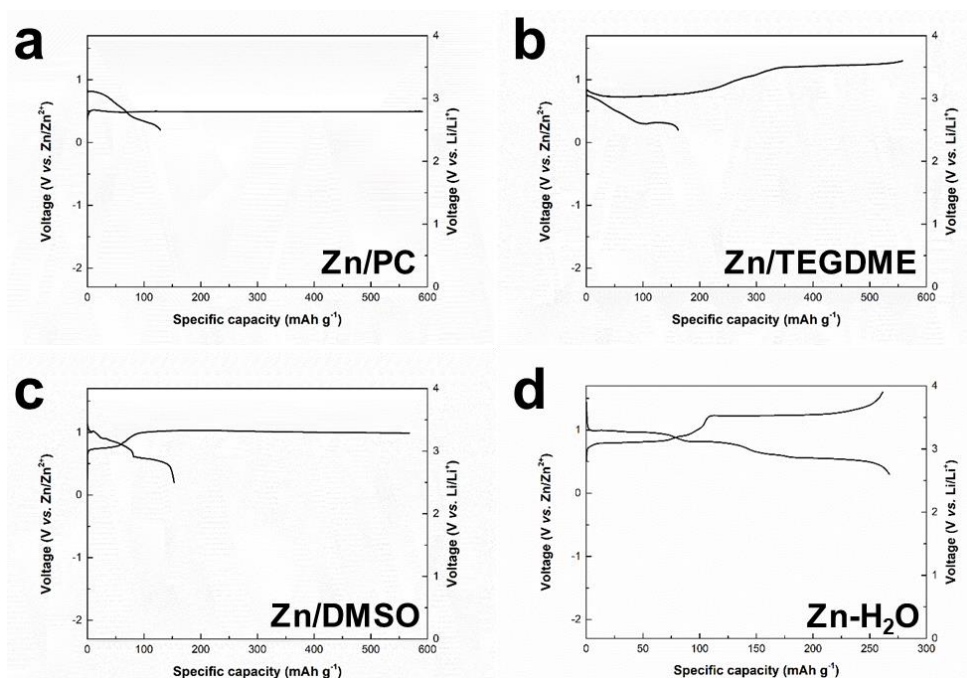


**Figure 4.5** Electrochemical tests of PNZ-TCNQ OCTC electrode in Zn ion batteries. Capacity-voltage profiles of PNZ-TCNQ OCTC electrode in 1M  $\text{Zn}(\text{TFSI})_2$  in (a) PC, (b) TEGDME, (c) DMSO, and (d)  $\text{H}_2\text{O}$ .

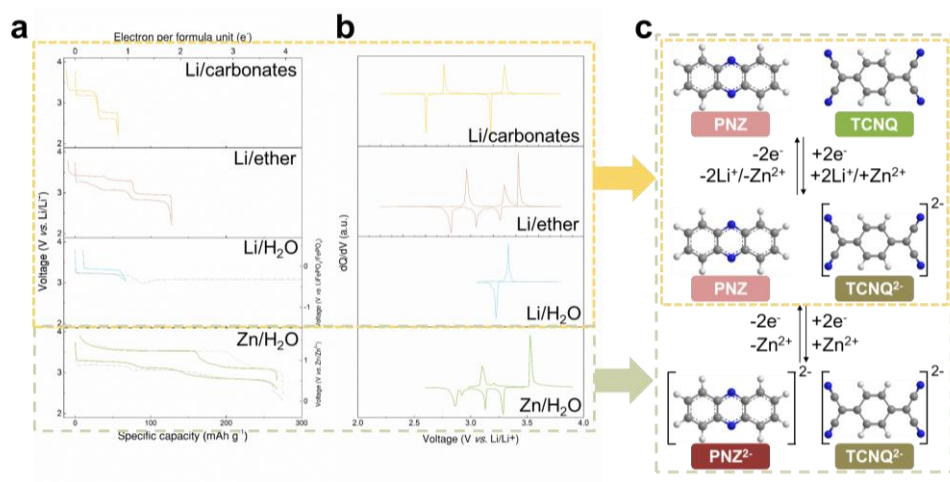


**Figure 4.6** Electrochemical behaviors of PNZ–TCNQ according to the electrolyte types and the four representative reaction types of PNZ–TCNQ. (a) Capacity–voltage profiles and (b) differential capacity curves of PNZ–TCNQ in Li ion with carbonates electrolytes, ether electrolytes, aqueous electrolytes, and Zn ion with aqueous electrolytes. (c) Suggested redox mechanism of PNZ–TCNQ regarding the four-electron storage.

### 4.3.2 Structural investigation on the intermediate phases of PNZ–TCNQ OCTC electrode during battery cycling

We further examined the structural changes in PNZ–TCNQ OCTC redox-active material during the battery cycling in the four representative electrolytes, through *ex situ* X-ray diffraction (XRD) analysis. We measured the XRD pattern of PNZ–TCNQ OCTC electrodes at the different state-of-charge during the first cycle of discharging and charging, obtained by recollecting the electrode samples from coin cells disassembled at each state. As presented in Figure 4.7, *ex situ* XRD patterns of PNZ–TCNQ OCTC electrodes in each electrolyte showed the reversible behavior after one battery cycle with recovering all the peak position, however, the peak intensity ratio was changed. Moreover, the obtained long-range arrangement of the intermediate phases of OCTC electrodes are totally distinct according to the electrolytes used, indicating that the PNZ–TCNQ OCTC have different redox mechanisms by means of the electrolyte types, as we expected in the analysis on electrochemical profiles. The most interesting point is that the peak patterns of the pristine samples were changed just after electrolyte exposure. (Figure 4.8a) Pristine electrode samples in each *ex situ* XRD pattern in Figure 4.7 are obtained through the cell disassembly without electrochemical cycling, namely, the pristine electrodes were stored in the batteries for the rest time of 12 h. (hereafter, called as rested samples) As shown in Figure 4.8b, all the rested samples except for the electrode in Li-aqueous electrolyte showed the same peak position with the pristine electrode, however, it was observed that the peak ratio of the material main peak at about 28°

are significantly different compared to the reference PTFE binder peak at  $18^\circ$  for the rested samples in Li-EC/DMC and Li-TEGDME electrolytes. On the other hand, rested sample in Li-aqueous electrolyte exhibited the fully different long-range arrangement compared to the pristine electrode, as illustrated in Figure 4.8c. Peak pattern of the rested sample in Li-aqueous electrolyte is expected to be the mixture of the PNZ and TCNQ monomers and the unindexed peaks. The data from the *ex situ* structural analysis implies that the PNZ–TCNQ OCTC undergoes the structural change, just after electrolyte exposure, that is, from the starting point of the battery assembly without cycling. Starting redox active materials already altered to the different structure according to the electrolyte types, thus, following intermediate products in the various electrolytes also shows different structural evolution during discharging and charging processes. However, it is hard to declare the origin of the structural change after electrolyte exposure until this step. Partial chemical degradation or complex formation can induce the distinct material main peak intensity ratio and the unindexed peaks, and the dissolution followed by the nucleation can also evolve the new crystal structure of PNZ–TCNQ OCTC. As a result, further analysis to identify the origin of the distinct redox reaction mechanism is demonstrated through thermo-gravimetric (TG) analysis.

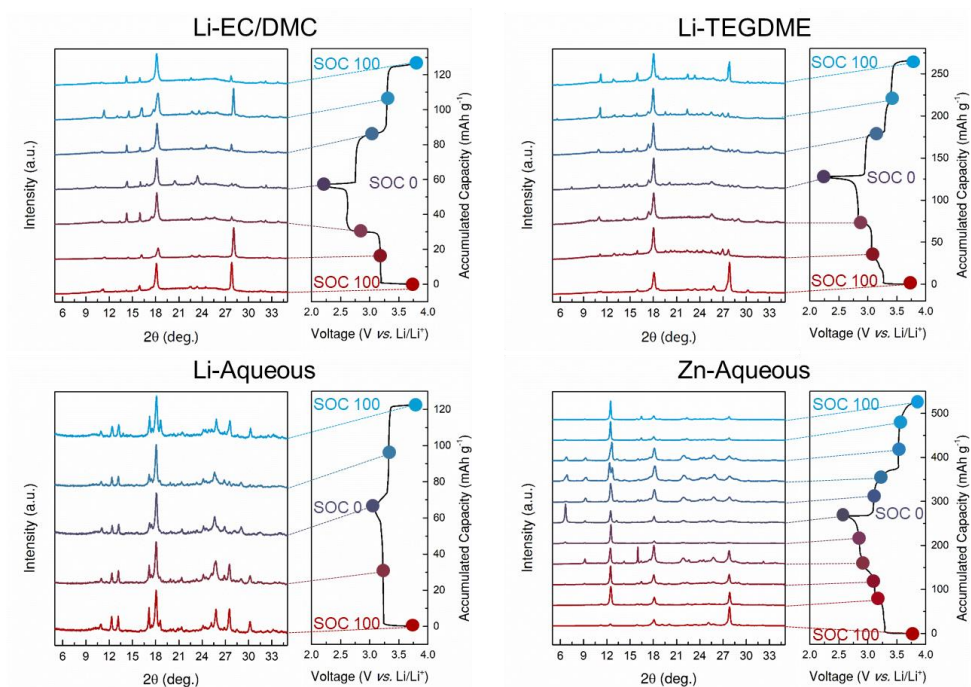


**Figure 4.7 Structural investigation on the intermediate phase of PNZ-TCNQ during cycling.** *Ex situ* XRD of PNZ-TCNQ during discharging and charging processes in (a) 1M LiTFSI in EC/DMC (v/v 1:1), (b) 1M LiTFSI in TEGDME, (c) 1M LiTFSI in  $\text{H}_2\text{O}$ , and (d) 1M  $\text{Zn}(\text{TFSI})_2$  in  $\text{H}_2\text{O}$ .

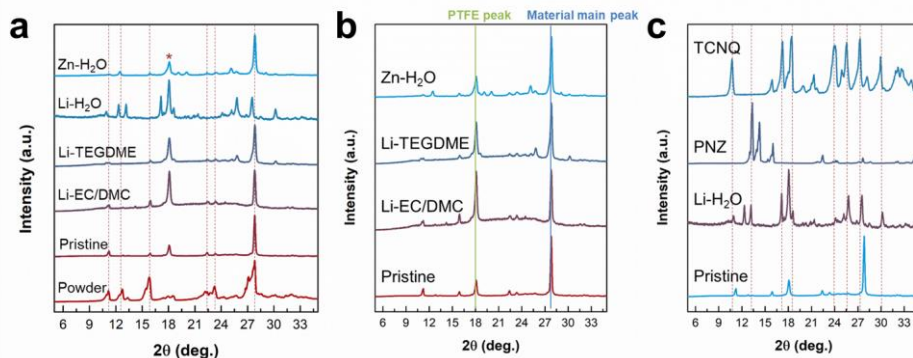


**Figure 4.8 Immediate phase transformation of PNZ–TCNQ OCTC electrode.**

(a) Long-range arrangements of PNZ–TCNQ powder, pristine, and electrodes after electrolytes exposure. (b) Comparison of the residual amount of PNZ–TCNQ of pristine and electrodes in 1M LiTFSI in EC/DMC, LiTFSI in TEGDME, and Zn(TFSI)<sub>2</sub> in H<sub>2</sub>O. (c) Structural destruction of PNZ–TCNQ electrode after the exposure to 1M LiTFSI in H<sub>2</sub>O.

### 4.3.3 Thermal and chemical investigation on the pre-formed product during battery cycling

TG analysis was conducted to identify the origin of structural change from the unexpected reaction, that is deduced from the altered peak patterns of the rested samples in XRD analysis. Original TG curves and the correlated derivative function curves are plotted in Figure 4.9. Original PNZ–TCNQ OCTC powder showed the two-step weight drop at  $\sim 200$  °C and  $\sim 280$  °C, each correlated to the PNZ and TCNQ evaporation, respectively. PNZ–TCNQ OCTC pristine electrode also exhibited the two-step weight drop at  $\sim 185$  °C and  $\sim 273$  °C, and one more weight drop at  $\sim 545$  °C was observed, which is the PTFE binder evaporation. However, rested samples except for the case of Zn-aqueous electrolyte showed the different trend of weight drop compared to the pristine electrode. The first weight drop, which is originally correlated to the PNZ evaporation, is shifted to the lower temperature of  $\sim 120$  °C and  $\sim 155$  °C for the rested samples in Li-EC/DMC and Li-TEGDME electrolytes, respectively, and the unexpected weight drop at  $\sim 450$  °C was observed for the rested samples in Li-EC/DMC, Li-TEGDME, and Li-aqueous electrolytes. The newly formed weight drop at  $\sim 450$  °C for the rested sample in Li-aqueous electrolyte is expected as the unwanted side-product from just after electrolyte exposure, which was observed in the newly evolved peak pattern of the rested sample in Li aqueous electrolyte. In the *ex situ* XRD analysis, the rested samples in Li-EC/DMC and Li-TEGDME exhibited the same peak position with the pristine sample, however, they also have the weight drop at  $\sim 450$  °C as the Li aqueous electrolytes, as well as the

large shift of the first weight drop to the lower temperature. It can be speculated that the peak ratio difference of the material main peak to the reference binder peak in Li-EC/DMC and Li-TEGDME is originated from this unexpectedly formed side-products. In other words, PNZ–TCNQ OCTC undergoes the chemical change by partial chemical degradation or complex formation, not a physical change from the nucleation. exposure. Nevertheless, the rested sample in Zn-aqueous electrolyte exhibited the highly similar three-step weight drops as the pristine electrode.

On the other hand, the electrode was fabricated with mixing the active material, conducting agent (conductive carbon), and binder (w/w/w=4:4:2). It should result in the residual weight of the pristine electrode as 40%, which is from the residual conductive carbon in the electrode. However, the residual weights of the rested samples except for Zn-aqueous electrolyte also shows the much lower value compared to the pristine sample, as illustrated in Figure 4.10. This indicates that the relative portion of the conducting agent in the electrode decreased, that is, the insertion of another component into the electrode. The only possible candidate that can be inserted into the electrode is the electrolyte for the rested samples, implying that the unwanted products are originated from the electrolyte participation. Nevertheless, the rested sample in Zn-aqueous electrolyte only showed the slight increase of the residual weight, which means that there is no electrolyte interaction with the active material, but it may be due to the slight amount of the active material dissolution.



PNZ–TCNQ OCTC powders, which were immersed in various types of pure solvents, were scrutinized through the TG analysis to further identify specifically the origin of pre-formed product, as presented in Figure 4.11. Dried PNZ–TCNQ OCTC powders, which were in methanol (MeOH), ACN, acetone, dichloromethane ( $\text{CH}_2\text{Cl}_2$ ), chloroform ( $\text{CHCl}_3$ ), and water solvents, showed the two-step weight drop as the pure PNZ–TCNQ OCTC powder, indicating no side reaction with the utilized solvents in this case. However, other samples that were stored in EC/DMC and TEGDME solvents exhibited the one big weight drop below 200 °C followed by the other small weight drop. The weight drop below 200 °C was also observed for the rested samples in the case of Li-EC/DMC and Li-TEGDME (Figure 4.9). Therefore, it can be expected that this shifted weight drop to the lower temperature is originated from the solvent-derived side-product formation. Interestingly, water solvent does not induce the side reaction with PNZ–TCNQ OCTC, while rested sample in Li-aqueous electrolyte showed the unexpected weight drop at ~450 °C. Accordingly, it is speculated that the weight drop presented at ~450 °C corresponds to the salt-derived side-product formation. Same experiment was demonstrated with the TCNQ powder, and this gives a clue that the main component of the side-reaction is TCNQ molecules in PNZ–TCNQ OCTC. (Figure 4.12) Dried TCNQ powders, which were immersed in MeOH, ACN, acetone,  $\text{CH}_2\text{Cl}_2$ ,  $\text{CHCl}_3$ , and water solvents, showed the clear single weight drop without any side reaction. However, same change of the TG curve shape was observed for the samples stored in EC/DMC and TEGDME solvents.

From the structural and thermal analysis on this phenomenon, it can be stated that the PNZ–TCNQ OCTC chemically interacts with the electrolyte without battery cycling, and the TCNQ molecules in OCTC mainly participate in the chemical interaction. This side reaction affects the distinct structural evolution during battery cycling, further inducing the difference of the redox reaction pathways. It is hard to declare whether the exact side reaction is the chemical degradation or complex formation, however, the probability of the complexation theory seems higher compared to the hypothesis on chemical degradation. The possibility of the complex formation of the TCNQ molecule and electrolytes had been reported in numerous literatures.<sup>[34-36]</sup> It is well-observed that the TG curve shape of the TCNQ(solvent) or (Li)(TCNQ)(solvent) complex altered from the single weight drop in the TG curve of the TCNQ molecule.<sup>[34-35]</sup> Furthermore, as shown in Figure 4.13, change of the chemical environment of the PNZ–TCNQ OCTC powder after electrolyte exposure was further examined through the FTIR spectroscopy (Fourier-transform infrared spectroscopy) to support the statement of the complexation between the organic active material and electrolytes. Broad band at around  $3500\text{ cm}^{-1}$  correlates to the intermolecular interaction of the solvation effect,<sup>[37-38]</sup> indicating the participation of the solvents to the PNZ–TCNQ OCTC. Additionally, the fingerprint peak of TCNQ at  $2220\text{ cm}^{-1}$ ,<sup>[39]</sup> corresponding to the nitrile bond stretching, remains constant though some of the samples have the interaction with the electrolytes.

As a result, it can be noted that there is a further room to exactly define the side reaction inducing structural changes of PNZ–TCNQ OCTC. From the obtained data until this step, it can only be declared that the different redox reaction mechanism of PNZ–TCNQ OCTC is originated from the chemical interaction between TCNQ and the utilized electrolytes (Li-EC/DMC, Li-TEGDME, and Li-H<sub>2</sub>O electrolytes).

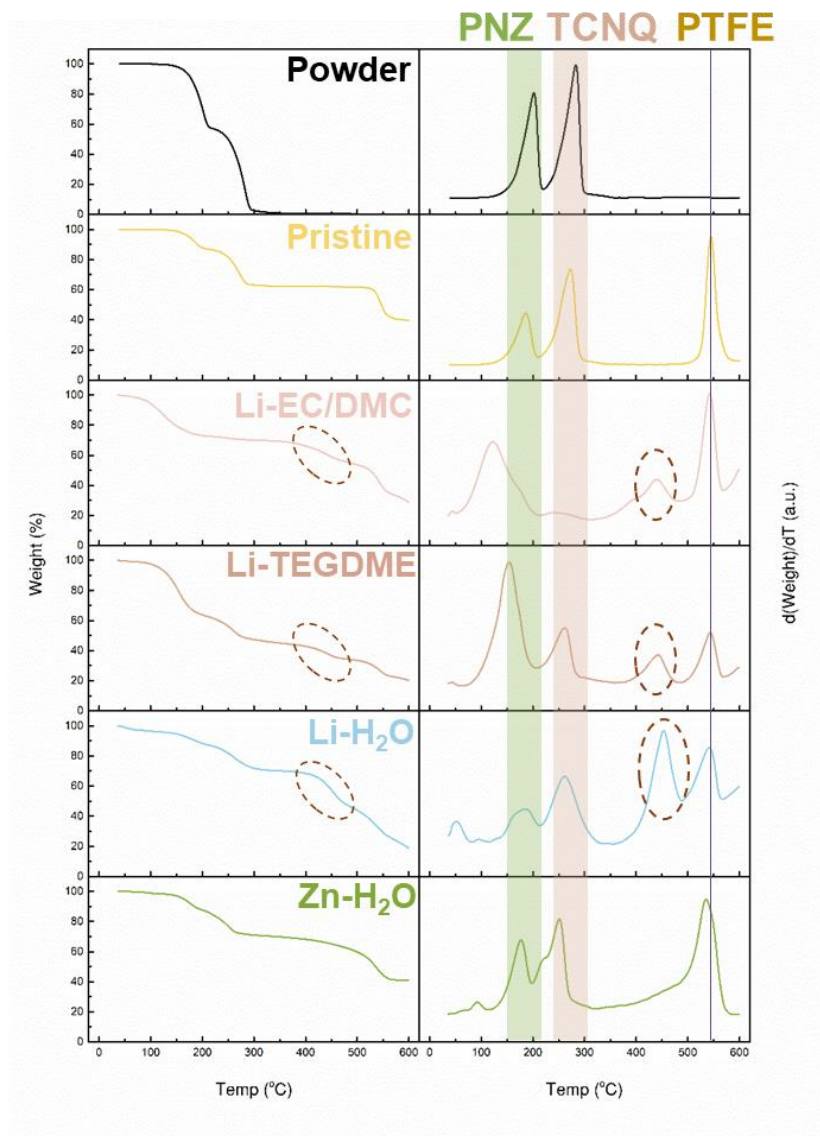


**Figure 4.9** Thermo-gravimetric (TG) curves (left) and correlated TG derivative curves (right) of PNZ–TCNQ powder, pristine, and electrodes obtained from the cell disassembly without battery cycling.

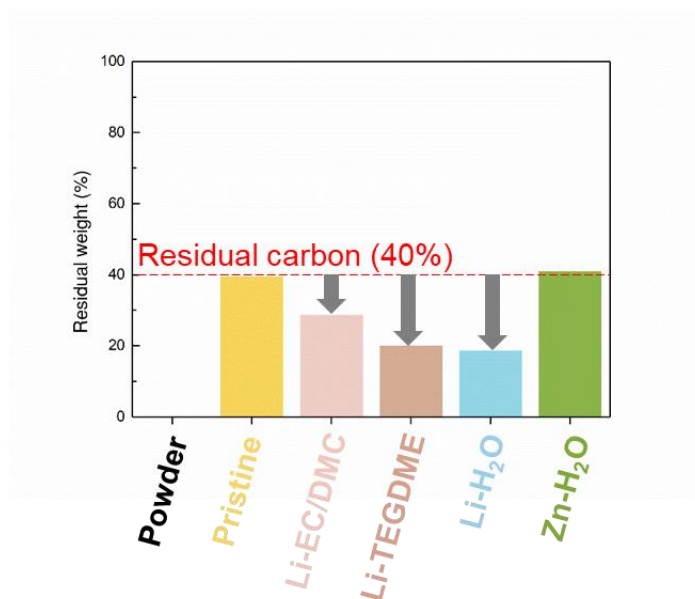


**Figure 4.10** Residual weight of the electrode after elevating the temperature to 600 °C.

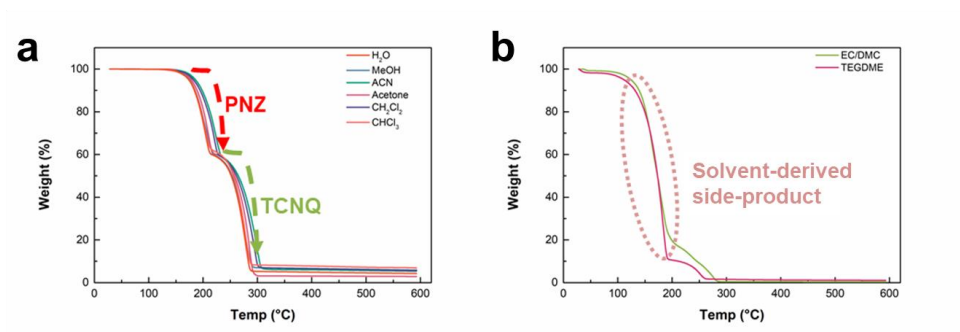


**Figure 4.11 Thermal investigation on the pre-formed product according to the various types of electrolytes and solvents.** TG curves of PNZ–TCNQ powder immersed in the electrolytes and pure solvents for 1 day, showing (a) same trend with the original PNZ–TCNQ and (b) altered trend from the original PNZ–TCNQ, respectively.

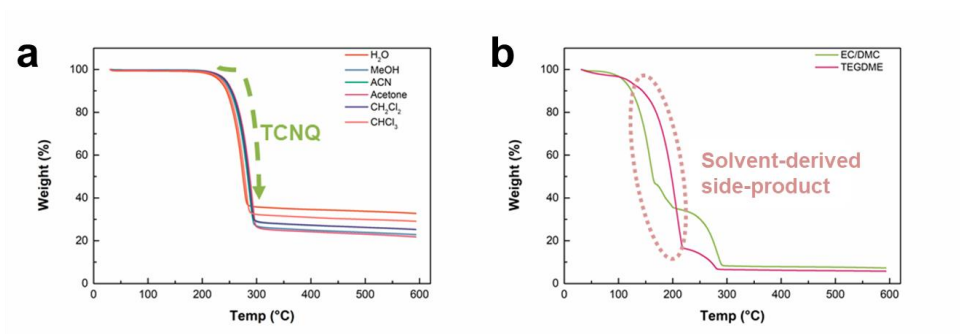


**Figure 4.12 Thermal investigation on the pre-formed product according to the various types of electrolytes and solvents.** TG curves of TCNQ powder immersed in the electrolytes and pure solvents for 1 day, showing (a) same trend with the original TCNQ and (b) altered trend from the original TCNQ, respectively.

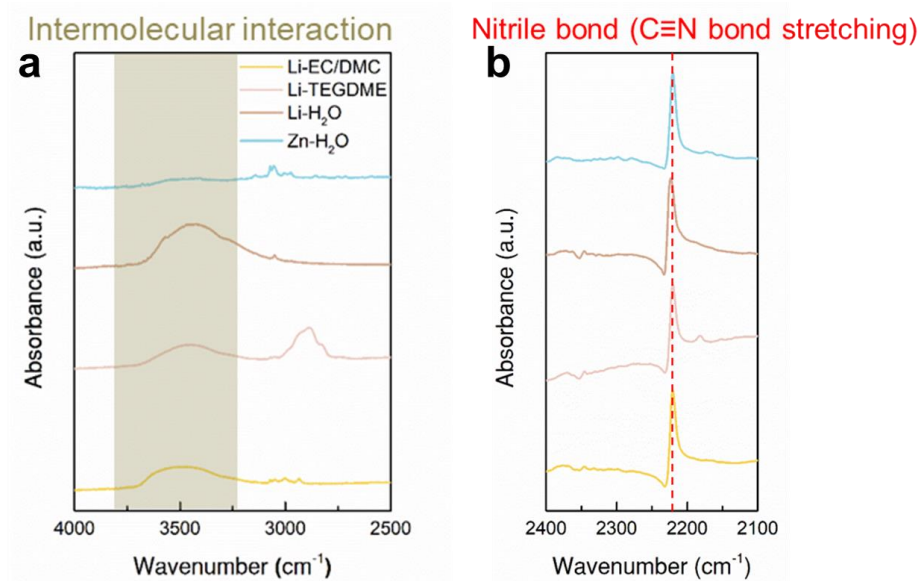


**Figure 4.13** Fourier-transform infrared spectroscopy (FTIR) curves of PNZ–TCNQ powder immersed in the electrolytes for 1 day in the range of (a) 4000–2500 cm<sup>-1</sup> and (b) 2400–2100 cm<sup>-1</sup>.



#### 4.3.4 The model for interplay between PNZ–TCNQ OCTC and electrolytes

Consequently, the model for interplay between PNZ–TCNQ OCTC and electrolytes can be summarized as illustrated in Figure 4.14. Li-EC/DMC and Li-TEGDME electrolytes produce the both salt/TCNQ-derived side-product and solvent/TCNQ-derived side-product, while Li-aqueous electrolytes only forms the salt/TCNQ side-product. Nevertheless, PNZ–TCNQ OCTC maintains its initial state in the Zn-aqueous electrolyte without any side reaction, indicating the high compatibility and stability.

Distinctive features of the crystal structure of OCTC could enhance the intrinsic material properties of constituting monomers,<sup>[18]</sup> thus the interplay with electrolytes may affect the material properties since it destructs the original OCTC structure through the ion and solvent molecule insertion. The characteristic structure of PNZ–TCNQ OCTC should be maintained to exhibit the improved electrochemical performances. Therefore, it is also important to investigate whether the pre-formed side-product is maintained or destroyed during cycling, or the new type of degradation arises in the intermediate phase of discharging and charging processes. We further performed the *ex situ* TG analysis of the PNZ–TCNQ OCTC electrodes, obtained at the intermediate states during battery cycling, as presented in Figure 4.15. Surprisingly, all the *ex situ* TG curves and corresponded derivative function curves of the PNZ–TCNQ OCTC electrodes, in each electrolyte during the discharging and charging processes, clearly shows the reversible behaviors. This implies that the pre-

formed side-products are maintained after cycling and the PNZ–TCNQ OCTC in Zn-aqueous electrolyte does not still form the electrolyte-derived side-product after cycling. As a result, the most compatible battery system to the PNZ–TCNQ OCTC is the Zn aqueous battery, which can preserve its own crystal structure without any unwanted side reaction. Furthermore, as shown in Figure 4.16, it is observed that the peak pattern of the PNZ–TCNQ OCTC electrode is preserved as cycle goes on.

One more different point of Zn-aqueous electrolyte was already observed in the electrochemical profiles, as shown in Figure 4.6. PNZ–TCNQ OCTC electrode in Zn aqueous battery could only fully utilize the redox-activity of both PNZ and TCNQ with the four-electron redox reaction. Realizing the full redox activation of PNZ–TCNQ OCTC may be related to the maintenance of its crystal structure. It is speculated that the pre-formed TCNQ-based side-product weakens the intermolecular interaction forces between PNZ and TCNQ molecules. The reason of this argument is that the electronic charge can be compensated to the acceptor molecule of TCNQ through interacting with Li ion, while the electronic charge state of donor molecule of PNZ cannot be satisfied. Therefore, weakened crystal structure of OCTC could not endure to accept the electron for full redox activity regarding the PNZ redox reaction, may resulting in the structural degradation of the active material. On the other hand, the well-maintained structure of OCTC in Zn aqueous battery could get four electrons and two zinc ions during discharging process without the destruction of the active material.

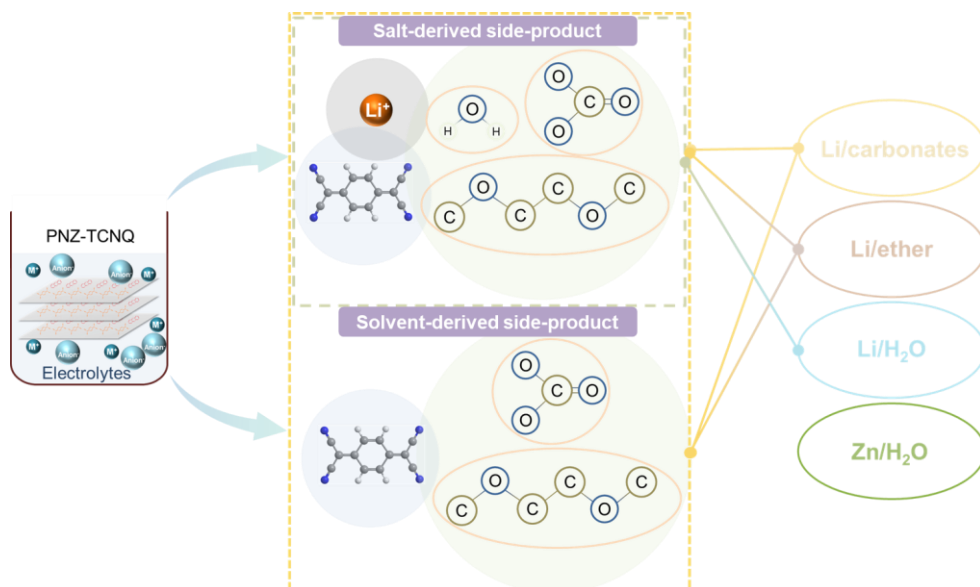


**Figure 4.14** Schematic diagram of the interplay model between active material and electrolytes.

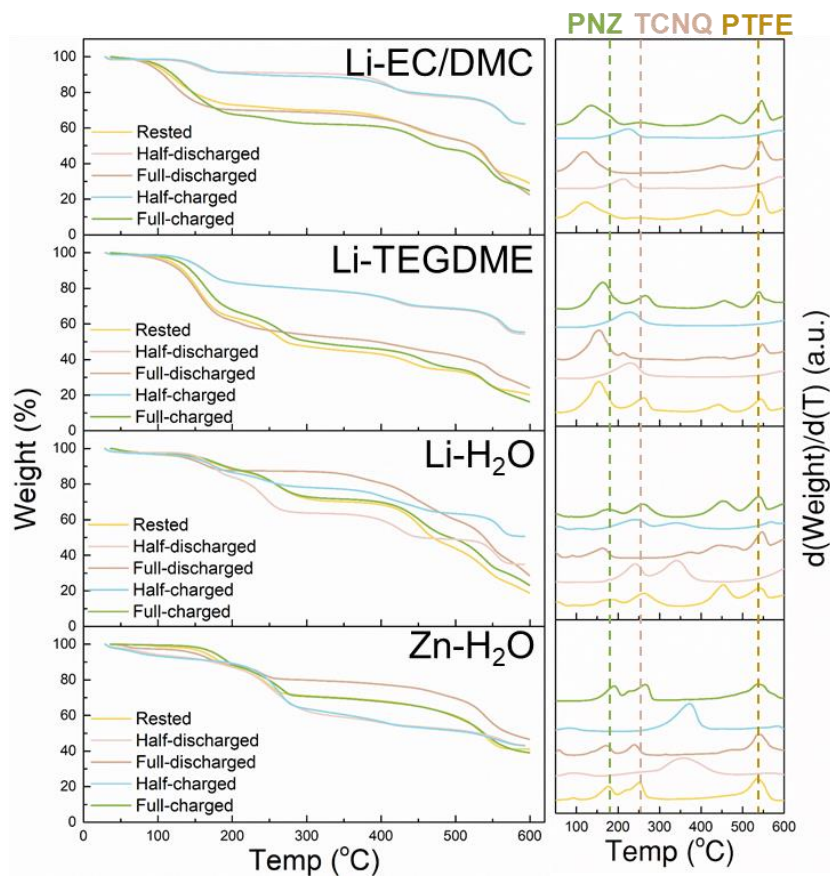


**Figure 4.15** *Ex situ* TG curves (left) and correlated TG derivative curves (right) of PNZ–TCNQ electrodes in (Top-to-bottom: 1M LiTFSI in EC/DMC, 1M LiTFSI in TEGDME, 1M LiTFSI in H<sub>2</sub>O, and 1M Zn(TFSI)<sub>2</sub> in H<sub>2</sub>O)

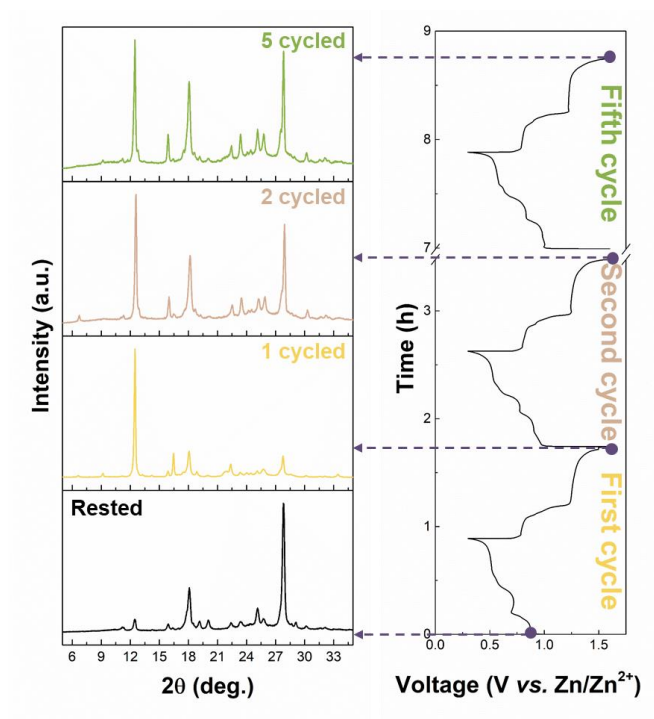


**Figure 4.16** *Ex situ* XRD and correlated capacity–voltage profile of PNZ–TCNQ OCTC electrode after further cycling.

#### 4.3.5 Electrochemical performances of PNZ–TCNQ OCTC in Zn aqueous battery

Hence, further electrochemical performances regarding the rate and cycle performances were further investigated for PNZ–TCNQ OCTC in Zn aqueous battery. Notably, conductive aqueous medium is expected to have a synergetic effect with the conducting OCTC electrode, showing the high rate-capable performance. Accordingly, the rate performances were tested with the various methods to check the feasibility for the commercialization. First, the practical specific capacities of PNZ–TCNQ OCTC and its constituting monomers at various rates of the current density are shown in Figure 4.17. The PNZ–TCNQ OCTC electrode exhibited ~96% of the theoretical capacity ( $280 \text{ mAh g}^{-1}$  for four-electron redox reaction) at the moderate current rate of  $50 \text{ mA g}^{-1}$  (~0.18 C-rate), while PNZ and TCNQ monomers exhibited ~85% and ~45% of their theoretical capacities even at the lower current rate of  $20 \text{ mA g}^{-1}$  (~0.08 C-rate), respectively. This result was attributed to the enhanced conductive nature of the PNZ–TCNQ OCTC compared to the donor and acceptor molecules. Furthermore, the PNZ–TCNQ OCTC electrode exhibited ~60% of the theoretical capacity at an extremely high current rate of  $1 \text{ A g}^{-1}$ , corresponding to a capacity of  $164 \text{ mAh g}^{-1}$ . The rate performances in terms of the commercialization, such as various contents ratio of the active material and the material loading density regarding the areal capacity, were further examined to show the capability of the PNZ–TCNQ OCTC electrode in Zn aqueous battery. The limitation of the organic redox-active molecules about the low active material

content in the electrode of 20%-60%,<sup>[4-6, 40]</sup> for the purpose of utilizing the large amount of conducting agent, was attributed to the poor electrical conductivity of organic-based electrode materials. In this respect, we also tested the synergetic combinations of conductive aqueous medium and OCTC electrode with various active material contents. Figure 4.18 presents the discharge capacities and the energy densities of the PNZ–TCNQ OCTC electrodes with five types of electrode compositions. The electrode containing the active material above 90% showed the decreased capacity, however, the 65%, 70%, and 80% of the active material contents delivered the high specific capacity ( $\sim 210 \text{ mAh g}^{-1}$ ) more than 70% of the theoretical capacity. On the other hand, it is highly required to develop the electrode that can be mass-loaded, resulting in the high areal capacity, to achieve the high energy density of the rechargeable batteries. Figure 4.19 shows the discharge specific capacities and the areal capacities at various active material loading density with the active material contents of 60%. The active material could be loaded on the electrode for the loading density of  $45 \text{ mg cm}^{-2}$  with the thickness of  $580 \text{ }\mu\text{m}$ , delivering the discharge specific capacity of  $223 \text{ mAh g}^{-1}$  and the areal capacity of  $\sim 10 \text{ mAh cm}^{-2}$ . Same test with the different active material contents of 40% and 80% was conducted as illustrated in Figures 4.20 and 4.21, and the obtained areal capacities and those of representative electrode material in Zn aqueous batteries are depicted in Figure 4.22. Other reported electrode materials regarding the organic<sup>[41-45]</sup> and inorganic<sup>[46-53]</sup>-based materials usually showed the areal capacity of about  $0.5\text{--}2.1 \text{ mAh cm}^{-2}$ , however, our work demonstrates the extremely high areal capacity above  $8 \text{ mAh cm}^{-2}$ . Ragone plots of

the PNZ–TCNQ OCTC and the other electrode materials<sup>[41-45, 48-51]</sup> are also illustrated in Figure 4.23, and it is observed that the energy densities and correlated power densities of PNZ–TCNQ OCTC electrode could reach the current level of the inorganic-based electrode materials. These results prove the highly feasible rate performance of PNZ–OCTC electrode, which can be comparable or exceeded to the currently used inorganic-based electrode materials.

As presented in Figure 4.24, the cycle stability test was also performed, and the PNZ–TCNQ OCTC electrode in Zn aqueous battery could retain 68% of its initial capacity after 50 cycles. Cycle performance was improved compared to that in reported Li non-aqueous batteries,<sup>[18]</sup> however, it still has a further room to be enhanced. This signifies that the unsolved problem is still existent, and the remained cause is already observed in Figure 4.15. Dissolution phenomenon was identified from the increased residual weight of the intermediate states of the electrodes. The relative portion of the conductive carbon in the electrode would increase if the active material and binder disappears in the electrode, and the only possible scenario is the dissolution of the active material. Dissolution also leads to the backward reaction of re-precipitation, and the re-precipitated active material may form the different morphology and be deposited at random site, even far from the conducting agent, resulting in the dead volume evolution.



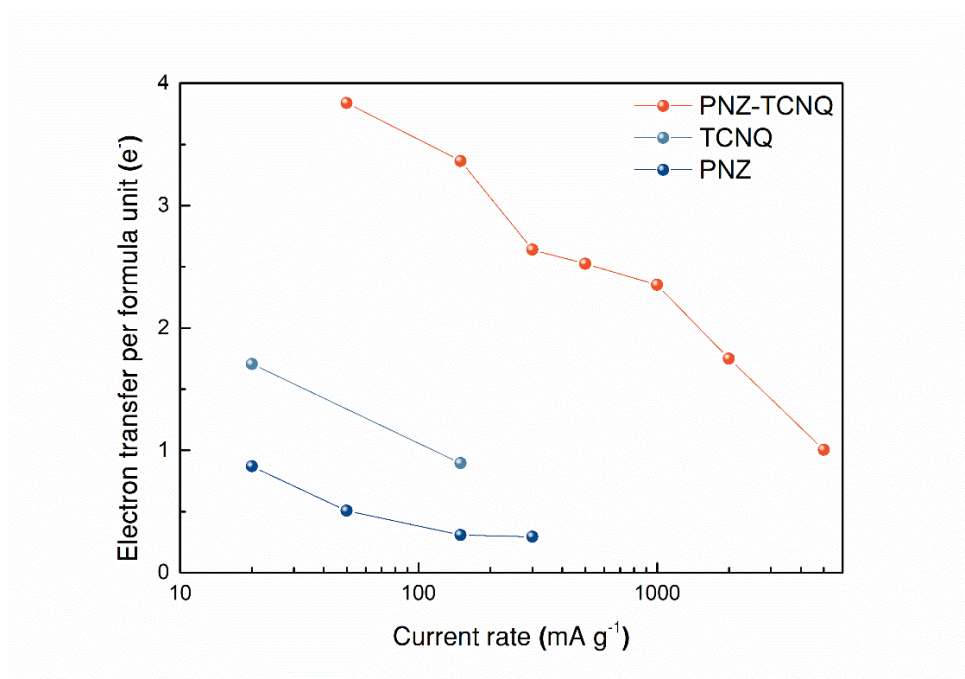


**Figure 4.17** Electron transfer per formula unit of PNZ–TCNQ and its constituting monomers in the various current rates.

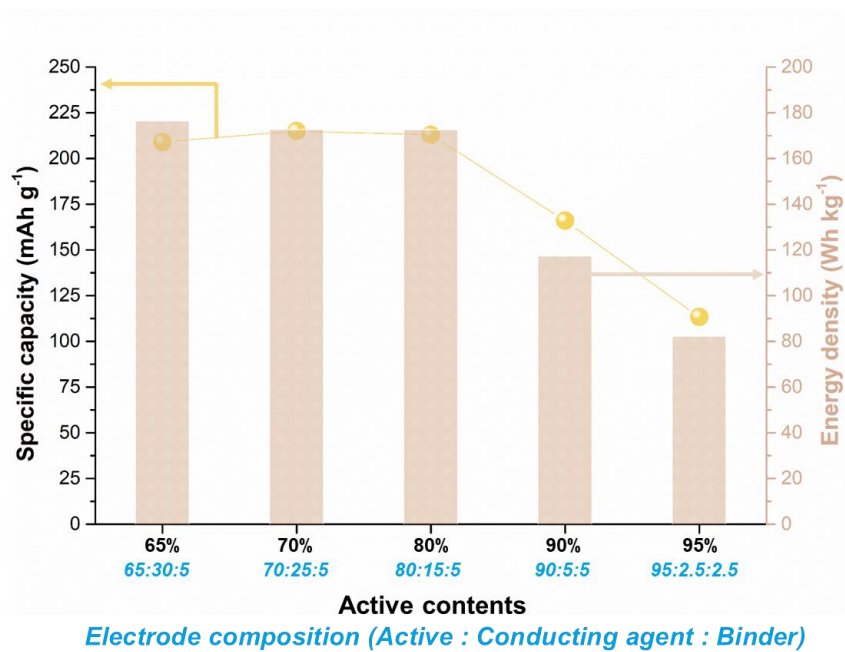


**Figure 4.18** High active contents test of PNZ–TCNQ electrodes in Zn aqueous batteries.

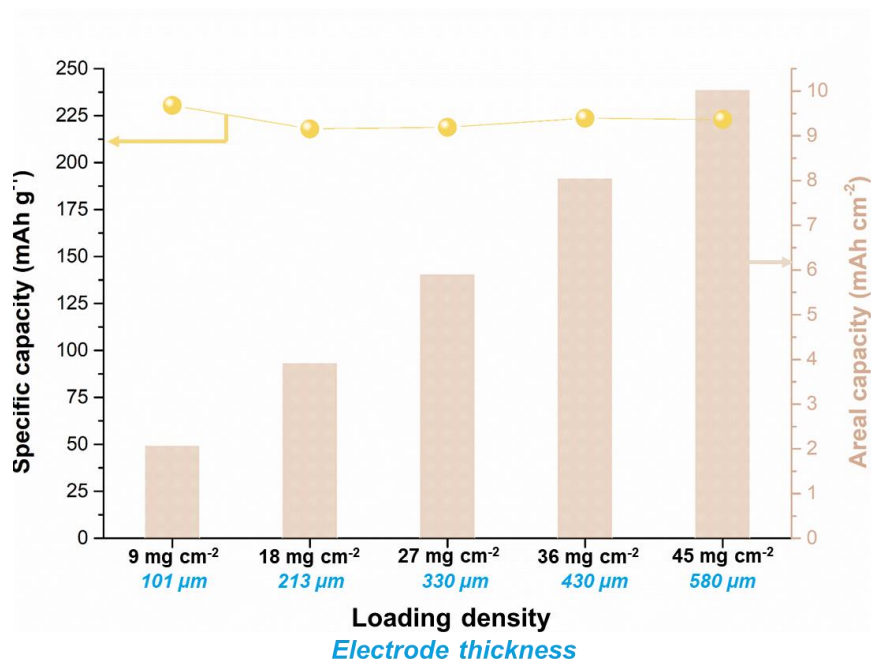


**Figure 4.19** Specific and areal capacities of PNZ-TCNQ electrodes with the active contents of 60% in the various active material loading density.

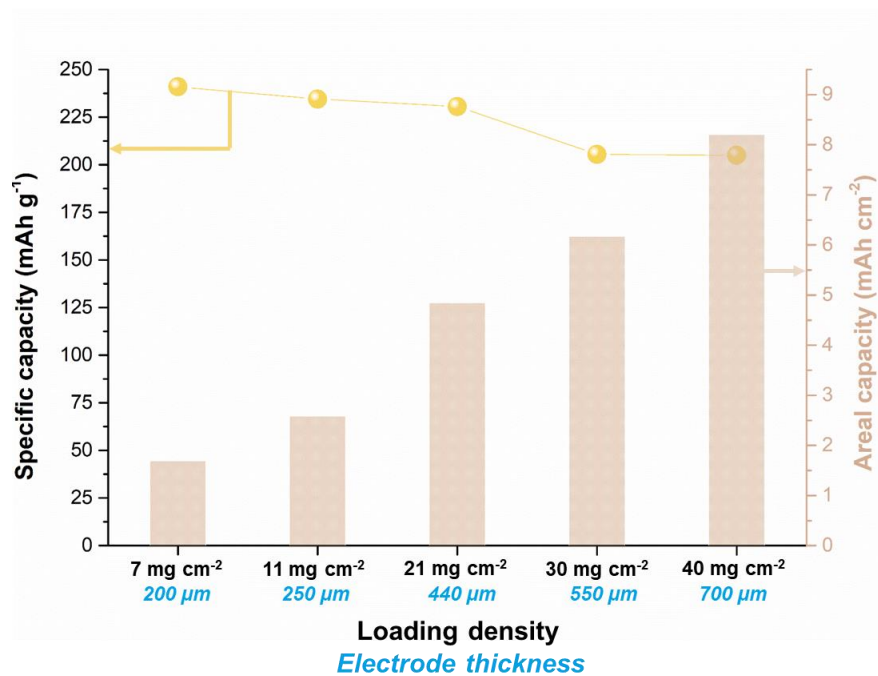


**Figure 4.20** Specific and areal capacities of PNZ-TCNQ electrodes with the active contents of 40% in the various active material loading density.

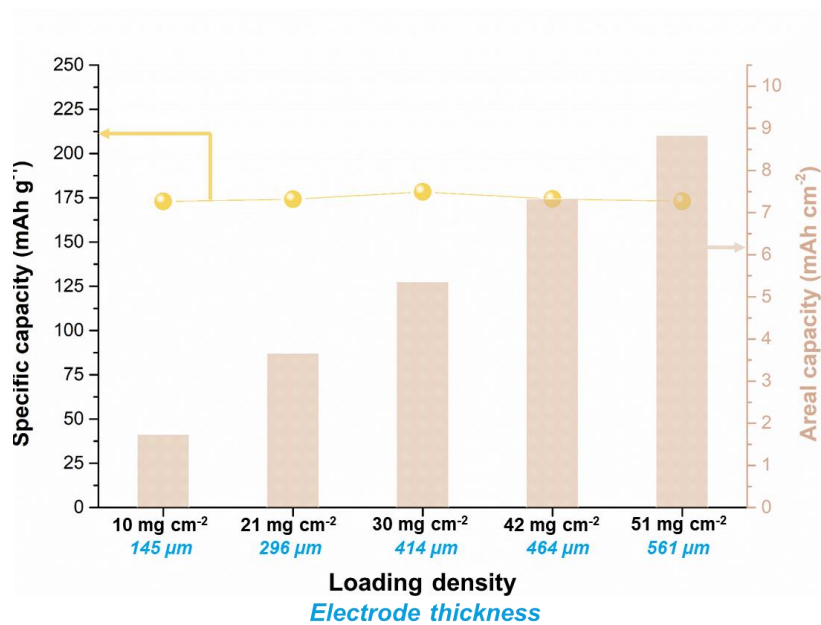


**Figure 4.21** Specific and areal capacities of PNZ–TCNQ electrodes with the active contents of 80% in the various active material loading density.

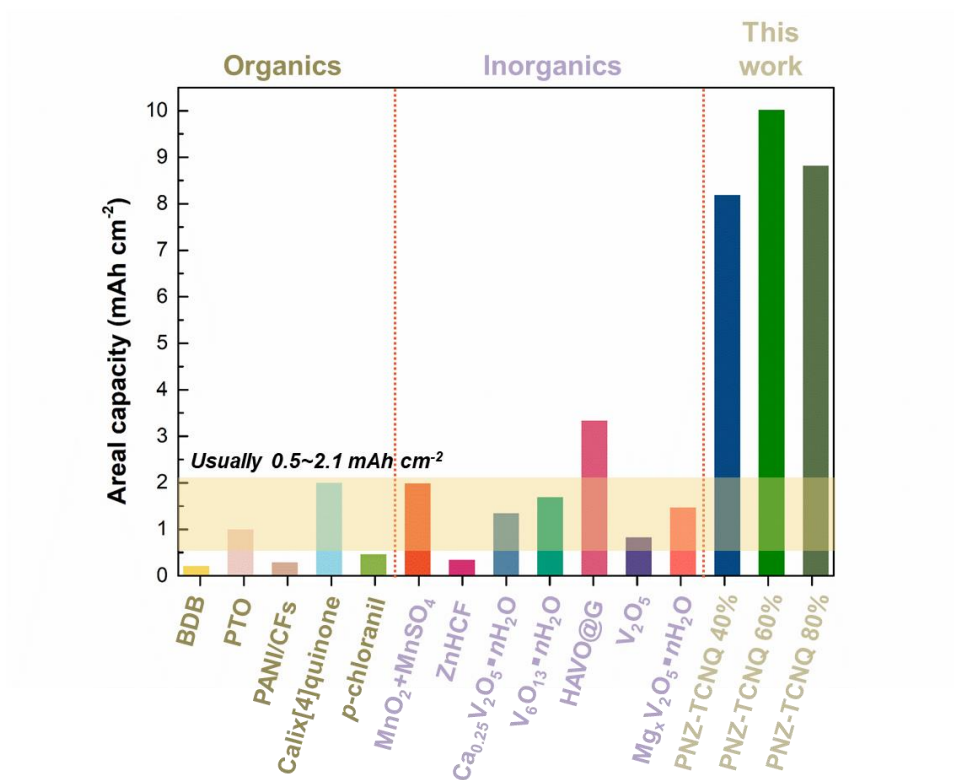


**Figure 4.22** Areal capacity comparison of PNZ–TCNQ with representatively reported electrodes in Zn aqueous batteries.

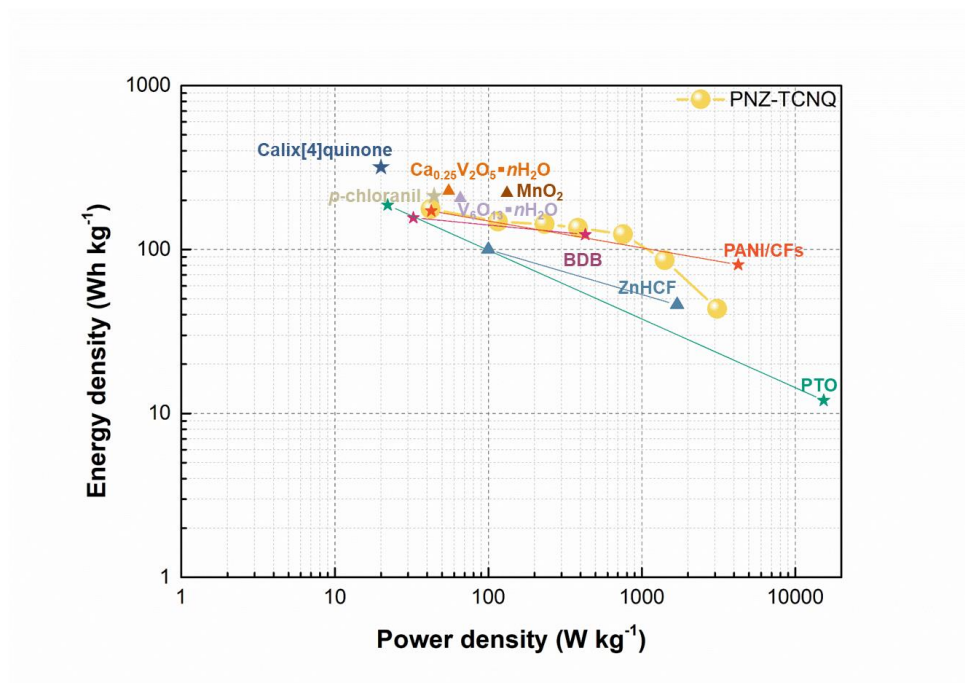


**Figure 4.23** Ragone plot of PNZ–TCNQ with representatively reported electrodes in Zn aqueous batteries.

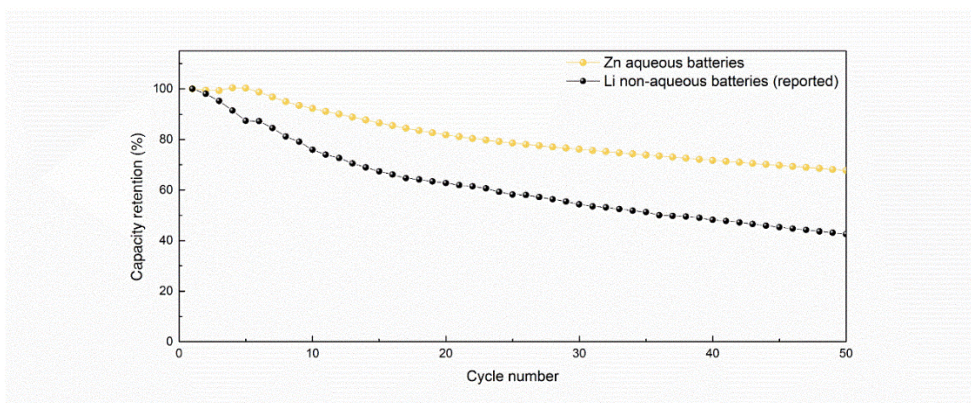


**Figure 4.24** Capacity retention curves of PNZ-TCNQ in Zn aqueous and Li non-aqueous batteries.



#### 4.3.6 Quantitative and qualitative analysis on dissolution behavior of organic redox-active compounds

Therefore, quantitative and qualitative analysis on dissolution of active material during cycling were conducted to define the remained issue of the capacity fading. First, *ex situ* electrode weight measurement was performed to compare the solubility of the intermediate phases of PNZ–TCNQ OCTC. Figure 4.25 present the electrode weight change, obtained from the electrode disassembled in each state-of-charge, and the deviation between the experimental and theoretical weight change, respectively. Theoretical electrode weight change was calculated considering the addition of the Zn ion weight according to the insertion of the Zn ion. Overall electrode weights are well-matched to the theoretically expected values, however, it is observed that there are slight negative deviations in the middle of the discharging and charging processes. Electrodes at 2/3 discharge and 1/3 charge show the largest weight loss of 5.37% and 3.46%, respectively. To further raise the reliability of this experiment and examine the dissolution behaviors of the constituting monomers, measuring electrode weight changes were also conducted for the PNZ and TCNQ molecules. PNZ and TCNQ molecules show the mush severe weight loss during cycling, and they lose the active material weight at the fully discharged state to ~21% and ~27%, respectively. As depicted in 4.26, PNZ–TCNQ OCTC exhibited the better cycle stability compared to those of its constituting monomers as the quantitative dissolution analysis. (Figure 4.27) Moreover, they could not entirely recover their lost weight after one cycling, exhibiting the additional weight loss of ~6% and ~2%

compared to the initial state. It can be stated that some of the dissolved active material can be recovered after cycling, however, the vanished amount of active materials continuously increases. Furthermore, the re-precipitated active material may be hard to participate in redox reaction since that it is possible to be deposit as a dead volume on the electrode surface.

On the other hand, investigating which constituent mainly dissolves were further examined through the visual studies. The electrodes obtained after cell disassembly at each state-of-charge during cycling were immersed in the pure water solvent for 1 day, as presented in Figure 4.28. There was no significant color change of the solvents containing PNZ–TCNQ OCTC electrodes. However, it is expected that the PNZ in the OCTC mainly dissolved during cycling for the sake of that the PNZ monomer also does not have the color change of the *ex situ* samples, while TCNQ monomer undergoes the color change to blue in the middle of the discharging and charging processes. The results from the ultraviolet–visible spectroscopy (UV–vis spectroscopy) supports likewise the statement of the dominant PNZ dissolution. Figure 4.29 shows the UV–vis spectra of the water solvents storing the *ex situ* electrode samples of PNZ–TCNQ OCTC, and its constituting monomers. Characteristic peaks of PNZ are observed at 250 and 360 nm, and the UV–vis spectra of PNZ–TCNQ OCTC also shows the two distinct peaks located at the same position of PNZ, while TCNQ exhibits the two different peaks at 325 and 600 nm. It is hard to argue that the dissolution of the PNZ–TCNQ OCTC is only come from the PNZ monomer because the soluble TCNQ species during cycling were already observed

in the quantitative dissolution analysis. Nevertheless, it can be speculated that the PNZ is more dominantly dissolved species compared to the TCNQ, in PNZ–TCNQ OCTC electrode.

In order to further increase the capacity retention for the long-term cycling, it is highly required to solve the problems derived from the dissolution of the active material such as shuttling effect, re-precipitated dead volume, and continuous loss of active material. Utilizing the separator that redox-active molecules cannot pass through and coating the electrode surface for capturing the dissolved redox-active species can be the solution for this issue. The mentioned strategy here will be treated in the further work to lastly optimize the battery performance of the OCTC rechargeable batteries.

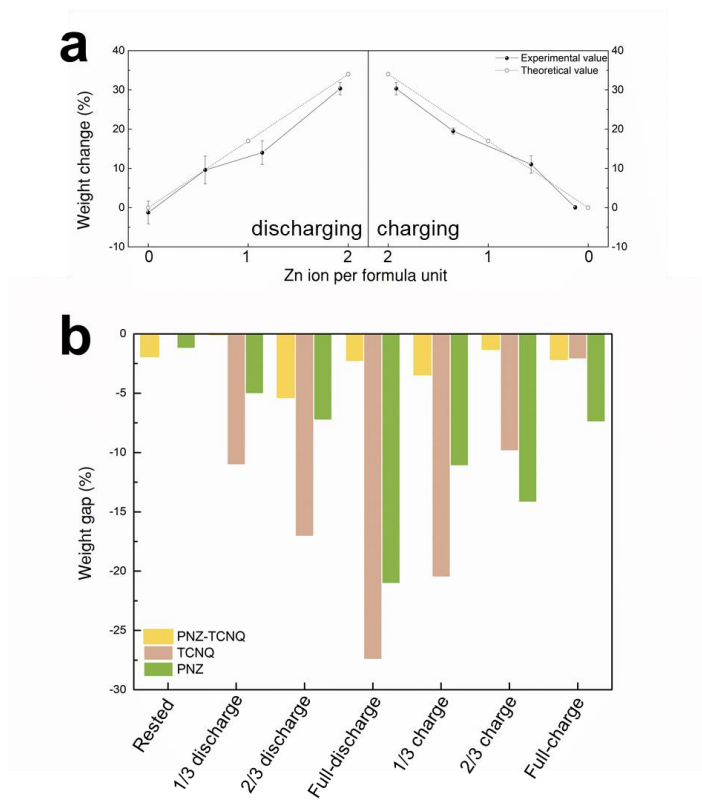


**Figure 4.25 Quantitative analysis on dissolution behavior.** (a) Electrode weight change and (b) the deviation of the electrode weight change between the experimental and theoretical values during battery cycling.

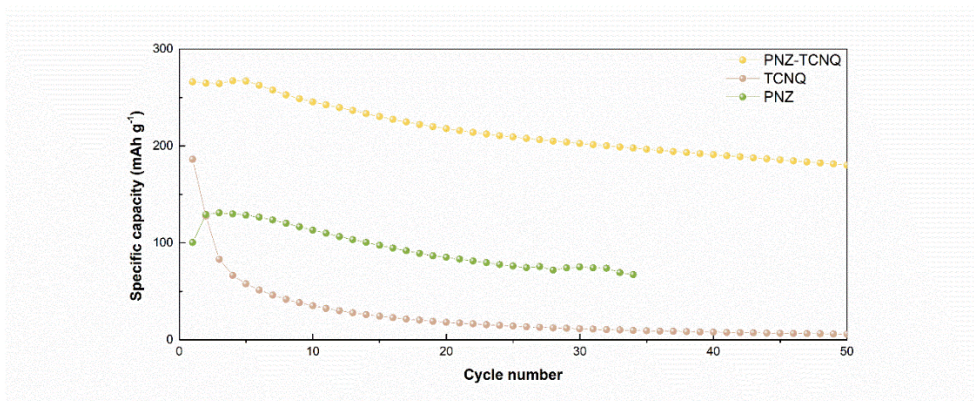


**Figure 4.26** Capacity retention curves of PNZ–TCNQ OCTC electrode and its constituting monomers (PNZ and TCNQ).

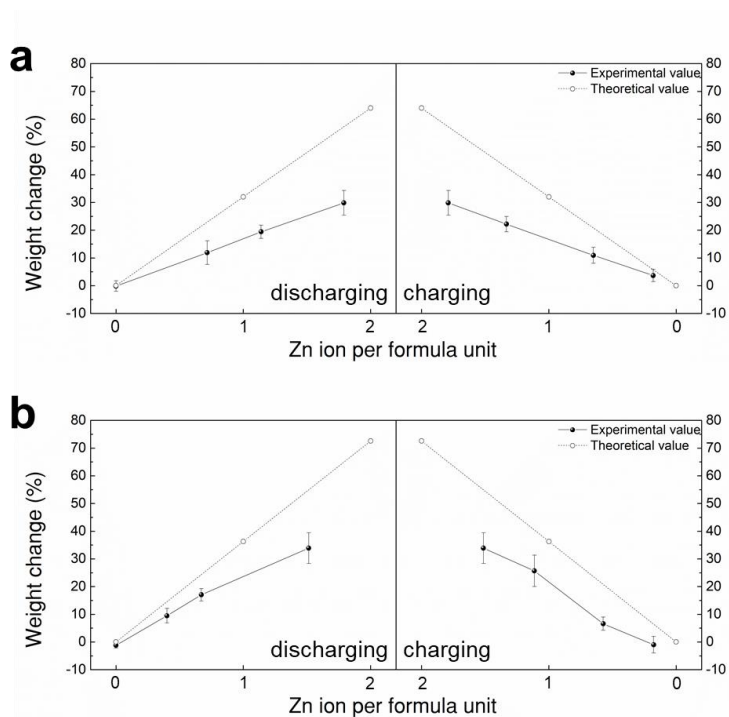


**Figure 4.27** Quantitative analysis on dissolution behavior for the constituting monomers of PNZ and TCNQ. Electrode weight change during battery cycling for (a) TCNQ and (b) PNZ.

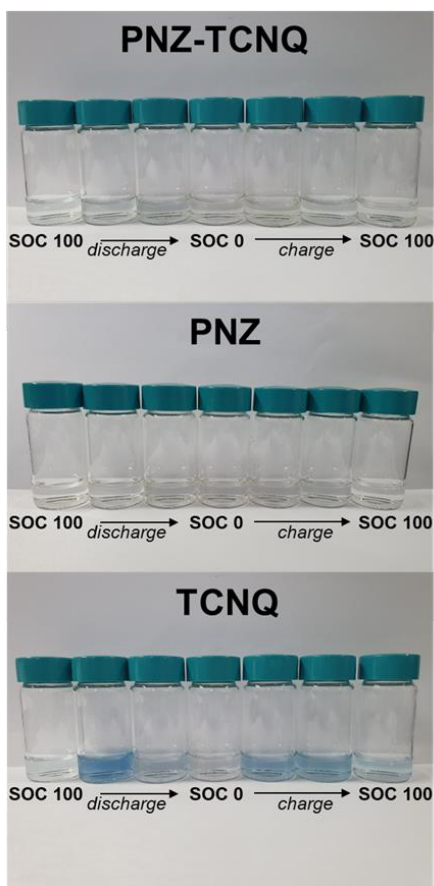


**Figure 4.28** Color change of the water solvents storing the PNZ–TCNQ and its constituting monomers at different state-of-charge.

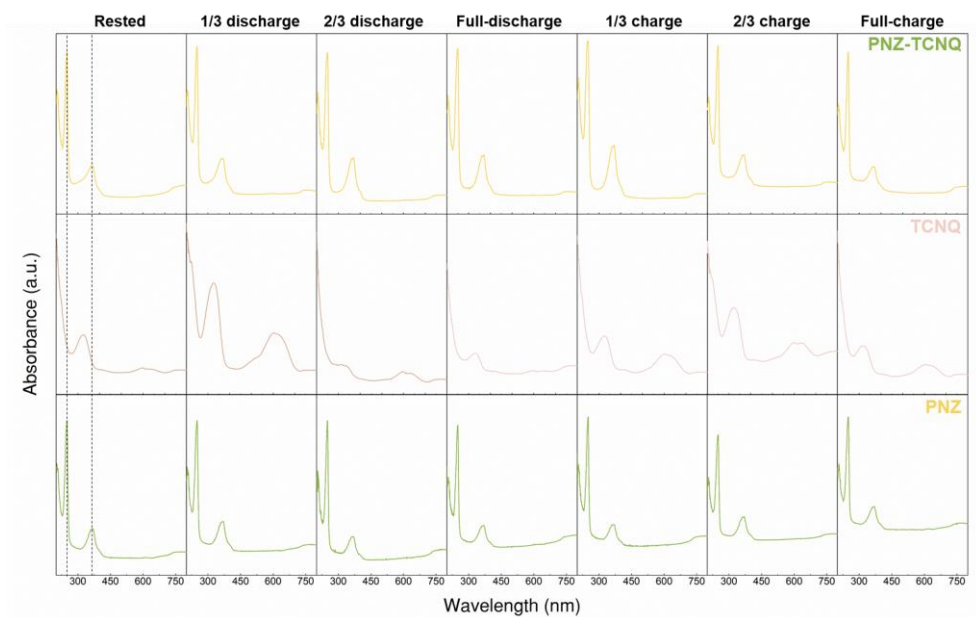


**Figure 4.29 Qualitative analysis on dissolution behavior.** *Ex situ* UV-vis spectroscopy of the PNZ-TCNQ and its constituting monomers (PNZ and TCNQ) during battery cycling.



#### 4.4 Concluding remarks

In summary, we elucidated the energy storage mechanism of model PNZ – TCNQ OCTC and applied it to the most compatible battery system, which can realize the full redox-activity with the best electrochemical performances. Due to the structural characteristics, priorly reported PNZ–TCNQ OCTC electrode could increase the electrical conductivity and reduce the solubility to solvent with the spontaneous reordering of the molecules, however, limited energy density originated from the redox-inactivity of PNZ component still needed to be improved. Interplay between the organic electrode material and electrolytes, which is suggested as the new factor determining the redox mechanism of organic redox-active compounds, was focused to be investigated, and the PNZ–TCNQ OCTC was applied to the various types of electrolytes with substituting the charge carrying ions and solvents. PNZ–TCNQ OCTC electrode underwent the different redox reaction pathways according to the electrolyte types (Li-carbonates, Li-ether, Li-aqueous, and Zn-aqueous electrolytes), and the PNZ–TCNQ OCTC electrode in Zn-aqueous electrolyte only could fully utilize the redox-activity of both PNZ and TCNQ monomers with four-electron redox reaction, while it has a two-electron redox reaction with the TCNQ monomer in other Li-based electrolytes. In order to investigate the origin of different redox reaction pathways, structural, thermal, and chemical analysis were further demonstrated, and the initially formed new phase of the active material just after electrolyte exposure was observed among the utilized electrolytes without the Zn-aqueous electrolyte. We figured out that the pre-formed

product is occurred by the interplay between the TCNQ molecule and the electrolytes regarding the charge carrying ions and the solvent molecules. We speculated that realizing the full redox reaction of PNZ–TCNQ OCTC in Zn-aqueous electrolyte may be possible due to the maintenance of its crystal structure without any side reaction. The other electrolytes induce to form the pre-formed TCNQ-based side-product, which weakens the intermolecular interaction between PNZ and TCNQ molecules, further resulting in the material degradation. Accordingly, electrochemical performances regarding the rate and cycle performances were further tested for PNZ–TCNQ OCTC in Zn aqueous battery. Synergetic effect of the conductive aqueous medium and OCTC could achieve the extremely high active material contents of 95% and the material loading density of  $45 \text{ mg cm}^{-2}$  with the areal capacity about  $10 \text{ mAh cm}^{-2}$ . Cycle performance of PNZ–TCNQ OCTC in Zn aqueous battery was improved compared to that in reported Li-non aqueous batteries, however, there still have a further room to be optimized. Quantitative and qualitative analysis on dissolution behavior of PNZ–TCNQ OCTC in Zn aqueous battery revealed that the dissolved amount of the active material at the intermediate phases increased, while the pristine state is slightly soluble and most of the dissolved species recovered after one cycle. We expected that dissolution problem derives several issues such as continuous loss of active material and evolution of the dead volume due to the randomly occurred re-precipitation. Utilizing the ion-selective separator that active material cannot pass through or coating the electrode surface for capturing the dissolved species can be the strategy that will be treated in further work. This

study suggests the energy storage behavior of organic active materials regarding the interaction with electrolytes, further emphasizing the structural stability and the dissolution behavior. Moreover, the most compatible combination of conductive aqueous medium and conducting OCTC shows the great potential to be highly feasible for commercialization of the organic rechargeable batteries.

## 4.5 References

- [1] J. M. Tarascon, M. Armand, *Nature* **2001**, 414, 359.
- [2] M. Armand, J.-M. Tarascon, *nature* **2008**, 451, 652.
- [3] D. Larcher, J.-M. Tarascon, *Nature chemistry* **2015**, 7, 19.
- [4] Y. Liang, Z. Tao, J. Chen, *Advanced Energy Materials* **2012**, 2, 742.
- [5] Z. Song, H. Zhou, *Energy & Environmental Science* **2013**, 6, 2280.
- [6] S. Lee, G. Kwon, K. Ku, K. Yoon, S. K. Jung, H. D. Lim, K. Kang, *Advanced materials* **2018**, 30, 1704682.
- [7] S. Lee, J. Hong, K. Kang, *Advanced Energy Materials* **2020**, 10, 2001445.
- [8] Y. Liang, P. Zhang, S. Yang, Z. Tao, J. Chen, *Advanced Energy Materials* **2013**, 3, 600.
- [9] Y. Liang, P. Zhang, J. Chen, *Chemical Science* **2013**, 4, 1330.
- [10] M. Yao, H. Senoh, S.-i. Yamazaki, Z. Siroma, T. Sakai, K. Yasuda, *Journal of Power Sources* **2010**, 195, 8336.
- [11] H. g. Wang, S. Yuan, D. l. Ma, X. l. Huang, F. l. Meng, X. b. Zhang, *Advanced Energy Materials* **2014**, 4, 1301651.
- [12] K. Sakaushi, E. Hosono, G. Nickerl, T. Gemming, H. Zhou, S. Kaskel, J. Eckert, *Nature communications* **2013**, 4, 1.
- [13] D.-H. Yang, Z.-Q. Yao, D. Wu, Y.-H. Zhang, Z. Zhou, X.-H. Bu, *Journal of Materials Chemistry A* **2016**, 4, 18621.

- [14] S. Wang, Q. Wang, P. Shao, Y. Han, X. Gao, L. Ma, S. Yuan, X. Ma, J. Zhou, X. Feng, *Journal of the American Chemical Society* **2017**, 139, 4258.
- [15] M. Lee, J. Hong, H. Kim, H. D. Lim, S. B. Cho, K. Kang, C. B. Park, *Advanced Materials* **2014**, 26, 2558.
- [16] H. Wang, P. Hu, J. Yang, G. Gong, L. Guo, X. Chen, *Advanced materials* **2015**, 27, 2348.
- [17] M.-S. Kwon, A. Choi, Y. Park, J. Y. Cheon, H. Kang, Y. N. Jo, Y.-J. Kim, S. Y. Hong, S. H. Joo, C. Yang, *Scientific reports* **2014**, 4, 7404.
- [18] S. Lee, J. Hong, S.-K. Jung, K. Ku, G. Kwon, W. M. Seong, H. Kim, G. Yoon, I. Kang, K. Hong, H. W. Jang, K. Kang, *Energy Storage Materials* **2019**, 20, 462.
- [19] J. P. Pender, G. Jha, D. H. Youn, J. M. Ziegler, I. Andoni, E. J. Choi, A. Heller, B. S. Dunn, P. S. Weiss, R. M. Penner, *ACS nano* **2020**, 14, 1243.
- [20] H. Wang, Y. I. Jang, B. Huang, D. R. Sadoway, Y. M. Chiang, *Journal of the Electrochemical Society* **1999**, 146, 473.
- [21] X. Hao, X. Lin, W. Lu, B. M. Bartlett, *ACS applied materials & interfaces* **2014**, 6, 10849.
- [22] D. Guan, J. A. Jeevarajan, Y. Wang, *Nanoscale* **2011**, 3, 1465.
- [23] F. Lai, X. Zhang, H. Wang, S. Hu, X. Wu, Q. Wu, Y. Huang, Z. He, Q. Li, *ACS applied materials & interfaces* **2016**, 8, 21656.

- [24] J. Geng, J.-P. Bonnet, S. Renault, F. Dolhem, P. Poizot, *Energy & Environmental Science* **2010**, 3, 1929.
- [25] H. Kim, D.-H. Seo, G. Yoon, W. A. Goddard III, Y. S. Lee, W.-S. Yoon, K. Kang, *The journal of physical chemistry letters* **2014**, 5, 3086.
- [26] M. Lee, J. Hong, J. Lopez, Y. Sun, D. Feng, K. Lim, W. C. Chueh, M. F. Toney, Y. Cui, Z. Bao, *Nature Energy* **2017**, 2, 861.
- [27] S. Lee, J. E. Kwon, J. Hong, S. Y. Park, K. Kang, *Journal of Materials Chemistry A* **2019**, 7, 11438.
- [28] S. Lee, K. Lee, K. Ku, J. Hong, S. Y. Park, J. E. Kwon, K. Kang, *Advanced Energy Materials* **2020**, 10, 2001635.
- [29] S. Lee, J. Hong, S.-K. Jung, K. Ku, G. Kwon, W. M. Seong, H. Kim, G. Yoon, I. Kang, K. Hong, *Energy Storage Materials* **2019**, 20, 462.
- [30] Z. Song, Y. Qian, M. Otani, H. Zhou, *Advanced Energy Materials* **2016**, 6, 1501780.
- [31] V. W. h. Lau, I. Moudrakovski, J. Yang, J. Zhang, Y. M. Kang, *Angewandte Chemie* **2020**, 132, 4052.
- [32] H. Sun, M. Wang, X. Wei, R. Zhang, S. Wang, A. Khan, R. Usman, Q. Feng, M. Du, F. Yu, *Crystal Growth & Design* **2015**, 15, 4032.
- [33] H. Zhao, R. Heintz, X. Ouyang, K. Dunbar, C. Campana, R. Rogers, *Chemistry of materials* **1999**, 11, 736.
- [34] A. Nafady, A. M. Bond, A. P. O'Mullane, *Inorganic chemistry* **2009**, 48, 9258.

- [35] N. Takahashi, K. Yakushi, K. Ishii, H. Kuroda, *Bulletin of the Chemical Society of Japan* **1976**, 49, 182.
- [36] A. Nafady, A. P. O'Mullane, A. M. Bond, A. K. Neufeld, *Chemistry of materials* **2006**, 18, 4375.
- [37] T. Xu, T. A. Morris, G. J. Szulczewski, R. R. Amaresh, Y. Gao, S. C. Street, L. D. Kispert, R. M. Metzger, F. Terenziani, *The Journal of Physical Chemistry B* **2002**, 106, 10374.
- [38] Y. Lu, J. Chen, *Nature Reviews Chemistry* **2020**, 1.
- [39] Q. Zhao, W. Huang, Z. Luo, L. Liu, Y. Lu, Y. Li, L. Li, J. Hu, H. Ma, J. Chen, *Science advances* **2018**, 4, eaao1761.
- [40] H. Glatz, E. Lizundia, F. Pacifico, D. Kundu, *ACS Applied Energy Materials* **2019**, 2, 1288.
- [41] Z. Guo, Y. Ma, X. Dong, J. Huang, Y. Wang, Y. Xia, *Angewandte Chemie* **2018**, 130, 11911.
- [42] D. Kundu, P. Oberholzer, C. Glaros, A. Bouzid, E. Tervoort, A. Pasquarello, M. Niederberger, *Chemistry of materials* **2018**, 30, 3874.
- [43] F. Wan, L. Zhang, X. Wang, S. Bi, Z. Niu, J. Chen, *Advanced Functional Materials* **2018**, 28, 1804975.
- [44] H. Pan, Y. Shao, P. Yan, Y. Cheng, K. S. Han, Z. Nie, C. Wang, J. Yang, X. Li, P. Bhattacharya, *Nature Energy* **2016**, 1, 1.
- [45] W. Zhang, S. Liang, G. Fang, Y. Yang, J. Zhou, *Nano-Micro Letters* **2019**, 11, 69.

- [46] C. Xu, B. Li, H. Du, F. Kang, *Angewandte Chemie* **2012**, 124, 957.
- [47] L. Zhang, L. Chen, X. Zhou, Z. Liu, *Advanced Energy Materials* **2015**, 5, 1400930.
- [48] C. Xia, J. Guo, P. Li, X. Zhang, H. N. Alshareef, *Angewandte Chemie International Edition* **2018**, 57, 3943.
- [49] J. Lai, H. Zhu, X. Zhu, H. Koritala, Y. Wang, *ACS Applied Energy Materials* **2019**, 2, 1988.
- [50] N. Zhang, Y. Dong, M. Jia, X. Bian, Y. Wang, M. Qiu, J. Xu, Y. Liu, L. Jiao, F. Cheng, *ACS Energy Letters* **2018**, 3, 1366.
- [51] F. Ming, H. Liang, Y. Lei, S. Kandambeth, M. Eddaoudi, H. N. Alshareef, *ACS Energy Letters* **2018**, 3, 2602.



## Chapter 5. Conclusion

Organic redox-active compounds, which are concerned as the future sustainable electrode materials, have been suffered from their intrinsic material properties, impeding the electrochemical performances. In this thesis, I develop the novel material group, OCTCs, and apply them to viable organic electrode materials in rechargeable batteries. Due to their structural characteristics originated from forming the charge-transfer interaction, intermolecular interactions induced by the molecular rearrangement enhance the intrinsic material properties simultaneously utilizing only redox-active molecules. In chapter 2, I demonstrate the use of OCTC as a novel type of organic electrode material for the first time. General structural characteristics of complementary hydrogen bonds in layer and  $\pi$ - $\pi$  stacking between the layer improve the electrical conductivity and structural integrity. In particular, the electrical conductivity of the model compound of OCTC (PNZ-TCNQ) reaches one of the highest level among the reported organic electrodes. It results in the enhanced rate and cycle performances at a high current rate and practical electrode formulation ratios.

Nevertheless, limitation on battery performance of PNZ-TCNQ OCTC still remained. Overall low voltage and singular redox activity of TCNQ limits the energy density. Further investigation on solving the remained drawback are progressed in parallel. In chapter 3, I design a new donor molecule (DD), which exhibits the extremely high 4 V class, for altering the redox-inactive PNZ in PNZ-TCNQ OCTC

electrode. DD is rationally modified from the DMPZ, which were firstly developed as the high energy density organic cathode material, with substituting the redox center atoms to the Group 16 element of oxygen having high electronegativity. DD exhibits the stable *p*-type redox reaction with the highest redox potential of 4.10 V vs. Li/Li<sup>+</sup> among reported organics, even comparable to the currently used transition metal oxide-based electrode materials. DD monomer also shows the high rate performance and planar structure that is suitable to be applied as a constituent of OCTC. New OCTC with the DD (electron donor molecule) and TCNQ (electron acceptor molecule) is successfully fabricated as the similar mixing procedure of the PNZ–TCNQ OCTC. DD–TCNQ OCTC significantly improves the material properties of electrical conductivity and structural stability. Particularly, the electrical conductivity of DD–TCNQ OCTC ( $2.785 \times 10^{-7} \text{ S cm}^{-1}$ ) is located at the remarkable high value, even comparable to that of inorganic electrodes. Moreover, the original objective is achieved, exhibiting the enhanced energy density of  $\sim 560 \text{ Wh kg}^{-1}$  ( $\sim 390 \text{ Wh kg}^{-1}$  for PNZ–TCNQ OCTC). Designing the suitable constituent of the OCTC with the improved electrochemical performances can enrich the suggested novel material groups of OCTCs, to ultimately show the superior battery performances for the commercialization.

In Chapter 4, further investigation on the energy storage mechanism of model PNZ–TCNQ OCTC is performed to identify the origin of redox-inactive behavior of PNZ component in firstly applied model battery system and ultimately realize the full redox-activity of PNZ–TCNQ OCTC electrode. The redox

mechanism of organic electrode materials is currently suggested that it is affected from the sorts of electrolytes regarding the charge carrying ions and solvent molecules. Therefore, the redox behavior of PNZ–TCNQ OCTC according to the electrolytes is focused to be analyzed through varying the types of charge carrying ions and solvents. I observe that the redox reaction pathways of the model PNZ–TCNQ OCTC electrode differs according to the electrolyte types. Four representative types of redox reaction are categorized, and interestingly, PNZ–TCNQ OCTC electrode in Zn-aqueous electrolyte only can fully utilize the redox-activity of both PNZ and TCNQ molecules with four-electron redox reaction, while it exhibits the singular redox activity of TCNQ in other Li-based electrolytes. It is observed that the active material just after electrolyte exposure undergoes the immediate phase transformation without the Zn-aqueous electrolyte. I figure out the origin of the preformed product, which is revealed as the interplay between the TCNQ molecule and electrolytes through thermal and chemical analysis. I suggest the speculation of that realizing the full redox reaction of PNZ–TCNQ OCTC in Zn-aqueous electrolyte is possible due to the stable maintenance of its crystal structure without any side reaction, while other electrolytes induce the electrolyte-derived side-product formation occurring the structural degradation of OCTCs. Following with this result, synergetic effect of combining conductive aqueous medium and conductive OCTC results in the great rate performance, achieving the extremely high active material contents of 95% and the material loading density of  $45 \text{ mg cm}^{-2}$  with the areal capacity  $10 \text{ mAh cm}^{-2}$ . Cycle performance of PNZ–TCNQ OCTC in Zn

aqueous battery is additionally improved from that in reported Li-OCTC rechargeable batteries.

Application of the novel electrode material group for the future generation energy storage system was performed and further investigation for optimizing battery performances was conducted in this thesis. Although some issues on OCTCs that should be solved are still remained, I believe that this innovative approach to develop new organic electrode material candidates with enhanced material properties suggests the great promise to enlarge the feasible alternatives for the more sustainable batteries in the future. I hope that this thesis will contribute to give the intuition of creative design strategy and fundamental understanding on the intermolecular interaction of organics that are utilized as energy materials.

## Chapter 6. Abstract in Korean

### 국 문 초 록

휴대용 기기에서부터 대형 전기자동차에 이르는 다양한 전자제품들이 개발됨에 따라 리튬 이온 전지에 대한 수요가 꾸준히 증가해왔다. 그러나 현재 사용되고 있는 리튬 이온 전지는 제한된 자원 매장량, 좁은 범위의 물질 후보군, 낮은 지속 가능성을 야기하는 전이금속 기반의 전극 소재를 활용함으로써 생기는 문제점을 가지고 있다. 따라서, 미래형 에너지 저장 시스템에 활용될 대안으로 산화/환원 활성을 가지는 분자를 전극으로 사용하는 유기물 이차 전지가 각광받고 있다. 유기 전극 소재는 주로 전형 원소로 구성된 탄소 기반 네트워크로 이루어져 있고, 화학적 개질이 용이하다는 장점을 가지고 있다. 이러한 유기 전극 소재 고유의 장점들은 구조적 다양성과 지속가능성 측면에서 높은 잠재성을 가지도록 한다. 하지만 낮은 전기전도도와 높은 용해도를 가지는 유기물의 고유 물성은 유기 산화/환원 소재의 전기화학 성능을 저해한다. 이러한 문제점을 극복하기 위해 화학적 개질이 용이하다는 특성에서 기인한 다양한 전략들이 제시되어 왔다. 치환기를 도입하거나 고분자화 하는 분자 단위의 개질과 전도성 구조체와 복합 전극을 만드는 전극 단위의 개질이 실행되었으나, 모든 개질은 분자 간의 연결체와

전도성 구조체와 같은 산화/환원 비활성을 띄는 도입부를 추가해야 하기 때문에 무게의 증가에 따른 에너지 밀도의 감소를 유발한다. 따라서, 전기화학 성능의 상충관계를 초래하게 되는 산화/환원 비활성 도입부를 활용하지 않는 새로운 접근법이 필요하다.

이러한 관점에서 고유 물성 향상을 위해 산화/환원 활성을 가지는 분자들의 분자간 상호작용을 이용하는 방식으로 발상을 전환했다. 유기물 전하 이동 착물은 두 가지 이상의 유기 분자들 (전자 공여체와 전자 수용체)의 조합으로 분자 간에 부분 전하가 전이되어 형성된다. 전자 공여체와 전자 수용체 간의 오비탈 혼합은 전하 이동 현상을 야기하고, 이러한 전하 이동 상호작용을 이루기 위해 전자 공여체와 전자 수용체는 강력한 분자간 힘을 통한 층상 구조를 가지고자 분자간 재배열을 이루게 된다. 상호보완적 수소결합과  $\pi$ - $\pi$  적층으로부터 기인한 유기물 전하 이동 착물의 구조적 특성은 구조적 안정성과 전기전도도의 향상을 동시에 이뤄낸다. 유기물 전하 이동 착물을 산화/환원 활성을 가지는 분자들로만 구성한다면 전기화학 성능을 유지하면서 기존의 유기물 고유의 한계점을 극복해낼 수 있다.

본 논문에서는 보고된 산화/환원 활성을 가지는 분자들 (Phenazine (PNZ) 과 7,7,8,8-tetracyanoquinodimethane (TCNQ))을 조합하여 형성한 유기물 전하 이동 착물을 최초로 전극 소재로 도입했다. PNZ-

TCNQ 복합체는 성공적으로 전기전도도의 향상과 용해도의 감소를 보여주며 훌륭한 수준의 배터리 성능을 나타냈다. 그럼에도 불구하고 유기 전극 소재의 상대적으로 낮은 작동 전압과 PNZ 단분자의 산화/환원 비활성은 에너지 밀도를 제한하여 배터리 성능의 향상을 저해한다. 이러한 문제를 해결하기 위해 에너지 밀도 향상을 위한 고전압 유기 전극 소재 개발 및 전자 공여체 분자의 산화/환원 비활성 현상의 기원에 대한 분석을 병렬로 진행한다. 첫째로, 리튬 대비 4.1 V의 고전압을 구현할 수 있는 새로운 전자 공여체 분자 (dibenzo-1,4-dioxin (DD))가 산화/환원 중심원소를 높은 전기음성도의 16 족 원소 (산소)로 치환함으로써 개발되었다. DD와 TCNQ를 조합한 새로운 복합체 전극이 성공적으로 제작되었으며, DD-TCNQ 복합체는 약  $560 \text{ Wh kg}^{-1}$ 의 향상된 에너지밀도와 더불어 높은 배터리 성능을 보여주었다. 둘째로, 전자 공여체 분자의 산화/환원 비활성 현상의 기원을 밝히고 궁극적으로 산화/환원 반응을 완벽히 구현해내기 위해 유기 전극 소재의 산화/환원 반응에 영향을 주는 요인을 분석하는 데에 초점을 맞췄다. 무기 전극 소재와 달리 최근에 이르러 유기 전극 소재는 전해질의 종류, 즉 전자 전달 이온과 용매 중 각각에 따라 전기화학 반응 경로가 달라지는 것이 보고되고 있다. 이러한 보고들을 통해 유기 활물질과 전해질 간의 상호작용에 따라 에너지 저장 메커니즘이 영향을 받는다고 예상할 수

있다. 따라서 유기 전극 소재의 산화/환원 양상을 자세히 분석하기 위해 유기에서 수계에 이르는 다양한 용매종과 1 가에서 2 가 이온에 이르는 다양한 전자 전달 이온종을 활용하여 전기화학 테스트를 진행했다. PNZ-TCNQ 복합체 전극이 용매 종과 전자 전달 이온 중에 따라 다른 산화/환원 반응 경로를 지나는 것을 확인했다. 또한 다른 리튬 기반의 전해질에서는 TCNQ 의 산화/환원 활성만이 가능했는데 아연 수계 전해질에서 PNZ 와 TCNQ 의 산화/환원 활성이 모두 구현되었다. 전해질 종에 따라 상이하게 얻어진 산화/환원 메커니즘들을 분석한 결과, 아연 수계 전해질을 제외한 전해질에서 활물질이 전해질과의 접촉 직후에 즉각적인 상변태가 일어남을 관찰했다. 초기 상변태로부터 미리 형성된 생성물은 TCNQ 분자와 전해질이 부반응을 하여 형성된 부산물임을 확인했고, 이런 전해질의 유기 활물질 구조 내 개입이 구조적 불안정성을 야기해 재료의 붕괴를 일으켰을 것이라는 추측을 가능케 했다. 그래서 화학적 부반응이 일어나지 않아 유기 활물질의 구조적 안정성을 유지할 수 있는 아연 수계 전지에서 PNZ-TCNQ 복합체가 4 전자 반응을 동반한 완벽한 산화/환원 반응 구현에 성공했을 것으로 추측된다. 또한, 아연 수계 전해질에서 전도성이 높은 수계 용매와 구조적 안정성으로부터 얻어지는 시너지 효과를 통해 PNZ-TCNQ 복합체 전극의 추가적으로 향상된 속도 및 수명 특성을 성공적으로



얻어냈다. 첨가제 없이 고유 물성 향상을 이뤄낼 수 있는 새로운 물질군 (유기물 전하 이동 착물)은 미래형 에너지 저장 시스템을 위한 물질 후보군을 확장하는 데에 새로운 지평을 열었다. 산화/환원 활성을 가지는 분자들의 수많은 조합이 가지는 무한한 잠재성과 뛰어난 배터리 성능은 지속가능한 에너지 소재의 상용화에 한 걸음 더 다가가게 할 것이다.

**주요어:** 이차 전지, 유기 산화/환원 활성 분자, 유기물 이차 전지, 전하 이동 착물, 전해질-활물질 상호작용

**학 번:** 2015-20852